Eigenvalue analysis of amorphous solids consisting of frictional grains under athermal quasistatic shear

Daisuke Ishima

January 27, 2023

Contents

Publication list for the requirement of this thesis

1. Daisuke Ishima, Kuniyasu Saitoh, Michio Otsuki, and Hisao Hayakawa, "Theory of rigidity and density of states of two-dimensional amorphous solids of dispersed frictional grains in the linear response regime", Submitted to Phys. Rev. E (Chapter 3), arXiv:2207.06632.

2. Daisuke Ishima, Kuniyasu Saitoh, Michio Otsuki, and Hisao Hayakawa, "Eigenvalue analysis of stress-strain curve of two-dimensional amorphous solids of dispersed frictional grains with finite shear strain", Submitted to Phys. Rev. E (Chapter 4), arXiv:2212.04628.

Reference papers

1. Daisuke Ishima and Hisao Hayakawa, "Scaling laws for frictional granular materials confined by constant pressure under oscillatory shear", Phys. Rev. E **101**, 042902 (2020) [12 pages].

2. Daisuke Ishima and Hisao Hayakawa, "Dilatancy of frictional granular materials under oscillatory shear with constant pressure", EPJ Web of Conf. **249**, 02011 (2021) [4 pages].

Abstract

This study performs eigenvalue analysis of two-dimensional amorphous solids comprising frictional grains under athermal quasistatic shear. First, (Chapters 3 and 4) the eigenvalue analysis of amorphous solids with friction is performed for two cases; (i) the contact force between grains expressed as the Hertzian force under a linear response regime and (ii) the contact force between grains owing to a linear spring, which is equivalent to a harmonic potential under finite shear strain.

In Chapter 1, previous studies on mechanical responses of dispersed amorphous solids under external agitations are reviewed.

In Chapter 2 of this thesis, the models and methods used are explained. In this study, the forces acting between grains are modeled using the discrete element method (DEM), where the grains interact only when in contact. In addition, the repulsive forces acting in the tangential direction at the point of contact of grains are modeled, which is seldom investigated in conventional eigenvalue analysis.

Two separated modes in the density of states for sufficiently small k_T/k_N, which is the ratio of the tangential to normal stiffness, are obtained. Rotational modes are found at low frequencies or small eigenvalues, whereas translational modes are found at high frequencies or large eigenvalues. Further, the location of the rotational band shifts to the high-frequency region with an increase in k_T/k_N and becomes indistinguishable from the translational band for large k_T/k_N. In addition, the rigidity is obtained using the eigenvalue analysis for frictional grains with infinitesimal strain with the aid of the Jacobian matrix. These are brief summaries of obtained results in Chapter 3.

Thereafter, the eigenvalue analysis is extended to the case of finite strain in Chapter 4. After obtaining the configuration of grains, the stress-strain curve based on the eigenvalue analysis is found to have almost perfect agreement with that obtained via the simulation, regardless of stress avalanches causing plastic deformations. Moreover, in contrast to expectations, the eigenvalues in the proposed model do not indicate any precursors to the stress-drop events.

In Chapter 5, we discuss and conclude our results obtained in the thesis.

We present some appendices to explain the details. In appendix A, we summarize the properties of the Jacobian. In appendix B, we present the explicit expressions of the Jacobian with the Hertzian contact force. In appendix C, we derive the rigidity for the linear response regime by eigenvalue analysis. In

Chapter 1

Introduction

1.1 Dispersed amorphous solids

Amorphous materials comprising dispersed grains such as powders, colloids, bubbles, and emulsions are ubiquitous in nature [1–8]. Therefore, understanding the behavior of dispersed amorphous systems is an important issue in the wide field of research such as pharmacology, engineering, agriculture, and physics [2, 6–8]. In particular, the dynamic processes of dispersed amorphous materials can be commonly observed in daily life for drug mixing, debris flow, snow avalanches, etc. Thus, understanding their properties is vital.

Dispersed amorphous materials behave as fragile solids above a critical density, and as liquid or gas below this critical density [9–21]. This non-equilibrium transition between the gas or liquid-like phase and the solid-like phase is referred to as the jamming transition. At the jamming point, the viscosity diverges, and rigidity emerges (see Fig. 1.1) [5]. Even when focusing on a dispersed amorphous solid where the density of grains is higher than the jamming density ϕ_c, the behavior of the solid is different from conventional solids. Additionally, the behavior is strongly dependent on the history of the preparation of the initial state [22–24]. These studies examined the mechanical response of dispersed amorphous solids under step strain. Such collections of dispersed dense grains above the jamming density are referred to as (dispersed) amorphous solids in this study.

Typically, solid-state physics assumes the crystalline structure of materials as reported in the standard texts on condensed matter physics [1, 25]. However, there are numerous studies on amorphous solids wherein the structure of particle arrangement lacks a long-range order [3, 5, 7, 26]. Nevertheless, amorphous solids have been studied within the framework of equilibrium statistical mechanics for disordered systems. When considering a collection of repulsive large grains with disorders such as granular materials, conventional statistical mechanics is no longer applicable, because such a system can be regarded as a system at zero temperature with an infinitely large number of degenerated

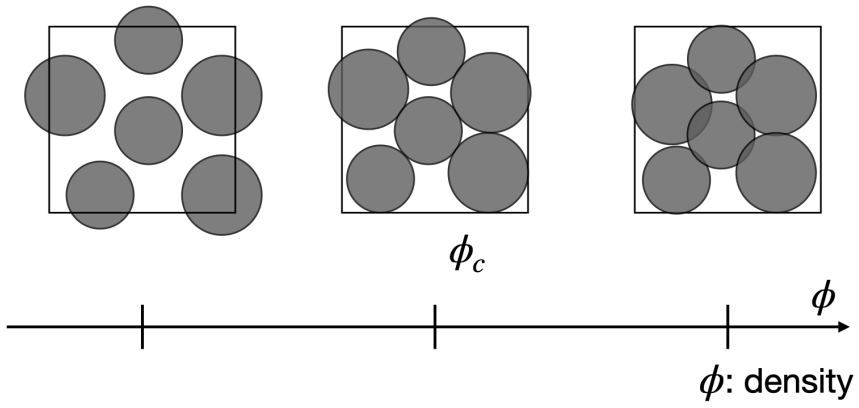

Figure 1.1: Schematic image of collections of grains for the jamming transition.

ground states corresponding to the metastable states in the energy landscape. In the late 1980s, Edwards and his coworkers attempted to formulate the statistical mechanics of granular assemblies [8, 27–29]. Consequently, it became a fashionable field of physics in the early 1990s to study the physics of granular materials such as sand avalanches [30–32]. Since the pioneering work by Liu and Nagel [10], the jamming transition has attracted increased attention as a typical problem of non-equilibrium physics [9–13, 16–19, 33]. The jamming transition of frictionless grains is a mixed transition as a functions of density ϕ where the pressure and shear modulus change continuously, whereas the coordination number and bulk modulus change in a discontinuous manner at the jamming point [12,16,18,19,34]. Researchers have found that the stresses of such systems satisfy scaling laws as a function of $\phi - \phi_c$ near the jamming point [6, 12, 16–19] such as $P \propto (\phi - \phi_c)$ and $G \propto (\phi - \phi_c)^{1/2}$ for linear spring contact model with pressure P and rigidity G.

Dilatancy, which is the volume expansion of a dispersed amorphous material, occurs [2, 35–37], when shear is applied. A more dilatant structure is realized for a high shear rate [38–41]. Previous studies have reported the existence of compaction wherein repeated oscillations to a system have rendered the system denser with more ordered configurations [4, 42–47]. Recently, it was reported that dilatant and compactified behaviors are strongly dependent on the preparation of the initial configuration of the collection of grains [48].

1.2 Effects of mutual friction between grains

Friction between materials is an important element for large grains, which cannot be ignored, although many theoretical studies have ignored its contribution. Here, the friction is essential for daily life because we cannot control moving

objects properly with zero friction, for example. The frictional force between contacted grains can be classified into dynamic and static friction forces [49]. More than 500 years ago, Leonardo suggested that the static friction force is directly proportional to the load on the contact surface:

$$F_{\text{Static}} = \mu_s F_\perp \tag{1.1}$$

where $F_{\text{Static}}, F_\perp$, and μ_s are the static frictional force, force vertical to the surface of the material, and static friction coefficient, respectively. In the 18th century, Amontons and Coulomb presented a more modern interpretation, summarizing the frictional forces as follows: (i) The frictional force does not depend on the apparent contact area, (ii) it is proportional to the vertical force, and (iii) the dynamic frictional coefficient μ is smaller than the static frictional coefficient μ_s and is independent of velocity. These empirical laws for frictional forces are referred to as Amontons-Coulomb's laws [49, 50]; however, the mechanism underlying the empirical laws has not been clarified yet. This is because friction is governed by various factors, such as the shape and surface conditions of contacted materials, as well as the existence or absence of interstitial fluids between them [51]. Moreover, Amontons-Coulomb's law is not a precise empirical law but an approximate one. Indeed, it has been confirmed theoretically and experimentally that dynamic frictional force is dependent on relative velocity [52–54], whereas the static friction is dependent on the duration time of contacted materials [54, 55]. Though the microscopic mechanism of friction remains unclear, inter-grain dynamical friction is modeled using Amontons-Coulomb's law when considering the dynamics of a collection of grains.

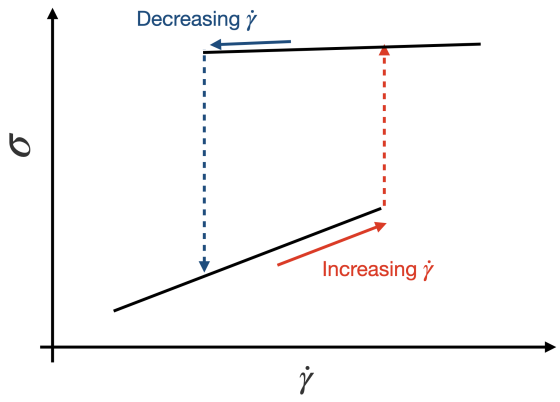

Figure 1.2: Plot of the shear stress σ against the shear rate $\dot{\gamma}$ observed in amorphous solids consisting of frictional grains under steady shear. This figure is modified by hand from the original one in Ref. [21].

In the case of dense granular and suspension systems, the inter-grain friction dramatically alters the rheological properties, such as discontinuous shear

thickening (DST) [21,56–61] and shear jamming [60–66]. DST is a phenomenon wherein the shear stress changes in a discontinuous manner with an increase or decrease in the shear rate. It has attracted the attention of physicists because the shear stress exhibits a hysteresis with an increase or decrease in the shear rate (see Fig. 1.2) [21, 56–61]. Recently, it has been confirmed that the shear jamming occurs owing to the memory effects of training a grain configuration, such as shaking the system [60, 61]. In addition, it has been reported that the DST occurs in the fragile region on the boundary between shear jamming and non-jamming regions [60, 61]. In granular materials comprising frictionless grains under oscillatory shear, two types of transitions have been reported; yielding transition, wherein the grains lose their recurrence, and softening transition, wherein the rigidity begins to decrease significantly [67–70]. Further, Ishima and Hayakawa found that yielding and softening transitions were indistinguishable in systems with mutual friction between grains [71]. This finding is consistent with the observation of a frictionless system in Ref. [60]. Furthermore, a study revealed that the scaling law between rigidity and strain scaled by pressure holds for frictional grains in oscillatory sheared granular materials (see Fig. 1.3 (a)), whereas it does not hold for frictionless grains (see Fig. 1.3 (b)) [21, 71, 72]. Here, rigidity G is introduced for oscillatory sheared materials [73–76]:

$$G := \frac{\sigma}{\gamma_0} \tag{1.2}$$

where σ and γ_0 are the shear stress and shear strain amplitude, respectively, for oscillatory sheared systems.

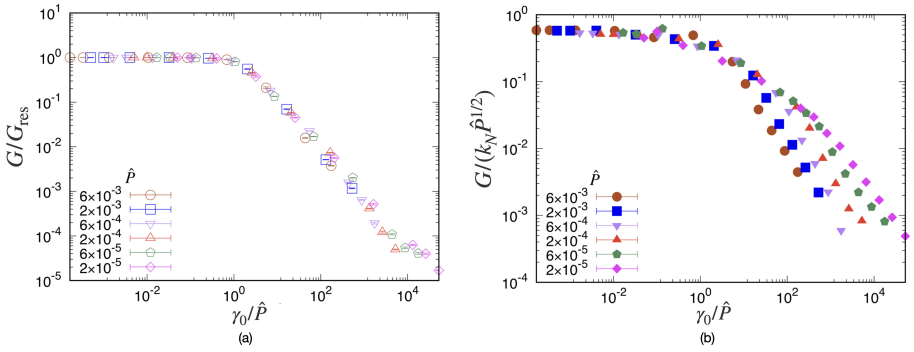

Figure 1.3: Plots of the scaled rigidity against scaled strain for (a) frictional grains with $\mu = 1.0$ and (b) frictionless grains with $\mu = 0$, where $\gamma_0, \hat{P}$, and μ are the shear strain amplitude, normalized pressure, and friction coefficient. Here, we have introduced $G_{\rm res} := \lim_{\gamma_0 \to 0} G$. These figures are modified from the original figures in Reference paper 1, corresponding to Ref. [71], where we have deleted the slopes of the line.

Amorphous systems comprising repulsive grains with mutual friction contain large constituent grains whose diameters satisfy $d \geq 0.01$mm. The characteristic

feature of a granular system is that the grains repel each other only when they are in contact [2]. In the case of granular materials, owing to the grain size being sufficiently large, the thermal fluctuations are negligible. However, if the grains are wet, the adsorption force is mediated by water, which varies depending on the amount of water [77]. Furthermore, if grains are mono-dispersed, the systems exhibit melting and crystallization similar to a conventional liquid-solid phase transition [78]. Thus, many previous studies on amorphous solids adopted two dispersed dry grains for simplicity (see, e.g., [12,18,33]). Note that the results obtained by bi-dispersed systems are not always universal ones. A power law size distribution of the grain is generated after the impact fracture of grains and other materials [79, 80]. The jamming point becomes denser in systems with a power law distribution than that of bi-disperse systems [81]. In this study, a granular system, wherein only simple repulsive interactions acted between contacted grains with mutual friction, is considered.

1.3 Eigenvalue analysis of dynamical matrix for amorphous solids

For amorphous solids comprising frictionless grains, an analysis of the dynamical matrix or the Hessian matrix is useful. The Hessian matrix is defined as the second derivative of the potential of a collection of grains concerning the displacements from their stable configuration [5, 8, 17, 82–88]:

$$\mathcal{H}_{ij}^{\kappa\zeta} := \frac{\partial^2 U}{\partial r_i^\kappa \partial r_j^\zeta}, \tag{1.3}$$

where i and j denote the particle indices, and κ and ζ represent the position component. The density of states (DOS) is the distribution function of the eigenfrequency of Hessian matrix [5, 8, 17, 82, 84, 85, 87–89]. Debye's theory, $D(\omega) \sim \omega^{d_s-1}$, with the DOS $D(\omega)$, spatial dimension d_s, and mode frequency ω, is valid for low-frequency regions [12,85,90,91]. Recently, $D(\omega) \sim \omega^4$ is valid, where this power-law behavior of frequencies is independent of dimension [84,92]. In particular, $D(\omega) \sim \omega^4$ is observed in the extremely low-frequency region for the small system sizes, which is lower than the frequency of the Debye region [84].

From the analysis of the DOS for systems composed of anisotropic grains, such as ellipses, dimers, deformable grains, and grains with rough surfaces with the aid of the Hessian matrix [93–103], researchers found that a rotational band in the DOS can be distinguished from the translational band [94, 96, 97, 100, 102, 103]. Additionally, the low-frequency mode called quartic mode has been observed in ellipsoidal grains for hypostatic configurations [95,97]. Although for systems of spherical grains with inter-grain friction, similar results are expected owing to grain rotations, studies reporting the existence of rotational bands in the DOS are rare. Because the frictional force between the grains is dependent on the contact history, it cannot be a conservative force. Therefore, stability analysis for frictional grains based on the Hessian cannot be used. Nevertheless,

the Hessian analysis using an effective potential for frictional grains has been performed [104,105], where the effective potential between contacting i and j-th grains is introduced as

$$\delta e_{ij} := \frac{1}{2}\left[k_N(\delta \boldsymbol{r}_{ij}\cdot \boldsymbol{n}_{ij}) - \frac{f_{N,ij}}{r_{ij}} + k_T \delta t_{ij}^2\right], \tag{1.4}$$

where k_N is the normal spring constant, k_T is the tangential spring constant, $\delta \boldsymbol{r}_{ij}$ is the virtual displacement for the translational directions from the force balance state of grains, δt_{ij} is the virtual displacement for the rotational directions, $\boldsymbol{n}_{ij}$ is the normal unit vector, and $f_{N,ij}$ is the normal force between the i and j-th grains at stable configuration. They reported that the mutual friction between grains causes a continuous change in the functional form of the DOS from that of frictionless systems [104, 105]. Recently, Liu et al. performed an eigenvalue analysis of an amorphous solid comprising frictional grains considering slip processes of grains, both experimentally and numerically [106]. Consequently, the grain configuration is successfully partitioned into clusters that contribute to the rigidity. However, studies on amorphous solids comprising frictional grains are scarce.

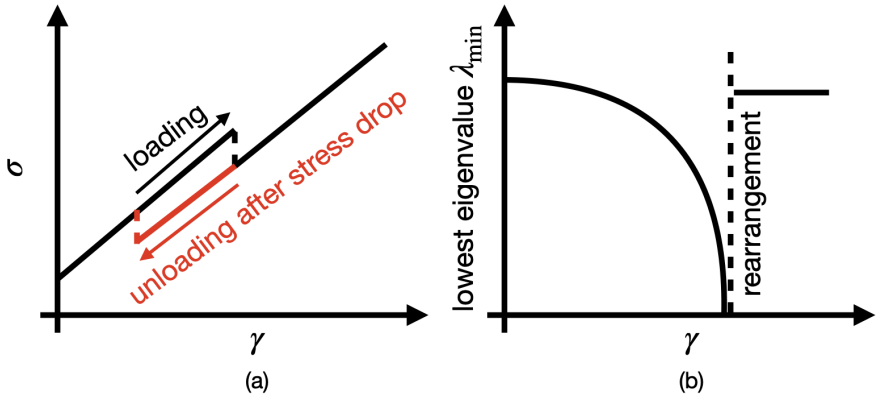

Figure 1.4: Schematic plots of (a) the shear stress σ, and (b) the lowest eigenvalue $\lambda_{\min}$ near stress drop event against shear strain γ under quasistatic shear. These figures are modified from the original one in Ref. [113].

It is generally known that plastic deformation for sheared amorphous solids is caused by the rearrangements of grains. The eigenvalue of the Hessian matrix approaches zero if the curvature of the potential landscape approaches zero nearby a critical strain γ_c [107–113]. Thus, it has been suggested that the decrement of the nonzero smallest eigenvalue of the Hessian matrix with the strain is a precursor of an avalanche or stress drop near γ_c [107, 108, 110–113] (see Fig. 1.4). Previous studies have indicated that instability appears owing

to a saddle-node bifurcation at which the curvature of the potential landscape becomes zero in one direction at the yielding point [107, 108, 114] (see Fig. 1.5). To determine the rigidity, eigenvalue analysis of the Hessian matrix [83, 86, 90, 107–109], is commonly used, although the quantitative accuracy of the theoretical rigidity has not been verified to the best of our knowledge. The analysis based on the saddle-node bifurcation predicts the behavior near γ_c [107, 108, 110, 114]:

$$G - G_{\rm reg} \propto -\frac{1}{\sqrt{\gamma_c - \gamma}}, \tag{1.5}$$

where $G_{\rm reg}$ is the regular part of rigidity G.

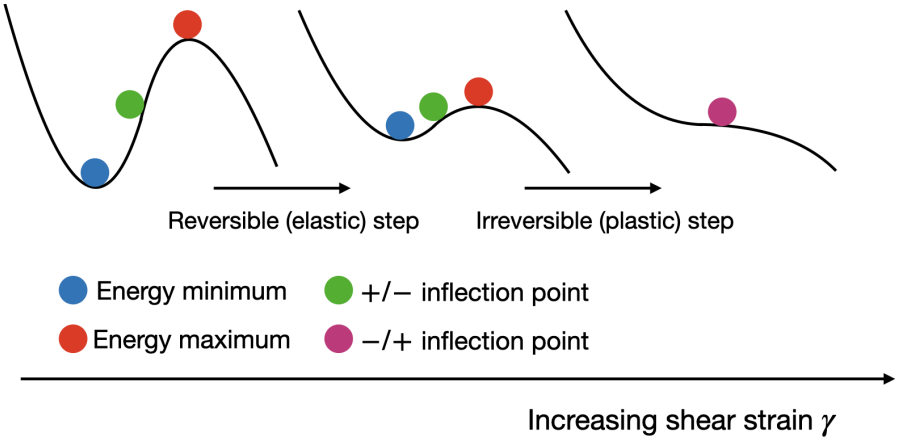

Figure 1.5: Schematics of the change in the potential energy with increase in the strain γ. This figure is modified from the original one in Ref. [108].

Clarifying the role of frictional force between grains is vital because the frictional force cannot be ignored in physical situations. Owing to the inapplicability of the Hessian analysis for such systems, Chattoraj et al. adopted the Jacobian matrix to analyze the stability of the configuration of frictional grains under finite strain [115]. The Jacobian matrix is an asymmetric matrix because it is defined as the derivative of the non-conservative forces originating from inter-grain friction at a certain strain. Therefore, its eigenvalues are generally complex numbers, and the imaginary part of the eigenvalues results in oscillatory instability [115–117]. Till date, no theoretical studies have determined the rigidity of the frictional grains.

1.4 The aim of this thesis

This study presents the results of eigenvalue analysis for dispersed amorphous solids comprising repulsive grains with inter-grain friction. (i) The DOS and

rigidity for Hertzian systems, which have history-dependent terms in contact forces under linear response regime, were determined. (ii) The rigidity is determined, and subsequently, the absence of precursors of the smallest eigenvalue for linear spring (or harmonic) systems for frictional grains under finite strain with stress drop was demonstrated.

1.5 Organization of this thesis

This thesis is organized as follows: Chapter 2 summarizes the models and methods used in this study. First, the discrete element method (DEM), widely used in numerical simulation for granular materials, is discussed. Next, the preparation method of the initial configuration using the fast inertial relaxation engine (FIRE) is explained [118]. Finally, the numerical integration method, referred to as the velocity Verlet method, is described in detail, including its accuracy. Chapter 3 presents the results of the DOS and theoretical prediction of rigidity in the linear response regime. The remainder of this chapter is organized as follows. The first section is the introduction of this chapter. The subsequent section introduces the numerical method. Section 3.3 introduces the Jacobian matrix. Section 3.4 comprises Sec. 3.4.1, which presents the DOS, and Sec. 3.4.2, which describes the theoretical prediction of rigidity in the linear response regime. The final section of this chapter summarizes the results of this study and presents a discussion on future work. Chapter 4 presents the results of the stress-strain relation obtained using the theory formulated in Sec. 4.3. Further, the theoretical and simulation results are compared to demonstrate the relevancy of the proposed theoretical analysis. The remainder of this chapter is organized as follows. The first section is the introduction of this chapter. Section 4.2 introduces the model to be analyzed in this study. Then, Section 4.3 summarizes the theoretical framework for determining the rigidity of an amorphous solid comprising frictional grains without considering the dynamical slip process. Section 4.4 presents the results of the stress-strain relation obtained using the theory formulated in Sec. 4.3. In addition, the theoretical and simulation results are compared to demonstrate the relevancy of the proposed theoretical analysis. Thereafter, Section 4.5 summarizes the obtained results and addresses future tasks to be solved. Finally, Chapter 5 summarizes all the results and conclusions. In Appendix A, we summarize the properties of the Jacobian, which is necessary for history-dependent frictional contact. In Appendix B, we present the explicit expressions of the Jacobian for Hertzian contact. In Appendix C, we derive the theoretical expression of G for linear response. In Appendix D, we investigate the effects of rattlers. In Appendix E, we introduce the DOS with the aid of the effective Hessian as in Refs. [104–106]. In Appendix F, we investigate the history-dependence of tangential displacement. In Appendix G, we investigate the behavior of the smallest eigenvalue in the vicinity of the stress-drop points. In Appendix H, we briefly summarize the properties of the Hessian matrix of the harmonic contact model. In Appendix I, we briefly summarize the properties of the Jacobian matrix for the harmonic contact model as

in Refs. [115–117, 119]. In Appendix J, we derive the theoretical expression of G with the eigenvalue analysis for finite strain.

Chapter 2

Models and methods used in this thesis

In this chapter, we describe models and methods used in this thesis, such as the discrete element method (DEM) method and the fast inertial relaxation engine (FIRE). In Sec. 2.1, we introduce the equations of motion describing the translational and rotational motions of grains. In Sec. 2.2, we describe the modeling of inter-grain forces. In Sec. 2.3, we introduce a method for preparing initial configurations using the FIRE. In particular, we describe the details of FIRE and its application to our system. In Sec. 2.4, we explain the velocity Verlet method, which is a numerical integration method for the MD, taking into account its accuracy for the velocity-dependent system.

2.1 Equations of motion

We model the dynamics of granular material as a collection of grains which are each specified by their position, momentum, and angular momentum. The equation of motion of the i-th grain with the position $\boldsymbol{r}_i$ is given by,

$$m_i \frac{d^2 \boldsymbol{r}_i}{dt^2} = \sum_{j \neq i} \boldsymbol{f}_{ij} + \boldsymbol{F}_i^{(\mathrm{drag})}, \tag{2.1}$$

where m_i, $\boldsymbol{f}_{ij}$, and $\boldsymbol{F}_i^{(\mathrm{drag})}$ are the mass of the i-th grain, the repulsive force acting on the i-th grain from j-th grain, and dissipative force of i-th grain, respectively. Here, we introduce non-zero drag force $\boldsymbol{F}_i^{(\mathrm{drag})} := -m_i \eta_D \boldsymbol{v}_i$, as a simplified description of friction between the moving grain and background fluid [106, 120–122] only in Chapter 4, where η_D and $\boldsymbol{v}_i := d\boldsymbol{r}_i/dt$ are the damping coefficient and the velocity of i-th grain, respectively. In other words, we use the model with $\boldsymbol{F}_i^{(\mathrm{drag})} = 0$ in Chapter 3. To conduct numerical simulation, we have to model the repulsive force $\boldsymbol{f}_{ij}$ according to the properties of the grains.

The equation of motion for the rotation of i-th grain in a two-dimensional system is given by

$$I_i \frac{d\omega_i}{dt} = \sum_{j \neq i} T_{ij} + T_i^{(\mathrm{drag})}, \tag{2.2}$$

where I_i, ω_i, T_{ij}, and $T_i^{(\mathrm{drag})}$ are the moment of i-th grain, the angular velocity of the i-th grain, the torque from the j-th grain acting on the i-th grain, and the dissipative torque of i-th grain, respectively. Note that the torque-balance equation is one for z-component in a 2D system. Since the force $\boldsymbol{f}_{ij}$ always acts on the surface of i-th grain, the torque T_{ij} is given by

$$T_{ij} = -\frac{d_i}{2} \boldsymbol{f}_{ij} \cdot \boldsymbol{t}_{ij}, \tag{2.3}$$

with diameter d_i of i-th grain and the unit vector $\boldsymbol{t}_{ij}$ in the tangential direction at the contact point. We adopt that $T_i^{(\mathrm{drag})} := -I_i \eta_D \omega_i$, as a simplified description of friction between the moving grain and background only in Chapter 4, but $T_i^{(\mathrm{drag})} = 0$ in Sec. 3.

2.2 Modeling of inter-grain force

For macroscopic grains such as granular particles, the force acting on each grain is repulsive and dissipative [123–125]. In this thesis, we adopt the DEM proposed by Cundall and Strack [123], which is a standard simulator of grain dynamics. We assume that the repulsive force between contacting grains is elastic, which can be expressed as a spring and dashpot, respectively (see Fig. 2.1), where we use the divider (a pair of parallel bars vertical to the compression direction) to express that the repulsive force only appears when the grains are contacted. The force $\boldsymbol{f}_{ij}$ exerted by the j-th grain on the i-th grain is expressed as

$$\boldsymbol{f}_{ij} = (\boldsymbol{f}_{N,ij} + \boldsymbol{f}_{T,ij})\, H\left(\frac{d_{ij}}{2} - r_{ij}\right), \tag{2.4}$$

where $\boldsymbol{f}_{N,ij}$ and $\boldsymbol{f}_{T,ij}$ are the contact force in the normal and tangential directions, respectively, with $d_{ij} = (d_i + d_j), r_{ij} = |\boldsymbol{r_{ij}}|$, and $\boldsymbol{r}_{ij} = \boldsymbol{r}_i - \boldsymbol{r}_j$. Here, $H(x)$ is Heviside's staircase function as

$$H(x) = \begin{cases} 1 & (x > 0) \\ 0 & (x \leq 0) \end{cases} . \tag{2.5}$$

2.2.1 Elastic repulsive and dissipative forces

We have adopted the Hertzian normal force as the static repulsive force in the normal direction in Chapter 3 and Hookean force in the normal repulsive force

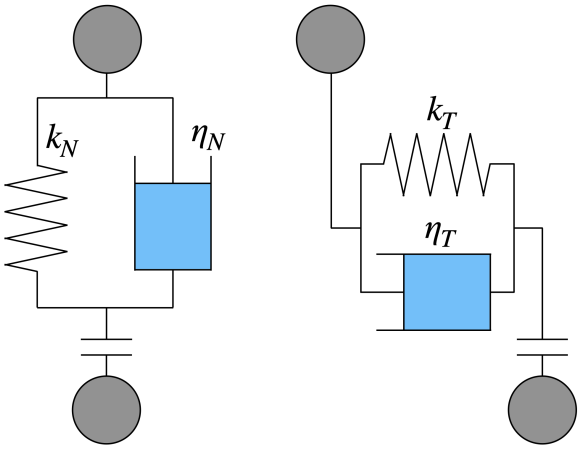

Figure 2.1: Schematics of the repulsive force in the DEM, where the divider and spring express the condition of contact and elastic repulsive force, respectively. Left and right figures express the contacting force in normal and tangential directions acting on contacting grains, respectively. Here dashpots (with η_N and η_T) express dissipative force proportional to relative speed of contacting grains.

in Chapter 4. Here, the compression in the normal direction between i and j-th grains $\xi_{N,ij}$ is defined as

$$\xi_{N,ij} = \frac{d_{ij}}{2} - |\boldsymbol{r}_{ij}|. \tag{2.6}$$

On the other hand, tangential compression $\xi_{T,ij}$ is defined as

$$\xi_{T,ij} := |\boldsymbol{\xi}_{T,ij}| \tag{2.7}$$

with the tangential compression vector

$$\boldsymbol{\xi}_{T,ij}(t) := \int_{C_{ij}(t')} dt' \boldsymbol{v}_{T,ij}(t') - \left[\left(\int_{C_{ij}(t')} dt' \boldsymbol{v}_{T,ij}(t') \right) \cdot \boldsymbol{n}_{ij}(t) \right] \boldsymbol{n}_{ij}(t), \tag{2.8}$$

where $\boldsymbol{n}_{ij} := (n_{ij}^x, n_{ij}^y)^{\mathrm{T}} := \boldsymbol{r}_{ij}/r_{ij}$, $\boldsymbol{v}_{T,ij} := \boldsymbol{v}_{ij} - \boldsymbol{v}_{N,ij} + \boldsymbol{u}_{ij}(d_i\omega_i + d_j\omega_j)/2$, and $\int_{C_{ij}(t')} dt'$ is the integration over the duration time of contact between i and j-th grains. Here, we have introduced $\boldsymbol{u}_{ij} := (n_{ij}^y, -n_{ij}^x)^{\mathrm{T}}$, $\boldsymbol{v}_{ij} := d\boldsymbol{r}_{ij}/dt$, and $\boldsymbol{v}_{N,ij} := (\boldsymbol{v}_{ij} \cdot \boldsymbol{n}_{ij})\boldsymbol{n}_{ij}$.

Hertzian case

The repulsive force of 3-dimensional spheres for normal direction is expressed as Hertzian contact force [126–128], where the repulsive force is proportional to

the $\xi_{N,ij}^{3/2}$ with normal stiffness constant k_N [126–128]:

$$\boldsymbol{f}_{N,ij} = k_N \xi_{N,ij}^{3/2} \boldsymbol{n}_{ij} - \eta_N \boldsymbol{v}_{N,ij}, \tag{2.9}$$

where $\boldsymbol{n}_{ij} := \boldsymbol{r}_{ij}/|\boldsymbol{r}_{ij}|$ and the normal damping coefficient η_N. The tangential contact force $\boldsymbol{f}_{T,ij}$ is expressed as

$$\boldsymbol{f}_{T,ij} = k_T \xi_{N,ij}^{1/2} \xi_{T,ij} \boldsymbol{t}_{ij} - \eta_T \boldsymbol{v}_{T,ij}, \tag{2.10}$$

where we have introduced $\boldsymbol{t}_{ij} := -\boldsymbol{\xi}_{T,ij}/|\boldsymbol{\xi}_{T,ij}|$, tangential stiffness constant k_T, and tangential damping coefficient η_T. Although, strictly speaking, η_N is proportional to $\xi_{N,ij}^{1/2}$ [129–131], we adopt simplified dissipative forces where η_N and η_T are constants as in Eq. (2.9) in the analysis in Chapter 3 because we are not interested in the relaxation dynamics.

Hookean case

The repulsive force of contacting cylinders or circular disks in the normal direction is expressed as a product of a linear function of $\xi_{N,ij}$ and its logarithmic function [128]. When we ignore the logarithmic contribution, the normal contacting force is reduced to

$$\boldsymbol{f}_{N,ij} = k_N \xi_{N,ij} \boldsymbol{n}_{ij} - \eta_N \boldsymbol{v}_{N,ij}. \tag{2.11}$$

Similarly, the tangential repulsive force is introduced as

$$\boldsymbol{f}_{T,ij} = k_T \xi_{T,ij} \boldsymbol{t}_{ij} - \eta_T \boldsymbol{v}_{T,ij}. \tag{2.12}$$

Here, we may use the Hookean model to describe the approximate motion of circular disks or cylinders. Although there are viscous or dissipative contact force terms $-\eta_N \boldsymbol{v}_{N,ij}$ and $-\eta_T \boldsymbol{v}_{T,ij}$ proportional to inter-grain speed in realistic situations, we ignore such effects in the analysis of Chapter 4 because we are interested in quasi-static situations. In this case, fluid drag terms in Eqs. (2.1) and (2.2) play important roles.

Sliding friction

The empirical frictional force switches from static to dynamic friction when the tangential force exceeds the threshold of tangential force. To include this switch mechanism between static and dynamic friction, we express $\boldsymbol{f}_{T,ij}$ as [124]:

$$\boldsymbol{f}_{T,ij} = \begin{cases} \boldsymbol{f}_{T,ij}^{(\mathrm{static})} & (|\boldsymbol{f}_{T,ij}^{(\mathrm{static})}| < \mu |\boldsymbol{f}_{N,ij}|) \\ \mu |\boldsymbol{f}_{N,ij}| \boldsymbol{t}_{ij} & (\text{otherwise}) \end{cases}, \tag{2.13}$$

where μ, and $\boldsymbol{f}_{T,ij}^{(\mathrm{static})}$ are the friction coefficient, and static tangential force in Eq. (2.10) or Eq. (2.12), respectively. Although the slip process is important in physical situations, we focus only on non-slip grains in Chapters 3 and 4 from the limitation of the applicability of our eigenvalue analysis.

2.3 Method of preparing configuration before applying the shear

In this section, we summarize the method of preparing a stable configuration of grains before applying the shear. For this purpose, as a first step, we perform the relaxation for frictionless grains with the FIRE. In the second step, the system is relaxed, taking into account the static friction between grains. In the first subsection, we summarize how to prepare the configurations of frictionless grains by the FIRE [118]. In the second subsection, we describe the details of the numerical method, including the force with static friction.

2.3.1 Method of preparing configuration before applying shear by FIRE

At first, we place grains at random without any overlaps of grains with the initial fraction $\phi_{\rm ini} = 0.6$. We increase the projected area fraction of the system by the increment of the fraction $\Phi := \phi^{\rm New} - \phi^{\rm Old}$ up to the target fraction ϕ, where $\phi^{\rm Old}$ and $\phi^{\rm New}$ are the projected area fraction of the system before and after each step of the increment, respectively. After each step of the increment, the system is relaxed by the FIRE [118].

To implement the process of increasing the area fraction, we scale the system as

$$L^{\rm New} = L^{\rm Old}\sqrt{\frac{\phi^{\rm Old}}{\phi^{\rm New}}}, \tag{2.14}$$

$$\boldsymbol{r}_i^{\rm New} = \boldsymbol{r}_i^{\rm Old}\sqrt{\frac{\phi^{\rm Old}}{\phi^{\rm New}}}, \tag{2.15}$$

where $L^{\rm Old}/L^{\rm New}$ and $\boldsymbol{r}_i^{\rm Old}/\boldsymbol{r}_i^{\rm New}$are the linear system size and the position of the i-th grain before/after rescaling, respectively. We adopt $\Phi = 10^{-4}$ throughout this thesis. When there are overlaps between grains at $\phi^{\rm New}$, the system relaxes to a stable configuration with the aid of the FIRE.

The FIRE is a fast relaxation method of minimizing potentials $U(\boldsymbol{r})$ depending on the configuration of the grains $\boldsymbol{r} := (\boldsymbol{r}_1^{\rm T}, \boldsymbol{r}_2^{\rm T}, \cdots, \boldsymbol{r}_N^{\rm T})^{\rm T}$ with $\boldsymbol{r}_i := (r_i^x, r_i^y)^{\rm T} := (x_i, y_i)^{\rm T}$ [118], where the superscript T expresses the transpose. Here, we use the Hertzian potential for $U(\boldsymbol{r})$ in Chapter 3 which is defined as

$$U(\boldsymbol{r}) := \frac{2}{5}k_N \sum_{j\neq i} \xi_{N,ij}^{5/2} H(d_{ij}/2 - |\boldsymbol{r}_{ij}|). \tag{2.16}$$

Let us introduce ζ-component of the force $F_{F,i}^{\zeta}$ acting on the i-th grain as

$$F_{F,i}^{\zeta} := -\frac{\partial U}{\partial r_i^{\zeta}} = \sum_{j\neq i} k_N \xi_{N,ij}^{3/2} n_{ij}^{\zeta} H(d_{ij}/2 - |\boldsymbol{r}_{ij}|), \tag{2.17}$$

where $\zeta = x$ or y. Note that $F^{\zeta}_{F,i}$ only consists of the normal repulsive force. In the FIRE, the position $\boldsymbol{r}$ and velocity $\boldsymbol{v}_F := (\boldsymbol{v}_{F,1}, \boldsymbol{v}_{F,2}, \cdots, \boldsymbol{v}_{F,N})^{\mathrm{T}}$ with $\boldsymbol{v}_{F,i} := (v^x_{F,i}, v^y_{F,i})^{\mathrm{T}}$ are updated by the following rules from (i) to (iv) with the variable time increment Δt_F. (i) The numerical integration via the velocity Verlet method is performed on $\boldsymbol{r}$ and $\boldsymbol{v}_F$:

$$r^{\zeta}_i \to r^{\zeta}_i + \Delta t_F v^{\zeta}_i + \Delta t_F^2 \frac{F^{\zeta}_{F,i}(\boldsymbol{r})}{2m_i}, \tag{2.18}$$

$$v^{\zeta}_{F,i} \to v^{\zeta}_{F,i} + \Delta t_F \frac{F^{\zeta}_{F,i}(\tilde{\boldsymbol{r}}) + F^{\zeta}_{F,i}(\boldsymbol{r})}{2m_i}, \tag{2.19}$$

where $\tilde{\boldsymbol{r}}$ is the updated configuration in Eq. (2.18). (ii) We calculate $P := \boldsymbol{F}_F \cdot \boldsymbol{v}_F$, where $\boldsymbol{F}_F := (\boldsymbol{F}^{\mathrm{T}}_{F,1}, \boldsymbol{F}^{\mathrm{T}}_{F,2}, \cdots, \boldsymbol{F}^{\mathrm{T}}_{F,N})^{\mathrm{T}}$ with $\boldsymbol{F}_{F,i} := (F^x_{F,i}, F^y_{F,i})^{\mathrm{T}}$. (iii) The velocity $\boldsymbol{v}_F$ is updated as

$$\boldsymbol{v}_{F,i} \to \boldsymbol{v}_{F,i} + \chi(\hat{\boldsymbol{v}}_{F,i} - \hat{\boldsymbol{F}}_{F,i})|\boldsymbol{v}_{F,i}|, \tag{2.20}$$

where χ is the relaxation parameter and $\hat{\boldsymbol{a}} := \boldsymbol{a}/|\boldsymbol{a}|$ for an arbitrary vector $\boldsymbol{a}$. (iv) We update χ and Δt_F in the FIRE according to the positive or negative value of P. To speed up the relaxation when the motion is along a potential gradient, we increase Δt_F. Note that this process is performed only when the number of numerical integrations along the potential gradient is larger than a certain number of times $N_{\min}$ to stabilize the numerical calculation. To implement this update rule, if $P > 0$ and the number of numerical integrations of $P > 0$ is larger than $N_{\min}$, Δt_F and χ are updated as

$$\Delta t_F \to \min(\Delta t_F f_{\mathrm{inc}}, \Delta t_{F,\max}), \tag{2.21}$$

$$\chi \to \chi f_{\chi}, \tag{2.22}$$

where $\min(a, b)$ is a selecting function of smaller one from a and b, the parameter f_{inc} is introduced to speed up the relaxation, and f_{χ}, and $\Delta t_{F,\max}$ are parameters to stabilize numerical calculations. Here, we adopt $f_{\mathrm{inc}} = 1.1, f_{\chi} = 0.99, N_{\min} = 5, \Delta t_{F,\max} = 10\Delta t_{F,\mathrm{ini}}$, and $\Delta t_{F,\mathrm{ini}} = 1.0 \times 10^{-2} t_0$ [118,132]. Note that $N_{\min}$ is necessary for the stability of the algorithm. In the case of $P \leq 0$, we set

$$\boldsymbol{v}_F \to \boldsymbol{0}, \tag{2.23}$$

$$\chi \to \chi_{\mathrm{start}}, \tag{2.24}$$

$$\Delta t_F \to \Delta t_F f_{\mathrm{dec}}, \tag{2.25}$$

where we adopt $f_{\mathrm{dec}} = 0.5$ and $\chi_{\mathrm{start}} = 0.1$ [118,132].

We repeat the operations (i) through (iv) until $|F^{\zeta}_{F,i}| < F_{\mathrm{Th}}$ for arbitrary i and ζ. Note that we have used the initial values for $\Delta t_F = \Delta t_{F,\mathrm{ini}}$ and $\chi = \chi_{\mathrm{start}}$ at the starting point of the FIRE. Here, $\boldsymbol{r}$ is given and we set $\boldsymbol{v}_F = \boldsymbol{0}$ at the starting point of the FIRE.

2.3.2 Numerical method for relaxation of the configuration of frictional grains

After we obtain a stable configuration of frictionless grains at a target fraction in terms of the FIRE, we consider the effect of static friction in the relaxation process of frictional grains. The time evolution of the system is given by Eqs. (2.1)–(2.4) until $\tilde{F}^{\alpha}_{F,i} < F_{\rm Th}$ for arbitrary i and α. For the time integration, we adopt the velocity Verlet method with the time increment $\Delta t = 1.0 \times 10^{-2} t_0$.

2.4 Velocity Verlet method in our system

In this section, we first verify the accuracy of the velocity Verlet method. Next, we summarize the implementation of the velocity Verlet method. To simplify the notation, we introduce the generalized force $\tilde{\boldsymbol{f}} := (\tilde{\boldsymbol{f}}_1^{\rm T}, \tilde{\boldsymbol{f}}_2^{\rm T}, \cdots, \tilde{\boldsymbol{f}}_N^{\rm T})^{\rm T}$ with $\tilde{\boldsymbol{f}}_i := (\tilde{f}_i^x, \tilde{f}_i^y, \tilde{f}_i^\ell)^T := (F_i^x/m_i, F_i^y/m_i, 2T_i/(d_i I_i))^{\rm T}$ in this section, where $F_i^\zeta := \sum_{j\neq i} f_{ij}^\zeta - F_i^{({\rm drag}),\zeta}$ for $\zeta = x$ and y, and $T_i := \sum_{j\neq i} T_{ij} - T^{({\rm drag})}$. Here, f_{ij}^ζ and $F_i^{({\rm drag}),\zeta}$ are ζ-component of $\boldsymbol{f}_{ij}$ and $\boldsymbol{F}_i^{({\rm drag})}$, respectively. Note that $\tilde{f}_i^\alpha$ is the generalized force which depends on the generalized position vector $\boldsymbol{q}$ and the generalized velocity $\dot{\boldsymbol{q}}$ as in Eqs. (2.9)–(2.12), where $\boldsymbol{q} := (\boldsymbol{q}_1^{\rm T}, \boldsymbol{q}_2^{\rm T}, \cdot, \boldsymbol{q}_N^{\rm T})^{\rm T}$ with $\boldsymbol{q}_i := (r_i^x, r_i^y, d_i\theta_i/2)^{\rm T}$ and $\dot{\boldsymbol{a}} := d\boldsymbol{a}/dt$ for an arbitrary vector $\boldsymbol{a}$.

2.4.1 Accuracy of the velocity Verlet method for the force depending on the velocity

In this subsection, we check the accuracy of the velocity Verlet method for the force depending on the velocity with the aid of discretization based on the Taylor expansion. The velocity Verlet method is given by a set of equations

$$q_i^\alpha(t+\Delta t) = q_i^\alpha(t) + \Delta t \dot{q}_i^\alpha(t) + \frac{1}{2}\Delta t^2 \tilde{f}_i^\alpha(t), \tag{2.26}$$

$$\dot{q}_i^\alpha(t+\Delta t) = \dot{q}_i^\alpha(t) + \Delta t \frac{\tilde{f}_i^\alpha(t) + \tilde{f}_i^\alpha(t+\Delta t)}{2}. \tag{2.27}$$

The first equation is called the velocity Velret equation for $q_i^\alpha(t)$ and the second one is the equation for $\dot{q}_i^\alpha(t)$. It is known that the velocity Verlet algorithm has the accuracy of $O(\Delta t^2)$ in Hamiltonian systems [133], but little is known about its accuracy for dissipative dynamics. In this subsection, we clarify the accuracy of this method.

Here, we show from the Taylor expansion that the velocity Verlet method has second-order and first-order accuracies of Δt for $\boldsymbol{q}$ and $\dot{\boldsymbol{q}}$, respectively. Based on the Taylor expansion of $q_i^\alpha(t+\Delta t)$, we obtain

$$\begin{aligned} q_i^\alpha(t+\Delta t) &= q_i^\alpha(t) + \Delta t \dot{q}_i^\alpha(t) + \frac{1}{2}\Delta t^2 \ddot{q}_i^\alpha(t) + O(\Delta t^3) \\ &= q_i^\alpha(t) + \Delta t \dot{q}_i^\alpha(t) + \frac{1}{2}\Delta t^2 \tilde{f}_i^\alpha(t) + O(\Delta t^3), \end{aligned} \tag{2.28}$$

where $\dot{A} := dA/dt$ for an arbitrary function A. We can obtain the quadratic precision of Δt for $q_i^\alpha(t+\Delta t)$, because the RHS of Eq. (2.28) is a function of current time t.

On the other hand, based on the Taylor expansion of $\dot{q}_i^\alpha(t+\Delta t)$, we obtain

$$\begin{aligned}\dot{q}_i^\alpha(t+\Delta t) &= \dot{q}_i^\alpha(t) + \Delta t \ddot{q}_i^\alpha(t) + \frac{1}{2}\Delta t^2 \dddot{q}_i^\alpha(t) + O(\Delta t^3) \\ &= \dot{q}_i^\alpha(t) + \Delta t \tilde{f}_i^\alpha(t) + \frac{1}{2}\Delta t^2 \dot{\tilde{f}}_i^\alpha(t) + O(\Delta t^3). \end{aligned} \tag{2.29}$$

By using $\tilde{f}_i^\alpha(t+\Delta t) = \tilde{f}_i^\alpha(t) + \Delta t \dot{\tilde{f}}_i^\alpha(t) + O(\Delta t^2)$, we evaluate $\dot{\tilde{f}}_i^\alpha(t)$ as

$$\dot{\tilde{f}}_i^\alpha(t) = \frac{\tilde{f}_i^\alpha(t+\Delta t) - \tilde{f}_i^\alpha(t)}{\Delta t} + O(\Delta t). \tag{2.30}$$

Substituting Eq. (2.30) into Eq. (2.29), we obtain [133]

$$\dot{q}_i^\alpha(t+\Delta t) = \dot{q}_i^\alpha(t) + \Delta t \frac{\tilde{f}_i^\alpha(t+\Delta t) + \tilde{f}_i^\alpha(t)}{2} + O(\Delta t^3). \tag{2.31}$$

If the force $\tilde{f}_i^\alpha(t+\Delta t)$ is independent of $\dot{\boldsymbol{q}}$, we can obtain $\tilde{f}_i^\alpha(\boldsymbol{q}(t+\Delta t))$ from $\boldsymbol{q}(t+\Delta t)$ with the aid of Eq. (2.28) [133]. However, if $\tilde{f}_i^\alpha(t+\Delta t)$ depends on $\dot{\boldsymbol{q}}$, we have to evaluate $\tilde{f}_i^\alpha(\boldsymbol{q}(t+\Delta t), \dot{\boldsymbol{q}}(t+\Delta t))$, because $\tilde{f}_i^\alpha(\boldsymbol{q}(t+\Delta t), \dot{\boldsymbol{q}}(t+\Delta t))$ requires LHS of Eq. (2.31). Thus, we adopt the following replacements:

$$\tilde{f}_i^\alpha(t+\Delta t) := \tilde{f}_i^\alpha(\boldsymbol{q}(t+\Delta t), \dot{\boldsymbol{q}}(t+\Delta t)) \to \tilde{f}_i^\alpha(\boldsymbol{q}(t+\Delta t), \dot{\boldsymbol{Q}}(t)), \tag{2.32}$$

$$\tilde{f}_i^\alpha(t) := \tilde{f}_i^\alpha(\boldsymbol{q}(t), \dot{\boldsymbol{q}}(t)) \to \tilde{f}_i^\alpha(\boldsymbol{q}(t), \dot{\boldsymbol{Q}}(t-\Delta t)), \tag{2.33}$$

where we have introduced

$$\dot{Q}_i^\alpha(t) := \dot{q}_i^\alpha(t) + \Delta t \frac{\tilde{f}_i^\alpha(\boldsymbol{q}(t), \dot{\boldsymbol{Q}}(t-\Delta t))}{2}, \tag{2.34}$$

$$\dot{Q}_i^\alpha(t-\Delta t) := \dot{q}_i^\alpha(t-\Delta t) + \Delta t \frac{\tilde{f}_i^\alpha(\boldsymbol{q}(t-\Delta t), \dot{\boldsymbol{Q}}(t-2\Delta t))}{2}. \tag{2.35}$$

Here, the difference between $\tilde{f}_i^\alpha(\boldsymbol{q}(t+\Delta t), \dot{\boldsymbol{q}}(t+\Delta t))$ and $\tilde{f}_i^\alpha(\boldsymbol{q}(t+\Delta t), \dot{\boldsymbol{Q}}(t))$ caused by Eq. (2.32) is given by

$$\begin{aligned}\Delta\tilde{f}_i^\alpha(t+\Delta t) &:= \tilde{f}_i^\alpha(\boldsymbol{q}(t+\Delta t), \dot{\boldsymbol{q}}(t+\Delta t)) - \tilde{f}_i^\alpha(\boldsymbol{q}(t+\Delta t), \dot{\boldsymbol{Q}}(t)) \\ &= \tilde{f}_i^\alpha\left(\boldsymbol{q}(t+\Delta t), \dot{\boldsymbol{q}}(t) + \Delta t \tilde{\boldsymbol{f}}(t) + O(\Delta t^2)\right) \\ &\quad - \tilde{f}_i^\alpha\left(\boldsymbol{q}(t+\Delta t), \dot{\boldsymbol{q}}(t) + \Delta t \frac{\tilde{\boldsymbol{f}}(\boldsymbol{q}(t), \dot{\boldsymbol{q}}(t))}{2} + O(\Delta t^2)\right) \\ &= \Delta t \sum_{j=1}^{N} \sum_{\beta=x,y,\ell} \frac{\tilde{f}_j^\beta(\boldsymbol{q}(t), \dot{\boldsymbol{q}}(t))}{2} \frac{\partial \tilde{f}_i^\alpha(\boldsymbol{q}(t), \dot{\boldsymbol{q}}(t))}{\partial \dot{q}_j^\beta} + O(\Delta t^2). \end{aligned} \tag{2.36}$$

Similarly, the difference between $\tilde{f}_i^\alpha(t) := \tilde{f}_i^\alpha(\boldsymbol{q}(t), \dot{\boldsymbol{q}}(t))$ and $\tilde{f}_i^\alpha(\boldsymbol{q}(t), \dot{\boldsymbol{Q}}(t-\Delta t))$ in Eq. (2.33) can be evaluated as

$$\begin{aligned}\Delta\tilde{f}_i^\alpha(t) &:= \tilde{f}_i^\alpha(\boldsymbol{q}(t), \dot{\boldsymbol{q}}(t)) - \tilde{f}_i^\alpha(\boldsymbol{q}(t), \dot{\boldsymbol{Q}}(t-\Delta t)) \\ &= \Delta t \sum_{j=1}^{N} \sum_{\beta=x,y,\ell} \frac{\tilde{f}_j^\beta(\boldsymbol{q}(t), \dot{\boldsymbol{q}}(t))}{2} \frac{\partial \tilde{f}_i^\alpha(\boldsymbol{q}(t), \dot{\boldsymbol{q}}(t))}{\partial \dot{q}_j^\beta} + O(\Delta t^2). \end{aligned} \tag{2.37}$$

Thus, the replacement of Eqs. (2.32) and (2.33) in Eq. (2.31) with Eqs. (2.36) and (2.37) leads to

$$\begin{aligned}\dot{q}_i^\alpha(t+\Delta t) = \dot{q}_i^\alpha(t) &+ \Delta t \frac{\tilde{f}_i^\alpha(\boldsymbol{q}(t+\Delta t), \dot{\boldsymbol{Q}}(t)) + \tilde{\boldsymbol{f}}(\boldsymbol{q}(t), \dot{\boldsymbol{Q}}(t-\Delta t))}{2} \\ &- \Delta t^2 \sum_{j=1}^{N} \sum_{\beta=x,y,\ell} \frac{\tilde{f}_j^\beta(\boldsymbol{q}(t), \dot{\boldsymbol{q}}(t))}{2} \frac{\partial \tilde{f}_i^\alpha(\boldsymbol{q}(t), \dot{\boldsymbol{q}}(t))}{\partial \dot{q}_j^\beta} + O(\Delta t^3). \end{aligned} \tag{2.38}$$

Omitting the term including $O(\Delta t^2)$ in Eq.(2.38), we obtain the following numerical integration methods for $\dot{\boldsymbol{q}}$:

$$\dot{q}_i^\alpha(t+\Delta t) \to \dot{q}_i^\alpha(t) + \Delta t \frac{\tilde{f}_i^\alpha(\boldsymbol{q}(t+\Delta t), \dot{\boldsymbol{Q}}(t)) + \tilde{\boldsymbol{f}}(\boldsymbol{q}(t), \dot{\boldsymbol{Q}}(t-\Delta t))}{2}. \tag{2.39}$$

Note that Eq. (2.39) is the precise expression of the velocity Verlet scheme for $\dot{\boldsymbol{q}}$ presented in Eq. (2.27). From the comparison between Eqs. (2.38) and (2.39), we have confirmed that the velocity Verlet scheme has the first-order precision of Δt for $\dot{\boldsymbol{q}}$. We also note that if $\tilde{f}_i^\alpha$ is independent of $\dot{\boldsymbol{q}}$ as in the case of Hamiltonian systems, the term proportional to Δt^2 is zero and thus, the second-order accuracy of Δt for $\dot{q}_i^\alpha$ is guaranteed.

Let us go back to Eq. (2.28) with the replacement of Eq. (2.33) for $\tilde{f}_i^\alpha(t)$:

$$\begin{aligned} q_i^\alpha(t+\Delta t) &= q_i^\alpha(t) + \Delta t \dot{q}_i^\alpha(t) + \frac{1}{2}\Delta t^2 \tilde{f}_i^\alpha(t) + O(\Delta t^3) \\ &= q_i^\alpha(t) + \Delta t \dot{q}_i^\alpha(t) + \frac{1}{2}\Delta t^2 \tilde{f}_i^\alpha(\boldsymbol{q}(t), \dot{\boldsymbol{Q}}(t-\Delta t)) + O(\Delta t^3). \end{aligned} \tag{2.40}$$

Omitting the term including $O(\Delta t^3)$ in Eq.(2.40), we obtain the following numerical integration methods for $\boldsymbol{q}$:

$$q_i^\alpha(t+\Delta t) \to q_i^\alpha(t) + \Delta t \dot{q}_i^\alpha(t) + \frac{1}{2}\Delta t^2 \tilde{f}_i^\alpha(\boldsymbol{q}(t), \dot{\boldsymbol{Q}}(t-\Delta t)). \tag{2.41}$$

Here, Eq. (2.41) is the precise expression of the velocity Verlet scheme for $\boldsymbol{q}$ presented in Eq. (2.26). From Eqs. (2.40) and (2.41), we have confirmed that the velocity Verlet scheme has the second-order precision of Δt for $\boldsymbol{q}$.

2.4.2 Implementation of the velocity Verlet method for the force depending on the velocity

In this subsection, we explain how to implement the velocity Verlet method in our system. In this thesis, we adopt the following equations:

$$q_i^\alpha(t+\Delta t) = q_i^\alpha(t) + \Delta t \dot{q}_i^\alpha(t) + \Delta t^2 \frac{\tilde{f}_i^\alpha\left(\boldsymbol{q}(t), \dot{\boldsymbol{Q}}\left(t-\Delta t\right)\right)}{2}, \tag{2.42}$$

$$\dot{Q}_i^\alpha\left(t\right) = \dot{q}_i^\alpha(t) + \Delta t \frac{\tilde{f}_i^\alpha\left(\boldsymbol{q}(t), \dot{\boldsymbol{Q}}\left(t-\Delta t\right)\right)}{2}. \tag{2.43}$$

Here, the updated configuration $q_i^\alpha(t+\Delta t)$ and modified velocity $\dot{Q}_i^\alpha\left(t\right)$ are used to obtain the force $\tilde{f}_i^\alpha\left(\boldsymbol{q}(t+\Delta t), \dot{\boldsymbol{Q}}\left(t\right)\right)$. Then, we update the velocity as follows

$$\dot{q}_i^\alpha(t+\Delta t) = \dot{Q}_i^\alpha\left(t\right) + \Delta t \frac{\tilde{f}_i^\alpha\left(\boldsymbol{q}(t+\Delta t), \dot{\boldsymbol{Q}}\left(t\right)\right)}{2}. \tag{2.44}$$

Chapter 3

Theory of rigidity and density of states of two-dimensional amorphous solids of dispersed frictional grains in the linear response regime

3.1 Introduction of Chapter 3

Amorphous materials consisting of dispersed grains such as powders, colloids, bubbles, and emulsions are ubiquitous in nature [2, 5, 8, 9]. These materials behave like liquids at low densities and exhibit solid-like mechanical responses above their jamming point [10]. In systems consisting of frictionless grains, the rigidity changes continuously, but the coordination number of grains changes discontinuously at the jamming point as a function of density [5, 9, 12]. The critical behavior near the jamming point is of interest to physicists as a non-equilibrium phase transition [11, 16, 18, 20, 33]. Dispersed grains above the jamming point are fragile and exhibit softening and yielding transition under certain loads [67–70, 134–139].

For amorphous solids consisting of frictionless grains, it is useful to analyze the dynamical matrix or the Hessian matrix, which is defined as the second derivative of the potential of a collection of grains with respect to the displacements from their stable configuration [5, 8, 17, 82, 84, 87, 88]. For instance, the rigidity can be determined by eigenvalues and eigenvectors [83, 86, 90, 107–109]. It has been reported that the minimum nonzero eigenvalue of the Hessian ma-

trix decreases with increasing strain and eventually becomes negative, where an irreversible stress drop takes place [107, 108, 111–113].

The density of states (DOS) for systems composed of anisotropic grains, such as ellipses, dimers, deformable grains, and grains with rough surfaces have been studied with the aid of the Hessian matrix [93–103]. Because of the rotation of such anisotropic grains, there exists a rotational band in the DOS that is distinguishable from the translational band [94, 96, 97, 100, 102, 103].

Even for systems of spherical grains that cannot be free from inter-particle friction, similar results are expected as a result of grain rotations. However, few studies have reported the existence of rotational bands in the DOS. Because the frictional force between the grains depends on the contact history, it cannot be expressed as a conservative force. Therefore, stability analysis for frictional grains based on the Hessian cannot be used. Nevertheless, the Hessian analysis using an effective potential for frictional grains has been performed [104, 105]. Recently, Liu et al. suggested that the Hessian analysis with another effective potential can be used even if slip processes exist [106]. The previous studies [104, 105] reported that friction between grains causes a continuous change in the functional form of the DOS from that of frictionless systems. However, there are only a few reports on whether an isolated band in the DOS originating from friction between grains is visible at lower frequencies.

Recently, Chattoraj et al. discussed the stability of the grain configuration under strain using the Jacobian matrix of frictional grains [115]. They performed eigenvalue analysis under athermal quasi-static shear processes and determined the existence of oscillatory instability originating from inter-particle friction at a certain strain [115–117]. However, they did not discuss the rigidity or the DOS.

The theoretical determination of the rigidity of amorphous solids consisting of frictional grains is important for controlling amorphous solids. However, we do not know how to determine the rigidity from the Jacobian for the frictional grains.

The purpose of this chapter is to clarify the role of mutual friction between grains in terms of the rigidity and the DOS. We focus on the response to an infinitesimal strain from a stable configuration of grains without any strain to obtain tangible results. In this study, we assume that there is no slip between grains because of an infinitesimal strain, and we then deal with friction as static friction. We succeed in determining the rigidity in linear response regime. We find that there are two modes in the DOS for sufficiently small k_T/k_N.

The remainder of this chapter is organized as follows. In the next section, we introduce the numerical method. In Sec. 3.3, we introduce the Jacobian. Section 3.4 consists of Sec. 3.4.1, which deals with the DOS, and Sec. 3.4.2, which deals with the theoretical prediction of rigidity in the linear response regime. In the final section, we summarize the results of our study and discuss future work. The appendix consists of five sections. In Appendix A, we summarize some properties of the Jacobian. In Appendix B, we present the explicit expressions of the Jacobian. In Appendix C, we derive the theoretical prediction of rigidity using the Jacobian. In Appendix D, we investigate the effects of rattlers. In

Appendix E, we introduce the DOS using the Hessian analysis.

3.2 Numerical Model Used in this Chapter

Our system contains N frictional spherical grains embedded in a monolayer configuration. We treat this system as a two-dimensional system (see Fig. 3.1). To

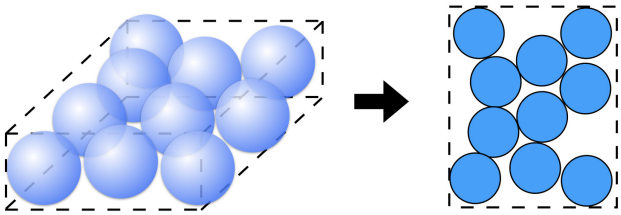

Figure 3.1: Schematics of our system.

prevent the system from crystallizing [78], we prepare an equal number of grains with diameters d and $d/1.4$. We assume that the mass of grain i is proportional to d_i^2, where d_i is the diameter of i-th grain. We introduce m as the mass of a grain with diameter d. In this study, x_i, y_i, and θ_i denote x, y coordinates, and the rotational angle of the i-th grain, respectively. We introduce the generalized coordinates of the i-th grain $\boldsymbol{q}_i := (\boldsymbol{r}_i^{\mathrm{T}}, \ell_i)^{\mathrm{T}} := (x_i, y_i, d_i\theta_i/2)^{\mathrm{T}}$, where the superscript T denotes the transposition.

Let the force, and z-component of the torque acting on the i-th grain be $\boldsymbol{F}_i := (F_i^x, F_i^y)^{\mathrm{T}}$ and T_i, respectively. Then, the equations of motion of i-th grain are expressed as

$$m_i \frac{d^2\boldsymbol{r}_i}{dt^2} = \boldsymbol{F}_i, \tag{3.1}$$

$$I_i \frac{d^2\theta_i}{dt^2} = T_i, \tag{3.2}$$

with the mass m_i and the momentum of inertia $I_i := m_i d_i^2/8$ of i-th grain. In a system without volume forces such as gravity, we can write

$$\boldsymbol{F}_i = \sum_{j\neq i} \boldsymbol{f}_{ij}, \tag{3.3}$$

$$T_i = \sum_{j\neq i} T_{ij}, \tag{3.4}$$

where $\boldsymbol{f}_{ij}$ and T_{ij} are the force and z-component of the torque acting on the i-th grain from the j-th grain, respectively. Here, T_{ij} is given by

$$T_{ij} = -\frac{d_i}{2}(n_{ij}^x f_{ij}^y - n_{ij}^y f_{ij}^x), \tag{3.5}$$

where we have introduced the normal unit vector between i and j grains as $\boldsymbol{n}_{ij} := \boldsymbol{r}_{ij}/|\boldsymbol{r}_{ij}| := (\boldsymbol{r}_i - \boldsymbol{r}_j)/|\boldsymbol{r}_i - \boldsymbol{r}_j|$. Here, n_{ij}^ζ and f_{ij}^ζ refer to ζ-components of $\boldsymbol{n}_{ij}$ and $\boldsymbol{f}_{ij}$, respectively. Note that ζ expresses $\zeta = x$ or y throughout this study. The force $\boldsymbol{f}_{ij}$ can be divided into normal $\boldsymbol{f}_{N,ij}$ and tangential $\boldsymbol{f}_{T,ij}$ parts as

$$\boldsymbol{f}_{ij} = (\boldsymbol{f}_{N,ij} + \boldsymbol{f}_{T,ij})H(d_{ij}/2 - |\boldsymbol{r}_{ij}|), \tag{3.6}$$

where $d_{ij} := d_i + d_j$ and $H(x)$ is Heaviside's step function, taking $H(x) = 1$ for $x > 0$ and $H(x) = 0$ otherwise. We model the repulsive force between the contacted grains i and j as the Hertzian force in addition to the dissipative force proportional to the relative velocity with a damping constant η_D [106] as follows:

$$\boldsymbol{f}_{N,ij} := k_N \xi_{N,ij}^{3/2} \boldsymbol{n}_{ij} - \eta_D \boldsymbol{v}_{N,ij}, \tag{3.7}$$

$$\boldsymbol{f}_{T,ij} := k_T \xi_{N,ij}^{1/2} \xi_{T,ij} \boldsymbol{t}_{ij} - \eta_D \boldsymbol{v}_{T,ij}, \tag{3.8}$$

where k_N and k_T are the stiffness parameters of normal and tangential contacts, respectively. For the normal compression and its velocity we have used $\xi_{N,ij} := d_{ij}/2 - |\boldsymbol{r}_{ij}|$ and $\boldsymbol{v}_{N,ij} := \dot{\boldsymbol{r}}_{ij} \cdot \boldsymbol{n}_{ij}$, respectively. For the tangential deformation, with the aid of $\boldsymbol{u}_{ij} := (n_{ij}^y, -n_{ij}^x)^{\mathrm{T}}$, the tangential velocity $\boldsymbol{v}_{T,ij}$ is defined as $\boldsymbol{v}_{T,ij} := \dot{\boldsymbol{r}}_{ij} - \boldsymbol{v}_{N,ij} + \boldsymbol{u}_{ij}(d_i\omega_i + d_j\omega_j)/2$, where we have introduced

$$\boldsymbol{\xi}_{T,ij} := \int_{C_{ij}} dt \boldsymbol{v}_{T,ij} - \left[\left(\int_{C_{ij}} dt \boldsymbol{v}_{T,ij} \right) \cdot \boldsymbol{n}_{ij} \right] \boldsymbol{n}_{ij}, \tag{3.9}$$

with $\xi_{T,ij} := |\boldsymbol{\xi}_{T,ij}|$ and $\boldsymbol{t}_{ij} := -\boldsymbol{\xi}_{T,ij}/|\xi_{T,ij}|$. Here, $\dot{\boldsymbol{A}} := d\boldsymbol{A}/dt$ and $\int_{C_{ij}} dt$ is the integration over the duration time of contact between i and j grains. Although the dissipative force between grains interacting with the Hertzian force is proportional to the product of the relative velocity and $\xi_{ij,N}^{1/2}$ [129–131], we adopt simple dissipative forces as in Eqs. (3.7) and (3.8) because we are not interested in the relaxation dynamics. We note that Eqs. (3.7) and (3.8) assume the Hertzian contact force for the static repulsion of contacting spheres, but all calculations in this study are those for two-dimensional systems. Here, we do not consider the effects of slips in the tangential equation of motion. This treatment can be justified if we restrict our interest in the linear response regime to a stable configuration of grains without any strain. This situation corresponds to frictional grains with infinitely large dynamical friction constant, in which the friction is only characterized by static friction. Therefore, our analysis does not apply to systems with finite strain [72], where the effect of slip is important.

To generate a stable configuration of frictional grains, we prepare a stable configuration of frictionless grains in a square box of linear size L using a fast inertial relaxation engine (FIRE) [118]. Subsequently, we turn on the tangential force using Eqs. (3.1) and (3.2) to achieve a stable configuration in the force-balanced (FB) state for frictional grain[1] (see Sec. 2.3 for details). Here, the FB state satisfies the FB conditions $|F_i^\zeta| = 0$ and $|T_i| = 0$ for arbitrary grains. Note that we set $\theta_i = 0$ when the tangential force is turned on.

We impose the Lees-Edwards boundary condition [140, 141], where the direction parallel to the shear strain is x-direction. After applying a step strain $\Delta\gamma$ to all grains, x-coordinate of the position of the i-th grain is shifted by an affine displacement $\Delta x_i(\Delta\gamma) := \Delta\gamma y_i^{\rm FB}(0)$, where the superscript FB denotes the FB state. The system is then relaxed to the FB state by the contact forces between the grains expressed in Eqs. (3.7) and (3.8). Here, ζ-components of translational $\Delta\mathring{r}_i^\zeta(\Delta\gamma)$ and rotational $\Delta\mathring{\ell}_i(\Delta\gamma)$ nonaffine displacements of the i-th grain after the relaxation process are, respectively, defined as follows:

$$\Delta\mathring{r}_i^\zeta(\Delta\gamma) := r_i^{{\rm FB},\zeta}(\Delta\gamma) - r_i^{{\rm FB},\zeta}(0) - \delta_{\zeta x}\Delta\gamma y_i^{\rm FB}(0), \tag{3.10}$$

$$\Delta\mathring{\ell}_i := \ell_i^{\rm FB}(\Delta\gamma) - \ell_i^{\rm FB}(0). \tag{3.11}$$

Using Eqs. (3.10) and (3.11), we introduce the rate of nonaffine displacements as:

$$\begin{aligned}\frac{d\mathring{r}_i^\zeta}{d\gamma} &:= \lim_{\Delta\gamma\to 0}\frac{\Delta\mathring{r}_i^\zeta(\Delta\gamma)}{\Delta\gamma}\\ &= \lim_{\Delta\gamma\to 0}\frac{r_i^{{\rm FB},\zeta}(\Delta\gamma) - r_i^{{\rm FB},\zeta}(0)}{\Delta\gamma} - \delta_{\zeta x}y_i^{\rm FB}(0),\end{aligned} \tag{3.12}$$

$$\begin{aligned}\frac{d\mathring{\ell}_i}{d\gamma} &:= \lim_{\Delta\gamma\to 0}\frac{\Delta\mathring{\ell}_i(\Delta\gamma)}{\Delta\gamma}\\ &= \lim_{\Delta\gamma\to 0}\frac{\ell_i^{\rm FB}(\Delta\gamma) - \ell_i^{\rm FB}(0)}{\Delta\gamma}.\end{aligned} \tag{3.13}$$

[1]For simplicity, we prepare the configuration before applying shear for frictionless grains at first, and then considered the friction between grains. If we prepare a configuration before applying shear by compressing frictional grains, we confirm that the configuration had an oscillatory instability that resulted from the appearance of a pair of imaginary eigenvalues of the Jacobian divided by mass matrix: $\lambda' = \lambda'_r \pm i\lambda'_i$ [115–117], where λ', λ'_r, and λ'_i are the complex, real, and imaginary eigenvalues of $M^{-1}\mathcal{J}$, respectively. Here, $\mathcal{J}$ is the Jacobian defined in Eq. (3.20), and M is the mass matrix whose explicit form is given by $M = \begin{bmatrix} M_1 & & \\ & \ddots & \\ & & M_N \end{bmatrix}$, where $M_i := \begin{bmatrix} m_i & & \\ & m_i & \\ & & 4I_i/d_i^2 \end{bmatrix}$. Because the linearized equation of motion is expressed as $d^2q_i^\alpha/dt^2 = -\sum_{k,\kappa}\sum_{j,\beta}(M_{ik}^{\alpha\kappa})^{-1}\mathcal{J}_{kj}^{\kappa\beta}q_j^\beta$, there are four fundamental solutions $\boldsymbol{q} \propto e^{i\omega'_n t}$, where $i\omega'_n$ consists of $i\omega'_{\pm 1} = \omega'_i \pm i\omega'_r$ and $i\omega'_{\pm 2} = -\omega'_i \pm i\omega'_r$. Here, ω'_r and ω'_i satisfy the relation $\omega'_r \pm i\omega'_i = \sqrt{\lambda'_r \pm i\lambda'_i}$. Thus, to avoid the oscillatory instability of the configuration before applying shear, we adopt the protocol of creating the configuration with frictionless grains, and then let the system relax by adding static friction between grains.

Our system is characterized by the generalized coordinate

$$\boldsymbol{q}(\gamma) := (\boldsymbol{q}_1^{\mathrm{T}}(\gamma), \boldsymbol{q}_2^{\mathrm{T}}(\gamma), \cdots, \boldsymbol{q}_N^{\mathrm{T}}(\gamma))^{\mathrm{T}}. \tag{3.14}$$

The configuration in the FB state at strain γ is denoted as

$$\boldsymbol{q}^{\mathrm{FB}}(\gamma) := ((\boldsymbol{q}_1^{\mathrm{FB}}(\gamma))^{\mathrm{T}}, (\boldsymbol{q}_2^{\mathrm{FB}}(\gamma))^{\mathrm{T}}, \cdots, (\boldsymbol{q}_N^{\mathrm{FB}}(\gamma))^{\mathrm{T}})^{\mathrm{T}}. \tag{3.15}$$

The shear stress $\sigma_{xy}(\gamma)$ at $\boldsymbol{q}^{\mathrm{FB}}(\gamma)$ for one sample is given by:

$$\sigma_{xy}(\boldsymbol{q}^{\mathrm{FB}}(\gamma)) = -\frac{1}{L^2}\sum_i \sum_{j>i} f_{ij}^x(\boldsymbol{q}^{\mathrm{FB}}(\gamma)) r_{ij}^y(\boldsymbol{q}^{\mathrm{FB}}(\gamma)). \tag{3.16}$$

The rigidity g in the linear response regime for one sample is defined as

$$g := \left.\frac{d\sigma_{xy}(\boldsymbol{q}(\gamma))}{d\gamma}\right|_{\boldsymbol{q}(\gamma)=\boldsymbol{q}^{\mathrm{FB}}(0)}, \tag{3.17}$$

where the differentiation on the right-hand side (RHS) of Eq. (3.17) is defined as follows:

$$\left.\frac{d\sigma_{xy}(\boldsymbol{q}(\gamma))}{d\gamma}\right|_{\boldsymbol{q}(\gamma)=\boldsymbol{q}^{\mathrm{FB}}(0)} := \lim_{\Delta\gamma\to 0} \frac{\sigma_{xy}(\boldsymbol{q}^{\mathrm{FB}}(\Delta\gamma)) - \sigma_{xy}(\boldsymbol{q}^{\mathrm{FB}}(0))}{\Delta\gamma}. \tag{3.18}$$

In the numerical calculation, we use a non-zero but sufficiently small $\Delta\gamma$ for the evaluation of g. Then, the rigidity G in the linear response regime is defined as

$$G := \langle g \rangle, \tag{3.19}$$

where $\langle\cdot\rangle$ is the ensemble average.

For the numerical FB condition, we use the condition $|\tilde{F}_i^\alpha| < F_{\mathrm{Th}}$ for arbitrary i, where F_{Th} is the threshold force for the simulation and $\tilde{\boldsymbol{F}}_i$ is the generalized force, defined as $\tilde{\boldsymbol{F}}_i := (\tilde{F}_i^x, \tilde{F}_i^y, \tilde{F}_i^\ell)^{\mathrm{T}} := (F_i^x, F_i^y, 2T_i/d_i)^{\mathrm{T}}$.

In our simulation, we adopt $\eta_D = (mk_N)^{1/2}d^{1/4}$ and $F_{\mathrm{Th}} = 1.0\times 10^{-14} k_N d^{3/2}$. The control parameters are the ratio of the tangential to normal stiffness k_T/k_N and projected area fraction to two-dimensional space ϕ. The operating ranges of k_T/k_N and ϕ are 0.0 to 10.0 and 0.83 to 0.90, respectively. In this study, we mainly present the results for $N = 1024$ and $\Delta\gamma = 1.0 \times 10^{-6}$ with the ensemble averages of 10 samples for each k_T/k_N and ϕ. Some results are obtained with $N = 128$, $\Delta\gamma = 1.0 \times 10^{-6}$, and five samples for each k_T/k_N and ϕ. We verify that the results are independent of the choice of $\Delta\gamma$ for $1.0 \times 10^{-6} \le \Delta\gamma \le 1.0 \times 10^{-4}$. We ignore the effect of dissipation between grains because the velocity of each grain is sufficiently small for infinitesimal agitation from the FB state. The time step of the simulation, Δt, was set to $\Delta t = 1.0 \times 10^{-2} t_0$, and numerical integration was performed using the velocity Verlet method (see Sec. 2.4), where $t_0 := (m/k_N)^{1/2} d^{-1/4}$.

Figure 3.2 (a) shows an example of the affine displacements of grains, where the displacements exist only in the shear direction, and Fig. 3.2 (b) shows the nonaffine displacements.

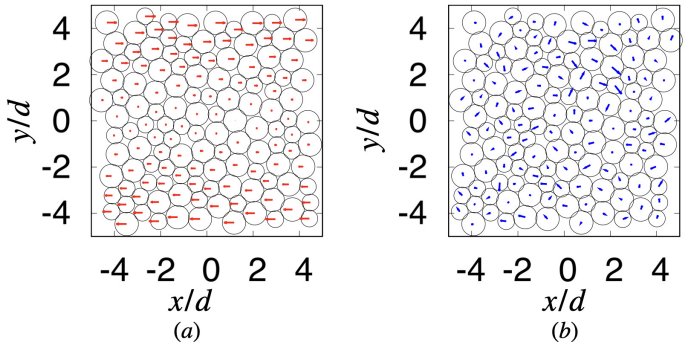

Figure 3.2: Plots of (a) affine displacements and (b) nonaffine displacements of grains with $\Delta\gamma = 1.0 \times 10^{-6}$. Here, the magnitudes of the vectors are multiplied by (a) $0.1\Delta\gamma^{-1}$ and (b) $5.0\Delta\gamma^{-1}$ for the visualization. These figures are based on numerical results for $N = 128$.

3.3 Theoretical Analysis

In this section, we introduce the Jacobian, the DOS, and theoretical expressions of the linear rigidity. Here, we omit the effects of $\dot{\boldsymbol{q}}$ because the dissipative term proportional to $\dot{\boldsymbol{q}}$ vanishes under quasistatic shear.

3.3.1 Jacobian and the DOS for frictional grains

In frictional systems, the stability of the system and DOS at $\boldsymbol{q}^{\mathrm{FB}}(\gamma)$ are analyzed using the Jacobian ($\mathcal{J}$) defined as [115]:

$$\mathcal{J}_{ij}^{\alpha\beta} := -\left.\frac{\partial \tilde{F}_i^{\alpha}(\boldsymbol{q}(\gamma))}{\partial q_j^{\beta}}\right|_{\boldsymbol{q}(\gamma)=\boldsymbol{q}^{\mathrm{FB}}(0)}, \tag{3.20}$$

where α and β are any of x, y and ℓ, while i and j express grain indices. Therefore, the Jacobian matrix, which is a $3N \times 3N$ matrix, can be written as

$$\mathcal{J} = \begin{bmatrix} \mathcal{J}_{11} & \cdots & \mathcal{J}_{1i} & \cdots & \mathcal{J}_{1j} & \cdots & \mathcal{J}_{1N} \\ \vdots & \ddots & \vdots & & \vdots & & \vdots \\ \mathcal{J}_{i1} & \cdots & \mathcal{J}_{ii} & \cdots & \mathcal{J}_{ij} & \cdots & \mathcal{J}_{iN} \\ \vdots & & \vdots & \ddots & \vdots & & \vdots \\ \mathcal{J}_{j1} & \cdots & \mathcal{J}_{ji} & \cdots & \mathcal{J}_{jj} & \cdots & \mathcal{J}_{jN} \\ \vdots & & \vdots & & \vdots & \ddots & \vdots \\ \mathcal{J}_{N1} & \cdots & \mathcal{J}_{Ni} & \cdots & \mathcal{J}_{Nj} & \cdots & \mathcal{J}_{NN} \end{bmatrix}, \tag{3.21}$$

where $\mathcal{J}_{ij}$ is a 3×3 submatrix of the Jacobian $\mathcal{J}$ for a pair of grains i and j:

$$\mathcal{J}_{ij} = \begin{bmatrix} \mathcal{J}_{ij}^{xx} & \mathcal{J}_{ij}^{xy} & \mathcal{J}_{ij}^{x\ell} \\ \mathcal{J}_{ij}^{yx} & \mathcal{J}_{ij}^{yy} & \mathcal{J}_{ij}^{y\ell} \\ \mathcal{J}_{ij}^{\ell x} & \mathcal{J}_{ij}^{\ell y} & \mathcal{J}_{ij}^{\ell\ell} \end{bmatrix}. \tag{3.22}$$

See Appendices A and B for detailed properties of the Jacobian. The right and left eigenvalue equations of $\mathcal{J}$ are, respectively, given by

$$\mathcal{J} \left| R_n \right\rangle = \lambda_n \left| R_n \right\rangle, \tag{3.23}$$

$$\left\langle L_n \right| \mathcal{J} = \lambda_n \left\langle L_n \right|, \tag{3.24}$$

where $|R_n\rangle$ and $\langle L_n|$ are the right and left eigenvectors corresponding to λ_n, respectively. Here, λ_n is the n-th eigenvalue of $\mathcal{J}$. Note that $|R_n\rangle$ and $\langle L_n|$ satisfy the orthonormal relation $\langle L_m|R_n\rangle = \delta_{mn}$ with normalization $\langle R_n|R_n\rangle = \langle L_n|L_n\rangle = 1$, if all eigenstates are non-degenerate. Here, the inner products for the right and left eigenvectors are defined as $\langle R_n|R_n\rangle = \sum_{i=1}^{N} \sum_{\alpha=x,y,\ell} |R_{n,i}^{\alpha}|^2$ and $\langle L_n|L_n\rangle = \sum_{i=1}^{N} \sum_{\alpha=x,y,\ell} |L_{n,i}^{\alpha}|^2$, respectively. In the presence of friction, the eigenvalue λ_n is generally a complex number, but if we restrict our interest to infinitesimal distortions from stable configurations without shear strain, λ_n becomes real and can be expressed as $\lambda_n = \omega_n^2$. The DOS is the distribution function of the eigenvalues, defined as:

$$D(\omega) := \frac{1}{3N} \sum_{n=1}^{3N} \langle \delta(\omega - \omega_n) \rangle. \tag{3.25}$$

Using the force decomposition, the Jacobian can also be divided into

$$\mathcal{J}_{ij}^{\alpha\beta} = \mathcal{J}_{N,ij}^{\alpha\beta} + \mathcal{J}_{T,ij}^{\alpha\beta}, \tag{3.26}$$

where

$$\mathcal{J}_{N,ij}^{\alpha\beta} := \left. \frac{\partial \tilde{f}_{N,ij}^{\alpha}(\boldsymbol{q}(\gamma))}{\partial q_j^{\beta}} \right|_{\boldsymbol{q}(\gamma)=\boldsymbol{q}^{\mathrm{FB}}(\gamma)}, \tag{3.27}$$

$$\mathcal{J}_{T,ij}^{\alpha\beta} := \left. \frac{\partial \tilde{f}_{T,ij}^{\alpha}(\boldsymbol{q}(\gamma))}{\partial q_j^{\beta}} \right|_{\boldsymbol{q}(\gamma)=\boldsymbol{q}^{\mathrm{FB}}(\gamma)} \tag{3.28}$$

for $i \neq j$ and

$$\mathcal{J}_{N,ij}^{\alpha\beta} := \sum_{(i,k)} \left. \frac{\partial \tilde{f}_{N,ik}^{\alpha}(\boldsymbol{q}(\gamma))}{\partial q_i^{\beta}} \right|_{\boldsymbol{q}(\gamma)=\boldsymbol{q}^{\mathrm{FB}}(\gamma)}, \tag{3.29}$$

$$\mathcal{J}_{T,ij}^{\alpha\beta} := \sum_{(i,k)} \left. \frac{\partial \tilde{f}_{T,ik}^{\alpha}(\boldsymbol{q}(\gamma))}{\partial q_i^{\beta}} \right|_{\boldsymbol{q}(\gamma)=\boldsymbol{q}^{\mathrm{FB}}(\gamma)} \tag{3.30}$$

for $i = j$. Here, we have introduced $\tilde{\boldsymbol{f}}_{N,ij} := (\tilde{f}^x_{N,ij}, \tilde{f}^y_{N,ij}, \tilde{f}^\ell_{N,ij})^{\mathrm{T}} := (f^x_{N,ij}, \tilde{f}^y_{N,ij}, 0)^{\mathrm{T}}$ and $\tilde{\boldsymbol{f}}_{T,ij} := (\tilde{f}^x_{T,ij}, \tilde{f}^y_{T,ij}, \tilde{f}^\ell_{T,ij})^{\mathrm{T}} := (f^x_{T,ij}, \tilde{f}^y_{T,ij}, 2T_{ij}/d_i)^{\mathrm{T}}$, where $f^\zeta_{N,ij}$ and $f^\zeta_{T,ij}$ are ζ-component of $\boldsymbol{f}_{N,ij}$ and $\boldsymbol{f}_{T,ij}$, respectively. Note that $\sum_{(i,j)}$ denotes the summation for contacted grains of the i-th grain. The explicit expressions of $\mathcal{J}^{\alpha\beta}_{N,ij}$ and $\mathcal{J}^{\alpha\beta}_{T,ij}$ are presented in the Appendix B.2.

3.3.2 Expressions of the linear rigidity via eigenmodes

Let us introduce $|\tilde{F}(\boldsymbol{q}(\gamma))\rangle$ as

$$|\tilde{F}(\boldsymbol{q}(\gamma))\rangle := [\tilde{\boldsymbol{F}}^{\mathrm{T}}_1(\boldsymbol{q}(\gamma)), \tilde{\boldsymbol{F}}^{\mathrm{T}}_2(\boldsymbol{q}(\gamma)), \cdots, \tilde{\boldsymbol{F}}^{\mathrm{T}}_N(\boldsymbol{q}(\gamma))]^{\mathrm{T}}. \tag{3.31}$$

Because the forces acting on the grains are balanced in the FB state, $|\tilde{F}(\boldsymbol{q}(\gamma))\rangle\,|_{\boldsymbol{q}(\gamma)=\boldsymbol{q}^{\mathrm{FB}}(\gamma)}$ satisfies

$$|\tilde{F}(\boldsymbol{q}(\gamma))\rangle\Big|_{\boldsymbol{q}(\gamma)=\boldsymbol{q}^{\mathrm{FB}}(\gamma)} = |0\rangle\,, \tag{3.32}$$

where $|0\rangle$ is the ket vector containing 0 for all components. The stable configuration in the FB state satisfies

$$\frac{d\,|\tilde{F}(\boldsymbol{q}(\gamma))\rangle}{d\gamma}\bigg|_{\boldsymbol{q}(\gamma)=\boldsymbol{q}^{\mathrm{FB}}(0)} = |0\rangle\,, \tag{3.33}$$

where

$$\begin{aligned}\frac{d\,|\tilde{F}(\boldsymbol{q}(\gamma))\rangle}{d\gamma}\bigg|_{\boldsymbol{q}(\gamma)=\boldsymbol{q}^{\mathrm{FB}}(0)} &:= \lim_{\Delta\gamma\to 0}\frac{\left|\tilde{F}(\boldsymbol{q}^{\mathrm{FB}}(\Delta\gamma))\right\rangle - \left|\tilde{F}(\boldsymbol{q}^{\mathrm{FB}}(0))\right\rangle}{\Delta\gamma}.\end{aligned} \tag{3.34}$$

Introducing

$$\left|\frac{d\mathring{q}}{d\gamma}\right\rangle := \left[\frac{d\mathring{r}^x_1}{d\gamma}, \frac{d\mathring{r}^y_1}{d\gamma}, \frac{d\mathring{\ell}_1}{d\gamma}, \cdots, \frac{d\mathring{r}^x_N}{d\gamma}, \frac{d\mathring{r}^y_N}{d\gamma}, \frac{d\mathring{\ell}_N}{d\gamma}\right]^{\mathrm{T}}, \tag{3.35}$$

the left-hand side (LHS) of Eq.(3.33) can be rewritten as:

$$\frac{d\,|\tilde{F}(\boldsymbol{q}(\gamma))\rangle}{d\gamma}\bigg|_{\boldsymbol{q}(\gamma)=\boldsymbol{q}^{\mathrm{FB}}(0)} = -\,|\Xi\rangle + \tilde{\mathcal{J}}\left|\frac{d\mathring{q}}{d\gamma}\right\rangle, \tag{3.36}$$

where we have used Eqs. (3.12) and (3.13) (see Appendix C.1). The first and second terms on RHS of Eq. (3.36) represent the strain derivatives of the forces for the contributions from the affine and nonaffine displacements, respectively.

The explicit form of $|\Xi\rangle$ is given by:

$$|\Xi\rangle := \begin{bmatrix} \sum_{j\neq 1} \mathcal{J}^{xx}_{N,j1} r^y_{1j} \\ \sum_{j\neq 1} \mathcal{J}^{xy}_{N,j1} r^y_{1j} \\ \sum_{j\neq 1} \mathcal{J}^{x\ell}_{N,j1} r^y_{1j} \\ \vdots \\ \sum_{j\neq N} \mathcal{J}^{xx}_{N,jN} r^y_{Nj} \\ \sum_{j\neq N} \mathcal{J}^{xy}_{N,jN} r^y_{Nj} \\ \sum_{j\neq N} \mathcal{J}^{x\ell}_{N,jN} r^y_{Nj} \end{bmatrix}. \tag{3.37}$$

Note that the tangential displacements do not contribute to $|\Xi\rangle$. This is because the affine displacements are applied to our system instantaneously as a step strain; thus, the integral interval of the tangential displacement during the affine deformation is zero. We have used $\tilde{\mathcal{J}}$ in Eq. (3.36) defined as

$$\tilde{\mathcal{J}}^{\alpha\beta}_{ii} := \begin{cases} -\mathcal{J}^{\ell x}_{ii} & (\alpha = \ell,\ \beta = x) \\ -\mathcal{J}^{\ell y}_{ii} & (\alpha = \ell,\ \beta = y) \\ \mathcal{J}^{\alpha\beta}_{ii} & (\text{otherwise}) \end{cases} \tag{3.38}$$

and

$$\tilde{\mathcal{J}}^{\alpha\beta}_{ij} := \begin{cases} -\mathcal{J}^{x\ell}_{ij} & (\alpha = x,\ \beta = \ell) \\ -\mathcal{J}^{y\ell}_{ij} & (\alpha = y,\ \beta = \ell) \\ \mathcal{J}^{\alpha\beta}_{ij} & (\text{otherwise}) \end{cases} \tag{3.39}$$

for $i \neq j$.

Expanding the nonaffine displacements by the eigenfunctions of $\tilde{\mathcal{J}}$ and using the fact that the LHS in Eq. (3.36) is zero, we obtain

$$\left| \frac{d\mathring{q}}{d\gamma} \right\rangle = {\sum_n}' \frac{\langle \tilde{L}_n | \Xi \rangle}{\tilde{\lambda}_n} |\tilde{R}_n\rangle, \tag{3.40}$$

where $\tilde{\lambda}_n, \langle \tilde{L}_n|$, and $|\tilde{R}_n\rangle$ are the n-th eigenvalue of $\tilde{\mathcal{J}}$, and the left and right eigenvectors corresponding to $\tilde{\lambda}_n$, respectively. Here, $\sum'_n$ on RHS of Eq. (3.40) excludes low-frequency modes for $\tilde{\lambda}_n t_0^2/m \leq 10^{-12}$ to maintain the numerical accuracy. Note that $|\tilde{R}_n\rangle$ and $\langle \tilde{L}_n|$ satisfy the orthonormal relation $\langle \tilde{L}_m | \tilde{R}_n \rangle = \delta_{mn}$, if all eigenstates are non-degenerate. See Appendix C.1 for the derivation of Eq. (3.40).

The rigidity in the linear response regime under infinitesimal strain $\Delta\gamma$ is decomposed into two parts:

$$G := G_{\mathrm{A}} + G_{\mathrm{NA}}, \tag{3.41}$$

where G_{A} and G_{NA} are the rigidities corresponding to the affine and nonaffine displacements, respectively. With the aid of Eqs. (3.16), (3.19), and (3.39) the

expressions of $G_{\rm A}$ and $G_{\rm NA}$ are, respectively, given by (see Appendix C.2)

$$G_{\rm A} := \frac{1}{2L^2}\left\langle \sum_{i,j(i\neq j)} (r_{ij}^y)^2 \mathcal{J}_{N,ji}^{xx} \right\rangle, \tag{3.42}$$

$$G_{\rm NA} := \frac{1}{2L^2}\left\langle \sum_{i,j(i\neq j)} \left[\sum_{\zeta=x,y} r_{ij}^y \tilde{\mathcal{J}}_{ij}^{x\zeta} \frac{d\mathring{r}_{ij}^{\zeta}}{d\gamma} - r_{ij}^y \tilde{\mathcal{J}}_{ij}^{x\ell} \frac{d\mathring{\ell}_{ij}}{d\gamma} \right] \right\rangle, \tag{3.43}$$

where we have introduced

$$\frac{d\mathring{r}_{ij}^{\zeta}}{d\gamma} := \frac{d\mathring{r}_{i}^{\zeta}}{d\gamma} - \frac{d\mathring{r}_{j}^{\zeta}}{d\gamma}, \tag{3.44}$$

$$\frac{d\mathring{\ell}_{ij}}{d\gamma} := \frac{d\mathring{\ell}_{i}}{d\gamma} + \frac{d\mathring{\ell}_{j}}{d\gamma}. \tag{3.45}$$

Substituting Eq. (3.40) into Eq. (3.43), $G_{\rm NA}$ can be rewritten as follows:

$$G_{\rm NA} = -\frac{1}{L^2}\left\langle {\sum_n}' \frac{\langle \tilde{L}_n|\Xi\rangle \langle\Theta|\tilde{R}_n\rangle}{\tilde{\lambda}_n} \right\rangle, \tag{3.46}$$

where we have introduced

$$\langle\Theta| := \begin{bmatrix} \sum_{j\neq 1} r_{1j}^y \tilde{\mathcal{J}}_{j1}^{xx} \\ \sum_{j\neq 1} r_{1j}^y \tilde{\mathcal{J}}_{j1}^{xy} \\ \sum_{j\neq 1} r_{1j}^y \tilde{\mathcal{J}}_{j1}^{x\ell} \\ \vdots, \\ \sum_{j\neq N} r_{Nj}^y \tilde{\mathcal{J}}_{jN}^{xx} \\ \sum_{j\neq N} r_{Nj}^y \tilde{\mathcal{J}}_{jN}^{xy} \\ \sum_{j\neq N} r_{Nj}^y \tilde{\mathcal{J}}_{jN}^{x\ell} \end{bmatrix}^{\rm T}. \tag{3.47}$$

The affine rigidity can be also expressed as

$$G_{\rm A} = \frac{1}{L^2}\left\langle \langle Y|\Xi\rangle \right\rangle, \tag{3.48}$$

where

$$\langle Y| := \left[r_{1j}^y, 0, 0, r_{2j}^y, 0, 0, \cdots, r_{Nj}^y, 0, 0 \right]. \tag{3.49}$$

3.4 Results

In this section, we present the results of eigenvalue analysis and rigidity based on the formulation explained in the previous section. Section 3.4.1 clarifies the effects of translational and rotational motions on the DOS. In Sec. 3.4.2, rigidity is determined using the eigenmodes of the Jacobian.

3.4.1 Eigenvalue analysis

In Fig. 3.3 we present some typical right eigenvectors $|R_n\rangle$, which was introduced in Eq. (3.23), and can be expressed as:

$$|R_n\rangle = \begin{bmatrix} \boldsymbol{R}_{n,1} \\ \boldsymbol{R}_{n,2} \\ \vdots \\ \boldsymbol{R}_{n,N} \end{bmatrix}, \tag{3.50}$$

where $\boldsymbol{R}_{n,i} := (R^x_{n,i}, R^y_{n,i}, R^\ell_{n,i})^{\mathrm{T}}$. Figure 3.3 illustrates vectors $(R^x_{n,i}, R^y_{n,i})^{\mathrm{T}}$ and colors to characterize the rotation $R^\ell_{n,i}$ of grain i for some characteristic ω_n with $k_T/k_N = 1.0\times10^{-8}$ (Figs. 3.3 (a1)-(a3)) and $k_T/k_N = 1.0\times10^{-4}$ (Figs. 3.3 (b1)-(b3)). Figures 3.3 (a1) and (b1) show the eigenvectors at $\omega_n t_0 = 1.0\times10^{-2}$ and $\omega_n t_0 = 1.0\times10^{-4}$, respectively, which are dominated by the rotational modes. In Fig. 3.3 (a2), we confirm that the eigenvector at $\omega_n t_0 = 1.3\times10^{-2}$ is expressed only by translational modes, whereas the eigenvector at $\omega_n t_0 = 1.3\times10^{-2}$ shown in Fig. 3.3 (b2) is expressed as a coupling mode of the rotational and translational modes. In Figs. 3.3 (a3) and (b3), we show the eigenvectors at $\omega_n t_0 = 1.0$ which are dominated by the translational modes.

To clarify the translational and rotational contributions at each eigenvalue, we compute the translational and rotational participation fractions [96, 98] defined as

$$\psi^T_n := \sum_{i=1}^{N} \left[|R^x_{n,i}|^2 + |R^y_{n,i}|^2 \right], \tag{3.51}$$

$$\psi^R_n := \sum_{i=1}^{N} |R^\ell_{n,i}|^2 = 1 - \psi^T_n, \tag{3.52}$$

respectively. Note that translational mode is dominant when ψ^T_n is close to 1 and rotational mode is dominant when ψ^R_n is close to 1. $\psi^T(\omega)$ and $\psi^R(\omega)$ are plotted for various k_T/k_N in Fig. 3.4, where

$$\psi^T(\omega) := \frac{\sum_{n=1}^{3N} \langle \psi^T_n \delta(\omega - \omega_n) \rangle}{\sum_{n=1}^{3N} \langle \delta(\omega - \omega_n) \rangle}, \tag{3.53}$$

$$\psi^R(\omega) := \frac{\sum_{n=1}^{3N} \langle \psi^R_n \delta(\omega - \omega_n) \rangle}{\sum_{n=1}^{3N} \langle \delta(\omega - \omega_n) \rangle}. \tag{3.54}$$

Here, ψ^T and ψ^R are set to zero if there is no right eigenvalue for $\omega^{(s)} < \omega t_0 < \omega^{(s+1)}$ with the s-th data point for the logarithmic scale $\omega^{(s)}$. Note that the range of ω in Fig. 3.4 is discretized into $N_{\log} = 60$ pieces such that each point is equally spaced on a logarithmic scale. Here, $\omega^{(s)}$ satisfies the inductive relation $\omega^{(s+1)} = \omega^{(s)} + 2^s \Delta\omega$ with $\omega^{(0)} = 0$, and we use $\Delta\omega t_0 = 8.67\times10^{-18}$ in our analysis. We also note that we do not consider the eigenmodes with

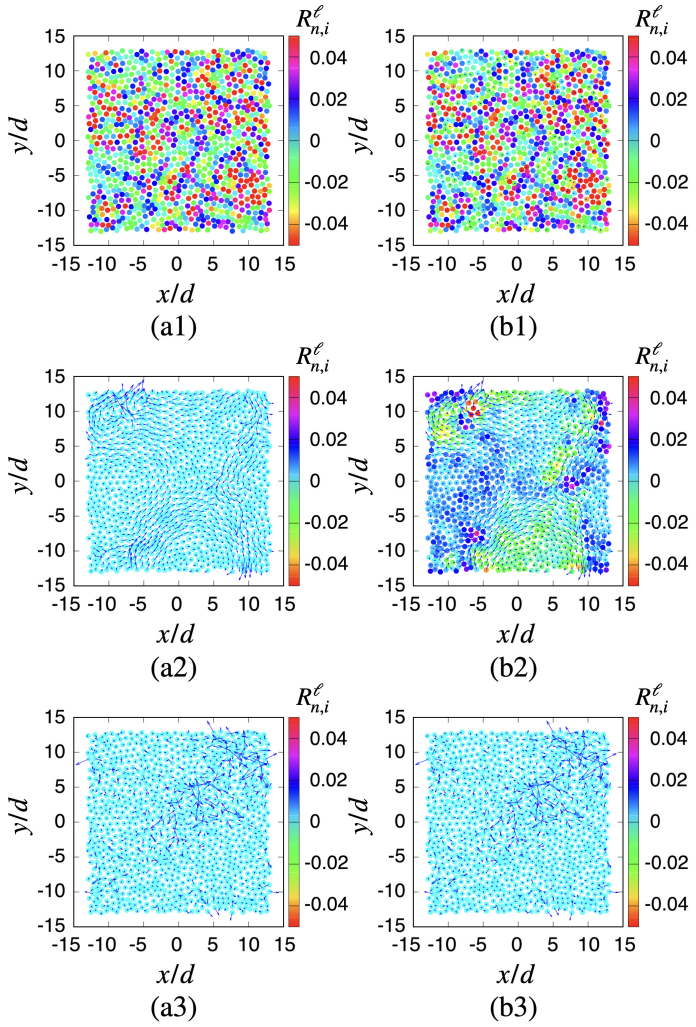

Figure 3.3: Plots of eigenvectors for $\phi = 0.90$ with (a1) $\omega_n t_0 = 1.0 \times 10^{-4}$, (a2) 1.3×10^{-2}, (a3) 1.0, (b1) 1.0×10^{-2}, (b2) 1.3×10^{-2}, and (b3) 1.0, where (a1)-(a3) and (b1)-(b3) are the results for $k_T/k_N = 1.0 \times 10^{-8}$ and 1.0×10^{-4}, respectively. Here, $(R^x_{n,i}, R^y_{n,i})^{\mathrm{T}}$ and $R^{\ell}_{n,i}$ are represented by vectors and colors for the i-th grain, respectively. Note that the magnitudes of the vectors are magnified by 20 times for visualization. These figures are based on numerical results for $N = 1024$.

extremely small eigenvalues in our numerical calculations to ensure the accuracy of our analysis. Such eigenmodes with small eigenvalues are supposed to be the contributions of the rattlers (see details in Appendix D). As shown in Figs. 3.4

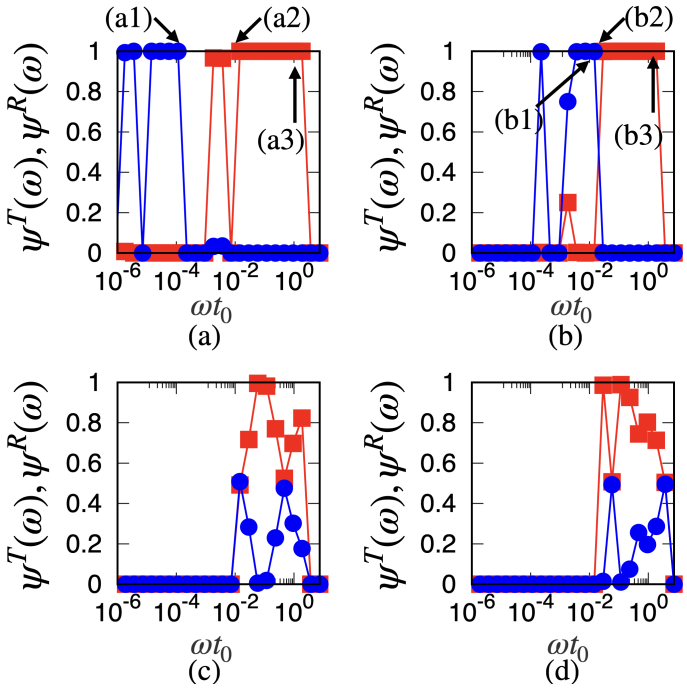

Figure 3.4: Semi-logarithmic plots of ψ^T (red filled squares and lines) and ψ^R (blue filled circles and lines) for $\phi = 0.90$ at (a) $k_T/k_N = 1.0 \times 10^{-8}$, (b) 1.0×10^{-4}, (c) 1.0, and (d) 10.0. The eigenvalues of (a1), (a2), (a3), (b1), (b2), and (b3) in these figures correspond to Figs. 3.3 (a1), (a2), (a3), (b1), (b2) and (b3), respectively. These figures are based on numerical results for $N = 1024$.

(a) and (b), we find the region of $\psi^R \simeq 1$ for low ω and $k_T/k_N < 1.0 \times 10^{-4}$. This region is referred to as Region I. We also find a region that satisfies $\psi^T \simeq 1$ for high ω and $k_T/k_N < 1.0$, in which the translational modes are dominant. This region is referred to as Region II. Here, three characteristic behaviors depend on k_T/k_N at $\phi = 0.90$. First, the translational modes are separable from the rotational modes for $k_T/k_N \leq 1.0 \times 10^{-8}$ because we need a small amount of energy to excite the rotational mode in nearly frictionless situations, as shown in Figs. 3.4 (a) and (b). Second, the translational and rotational contributions are not separated for $1.0 \times 10^{-6} \leq k_T/k_N \leq 1.0 \times 10^{-2}$. Third, the translational and rotational contributions are indistinguishable for $k_T/k_N \geq 1.0$.

The DOS obtained from the Jacobian eigenvalues is shown in Fig. 3.5. Note that we did not consider the eigenmodes with extremely small eigenvalues in our numerical calculations to ensure the accuracy of our analysis.

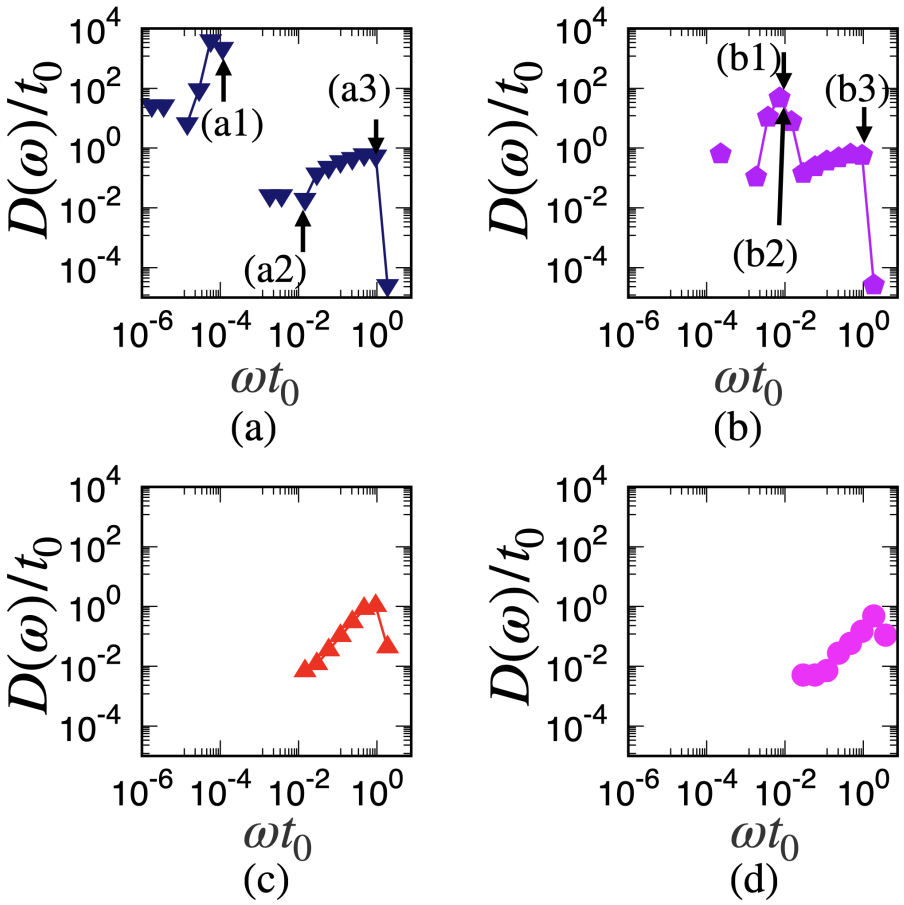

Figure 3.5: Double logarithmic plots of $D(\omega)$ for $\phi = 0.90$ at (a) $k_T/k_N = 1.0 \times 10^{-8}$, (b) 1.0×10^{-4}, (c) 1.0, and (d) 10.0. The eigenvalues of (a1), (a2), (a3), (b1), (b2) and (b3) in these figures correspond to Figs. 3.3 (a1), (a2), (a3), (b1), (b2) and (b3), respectively. These figures are based on numerical results for $N = 1024$.

Based on the results of $\psi^T(\omega)$ and $\psi^R(\omega)$, the DOS is also separated into two regions for $k_T/k_N \leq 1.0 \times 10^{-8}$. The rotational band for low ω shifts to the high ω region as k_T/k_N increases (see Figs. 3.5 (a) and (b)). In Region II with a high ω (see Figs. 3.5 (a) and (b)), the DOS is almost independent of k_T/k_N in which the translational modes are dominant for $k_T/k_N \leq 1.0 \times 10^{-2}$. The distinctions between the two regions for the DOS are visible with a distinct gap between the adjacent regions for $1.0 \times 10^{-10} \leq k_T/k_N \leq 1.0 \times 10^{-8}$. For $1.0 \times 10^{-6} \leq k_T/k_N \leq 1.0 \times 10^{-2}$; however, the high ω region of the DOS in Region I partially overlaps with the low ω region of Region II. Furthermore, Regions I and II are completely merged for $k_T/k_N \geq 1.0$ (see Figs. 3.5 (c) and (d)). Isolated DOS bands for low ω have been observed in systems containing anisotropic grains, such as elliptical grains and dimers [96–98]. However, to the best of our knowledge, there is no study pointing out the existence of isolated bands of DOS in systems consisting of spheres or disks.

Because we have confirmed the existence of a peak of $D(\omega)$ around $\omega t_0 \simeq (k_T/k_N)^{1/2}$, Fig. 3.6 shows the scaling of the DOS in Region I by plotting $\omega_R D(\omega/\omega_R)$, where $\omega_R := \sqrt{k_T/k_N} t_0^{-1}$ [2]. From Fig. 3.6 we find that $\omega_R D(\omega)$

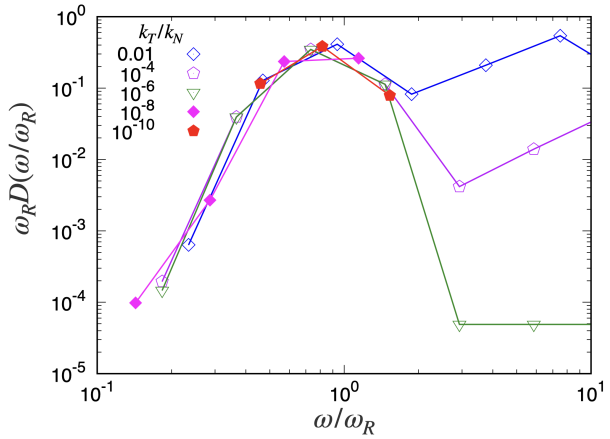

Figure 3.6: Scaling plots of $\omega_R D(\omega)$ versus ω/ω_R for $\phi = 0.90$ and various k_T/k_N in $0.1 < \omega/\omega_R < 10.0$. The figure is based on numerical results for $N = 1024$.

can be expressed as a universal function of ω/ω_R for $0.1 < \omega/\omega_R < 2$ and $k_T/k_N \leq 0.01$.

To investigate the DOS for frictionless grains, we plot the DOS for frictionless systems (see Fig. 3.7) obtained by the Hessian matrix, which is defined in Appendix E. The DOS in Fig. 3.7 shows the absence of an isolated band in the

[2] The reason why $D(\omega)$ is multiplied by ω_R in Fig. 3.6 is as follows. The integral value of the DOS within Region I $\int_{\rm I} d\omega D(\omega)$ is almost independent of k_T/k_N. Then, LHS can be rewritten as a variable $\int_{\rm I} d\omega D(\omega) = \int_{\rm I} d\hat{\omega} D^*(\hat{\omega})$, where $\hat{\omega} := \omega/\omega_R$, $D^*(\hat{\omega}) := \omega_R D(\omega/\omega_R)$ and $\int_{\rm I}$ represents the integral in Region I.

low ω region. Note that the negative slope of $D(\omega)$ at low ω vanishes in Fig. 3.7 if we ignore the contribution of the rattlers (see Appendix D).

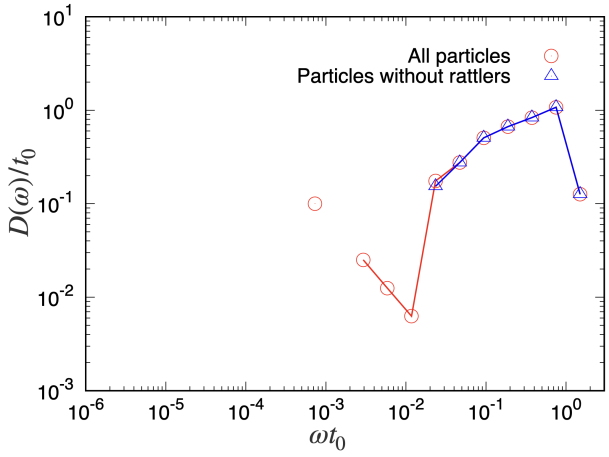

Figure 3.7: Double logarithmic plots of $D(\omega)/t_0$ versus ωt_0 for frictionless grains with $\phi = 0.90$, where red circles are the DOS for all modes, while blue triangles are the DOS with the eliminations of rattlers. The figure is based on numerical results for $N = 1024$.

At the end of this subsection, we examine the usefulness of the effective Hessian $\mathcal{H}$ introduced in Refs. [104–106] by comparing $D(\omega)$ with $D_H(\omega)$, where $D_H(\omega)$ is the DOS obtained from $\mathcal{H}$ (see Appendix E). As shown in Figs. 3.8 (a) and (b), $D(\omega)$ and $D_H(\omega)$ at $k_T/k_N = 1.0 \times 10^{-8}$ and 1.0×10^{-4} are almost identical. Here, the peak of the DOS near $\omega = 0$ is caused by the rotational motion of the grains. The peak of $D(\omega)$ is much higher than that of $D_H(\omega)$ for $k_T = k_N$, as shown in Fig. 3.8 (c). From Fig. 3.8 (d), we confirm that $D(\omega)$ has a sharper peak around $\omega t_0 \approx 2.5$ for $k_T/k_N = 10.0$ than that of $D_H(\omega)$. Therefore, the Jacobian analysis is relevant for a large k_T/k_N.

3.4.2 Theoretical evaluation of G

In this subsection, the validity of the theoretical rigidity expression presented in the previous section is demonstrated. For this purpose, at first, we examine the validity of Eq. (3.40), obtained by the eigenfunction expansion of the nonaffine displacements. Figures 3.9 (a) and (b) illustrate the nonaffine displacements on LHS and RHS of Eq. (3.40), respectively. In Figs. 3.9 (a) and (b), (x, y) and ℓ-components of $d\check{\boldsymbol{q}}_i/d\gamma$ at $\boldsymbol{r}_i$ are represented by vectors and colors, respectively. Figure 3.9 (c) shows the RHS and LHS of Eq. (3.40) against the components of the vectors whose orders follow Eq. (3.35), that is, the local order of the component follows x, y, and ℓ by fixing the particle number, and we align the components from the first grain to the N-th grain without omitting modes with

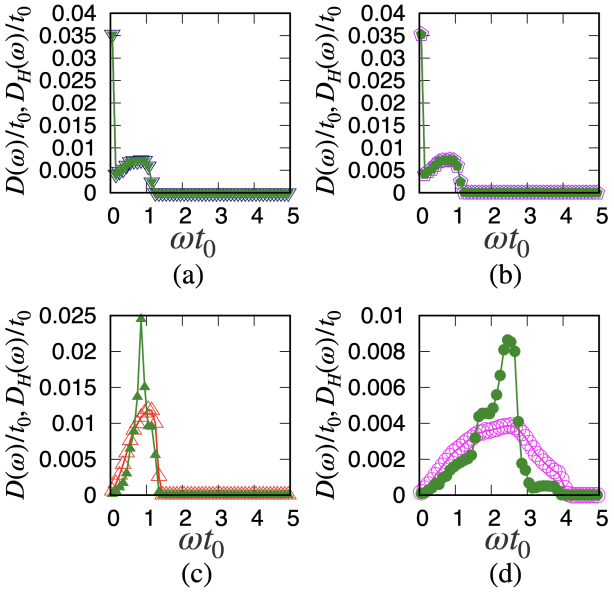

Figure 3.8: Plots of $D(\omega)$ (filled symbols) and $D_H(\omega)$ (open symbols) for $\phi = 0.90$ at (a) $k_T/k_N = 1.0 \times 10^{-8}$, (b) 1.0×10^{-4}, (c) 1.0, and (d) 10.0. These figures are based on numerical results for $N = 1024$.

extremely small and zero eigenvalues. Figure 3.9 shows that the expression in Eq. (3.40) correctly reproduces the simulation results.

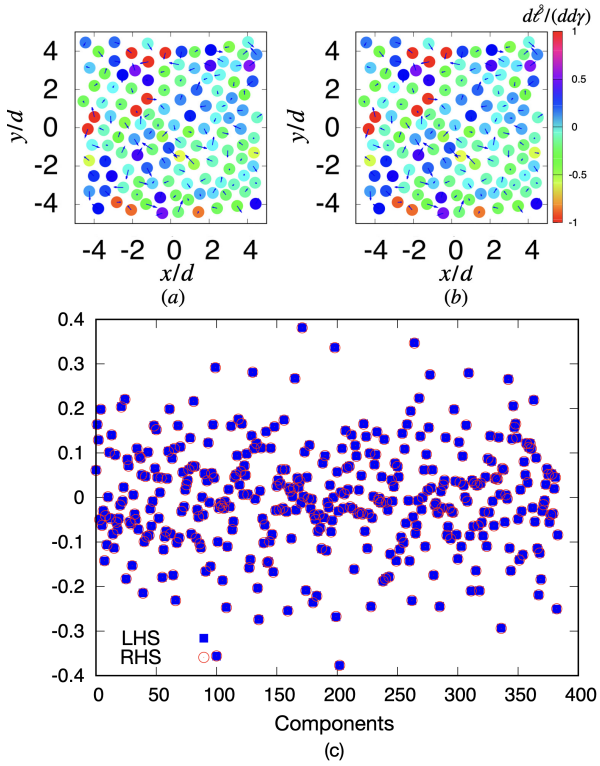

Figure 3.9: Plots of nonaffine displacements in (a) RHS and (b) LHS of Eq. (3.40). The vector and color of each grain correspond to x, y, and ℓ-components of the eigenvector of the grain, respectively. Here, the magnitude of the vectors is magnified by 5 times for visualization. (c) Plots of the RHS (open symbols) and LHS (filled symbols) of Eq. (3.40) for each component whose order follows Eq. (3.35). These figures are based on numerical results for $N = 128$.

The dimensionless rigidity obtained from Eqs. (3.41),(3.42) and (3.46) with the aid of $G^* := k_N d^{1/2}$ is shown in Fig. 3.10. This indicates the quantitative agreement between the theoretical and numerical values. Therefore, the rigidity in the linear response regime can be determined completely using the Jacobian analysis. On the contrary to the previous studies [12, 21, 142], we should note that G is not proportional to $\phi - \phi_c$ for a large k_T/k_N, where ϕ_c is the critical fraction of jamming transition for frictional grains.

The rigidity G is independent of k_T/k_N for $k_T/k_N \leq 1.0 \times 10^{-4}$ (see Fig. 3.11). We have confirmed that G smoothly approaches the frictionless value in the limit $k_T \to 0$ in contrary to Refs. [71, 72]. Here, G cannot be expressed as

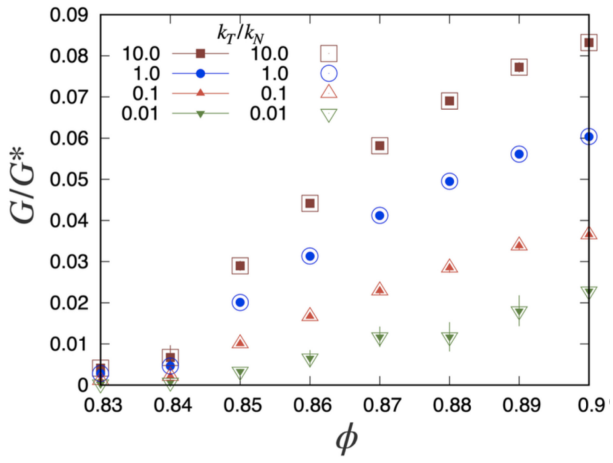

Figure 3.10: Plots of theoretical (Eq. (3.41): open symbols) and numerical (Eq. (3.18): filled symbols) G against ϕ for various k_T/k_N. The figure obtained by the numerical results for $N = 128$.

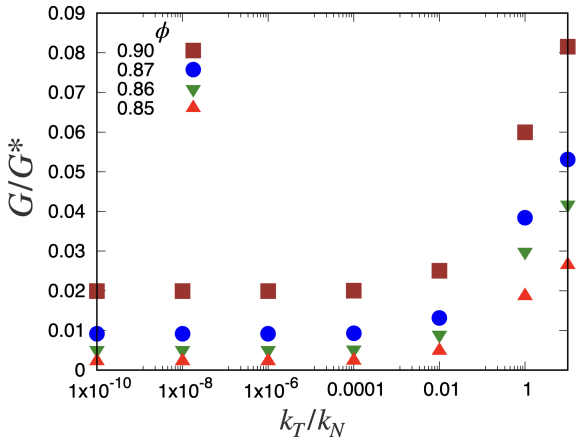

Figure 3.11: Plots of numerical G against k_T/k_N for various ϕ. The figure is obtained by the numerical results for $N = 1024$.

a factorization for large k_T/k_N [3].

To clarify the contributions of nonaffine deformations to the rigidity, we plot $G_{\rm NA}$ defined in Eq. (3.43) against ϕ in Fig. 3.12, in which $G_{\rm NA}$ becomes large as ϕ increases. Remarkably, $G_{\rm NA}$ is positive for $k_T/k_N > 2.0$, $G_{\rm NA} \approx 0$ at $k_T/k_N = 2.0$, and $G_{\rm NA}$ is negative for $k_T/k_N < 2.0$. The positive $G_{\rm NA}$ for a large k_T/k_N is counterintuitive, in which G increases from $G_{\rm A}$ even when the system is relaxed to the FB state. In the future, we must clarify the origin of this counterintuitive $G_{\rm NA}$. We note that the negative $G_{\rm NA}$ for a small k_T/k_N can be understood by the relaxation process to look for a FB configuration after applying affine deformations to the system.

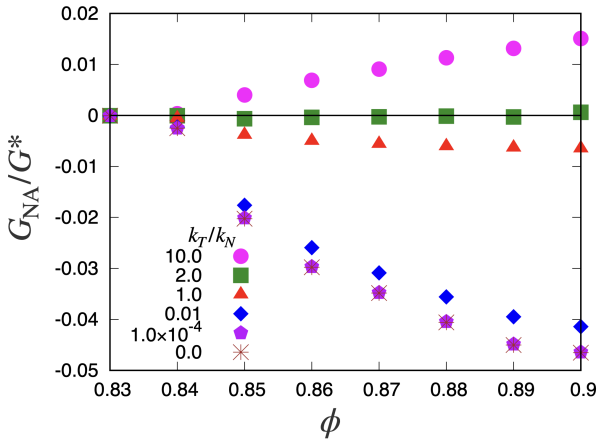

Figure 3.12: Plots of $G_{\rm NA}$ against ϕ for various k_T/k_N. The figure is obtained by the numerical results for $N = 1024$.

Because $G_{\rm NA}$ is proportional to the inverse of the eigenvalues from Eq. (3.46), the contributions of the small eigenvalues are expected to be important for the nonaffine displacements. In addition, it is possible to distinguish the contribution of Region I from that of Region II for a sufficiently small k_T/k_N by the apparent energy gap between the two regions. Here, we have divided Regions I and II by $\omega_c t_0 = 1.0 \times 10^{-2}$ whose value splits Regions I and II for $\phi = 0.90$ and $k_T/k_N = 1.0 \times 10^{-8}$ (see Fig. 3.5 (a)). Then, $g_{\rm NA}^{\rm I}$ and $g_{\rm NA}^{\rm II}$ are the one-sample rigidities corresponding to the contributions from the nonaffine

[3] We have confirmed that the factorization $G(\phi, k_T/k_N) = G_0(\phi)\mathcal{G}(k_T/k_N)$ is not held, where $G_0(\phi)$ is the rigidity of frictionless system.

displacements obtained from Regions I and II, respectively, as follows:

$$g_{\rm NA}^{\rm I} = -\frac{1}{L^2}\sum_{n(\tilde{\lambda}_n<\omega_c^2)}{}' \frac{\langle \tilde{L}_n|\Xi\rangle\,\langle\Theta|\tilde{R}_n\rangle}{\tilde{\lambda}_n}, \tag{3.55}$$

$$g_{\rm NA}^{\rm II} = -\frac{1}{L^2}\sum_{n(\tilde{\lambda}_n\geq\omega_c^2)}{}' \frac{\langle \tilde{L}_n|\Xi\rangle\,\langle\Theta|\tilde{R}_n\rangle}{\tilde{\lambda}_n}. \tag{3.56}$$

We plot $g_{\rm NA}^{\rm I}$, $g_{\rm NA}^{\rm II}$, and $g_{\rm NA}$ for each sample in Fig. 3.13, where $g_{\rm NA}$ is defined as

$$g_{\rm NA} := \frac{1}{2L^2}\sum_{i,j(i\neq j)}\left[\sum_{\zeta=x,y} r_{ij}^{y}\tilde{\mathcal{J}}_{ij}^{x\zeta}\frac{d\mathring{r}_{ij}^{\zeta}}{d\gamma} - r_{ij}^{y}\tilde{\mathcal{J}}_{ij}^{x\ell}\frac{d\mathring{\ell}_{ij}}{d\gamma}\right]. \tag{3.57}$$

Contrary to our expectations, the contributions to $g_{\rm NA}^{\rm I}$ are almost zero. Consequently, $G_{\rm NA}$ obtained from the eigenmode expansion of Region II is almost identical to $G_{\rm NA}$. Recalling that Region I is dominated by the rotation of grains, it is safe to assert that the rigidity of amorphous solids is determined only by translational modes, at least for $k_T/k_N = 1.0\times10^{-8}$.

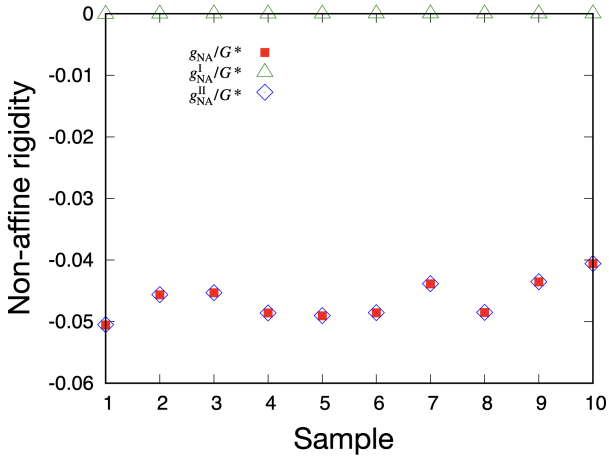

Figure 3.13: Plots of $g_{\rm NA}^{\rm I}, g_{\rm NA}^{\rm II}$, and $g_{\rm NA}$ obtained by Eqs. (3.55)–(3.57) at $\phi = 0.90$ and $k_T/k_N = 1.0\times10^{-8}$ against samples for different configuration. The figure is obtained by the numerical results for $N = 1024$.

3.5 Concluding Remarks of this Chapter

We analyzed the eigenmodes of the Jacobian and obtained an expression for the rigidity of amorphous solids of frictional grains under an infinitesimal strain. The rigidity obtained by the Jacobian completely agreed with that obtained

from the simulation. We confirmed that the rigidity was determined by the translational modes.

Further, we confirmed that the DOS can be divided into two regions. In the low-frequency region (Region I), the rotation of the grains plays a dominant role. These modes are characterized by the frequency $(k_T/k_N)^{1/2}/t_0$. Region I merges into the high-frequency region (Region II) for large k_T/k_N, where Region II is dominated by translational modes.

Although previous studies adopted the Hessian method by introducing an effective potential for frictional grains [104–106], we adopted the Jacobian for eigenvalue analysis. For a sufficiently small k_T/k_N, the DOS obtained from the theoretical analysis by the Jacobian is similar to that obtained by the Hessian analysis. However, the difference between the DOS obtained using the Jacobian and that obtained using the Hessian is visible for $k_T \geq k_N$. Therefore, our theoretical analysis is significant for large k_T/k_N.

When we consider the effect of the dynamical friction, that is, slips between grains, the rigidity is discontinuously changed in the frictionless limit [71, 72]. However, the rigidity continuously changes with k_T/k_N in our system and is smoothly connected to that of frictionless systems ($k_T = 0$). Because our system can be regarded as having infinitely large static and dynamical frictional constants, there is no slip between the grains. Therefore, it might be natural for G to continuously change the limit for $k_T/k_N \to 0$ in our system. In future work, we will consider the effects of slips, which are important for real frictional grains.

We reproduced the rigidity in the linear response regime using the eigenvalues and eigenfunctions of the Jacobian with modifications in the rotational part. However, the applicability of this theory is limited. The method used in this study cannot be used for finite strains because it is obvious that the eigenvectors are not orthogonal in the sheared state. Moreover, there are plastic deformations of the grains under large strains, which were not considered in this study. Therefore, we cannot predict the correct value of the theoretical rigidity at the stress drop point. More importantly, the effect of the history dependence of the frictional force is significant even in the linear response regime, although we have ignored such contacts because of the difficulty in constructing a proper theory. This issue should be addressed in future studies. Note that Chapter 4 gives a partial answer to the question of whether the eigenvalue analysis can be used even if stress avalanches exist in finite strain, though we ignore the effects of slip processes.

Chapter 4

Eigenvalue analysis of amorphous solids consisting of frictional particles for finite shear strain

4.1 Introduction of Chapter 4

Amorphous materials consisting of dispersed repulsive grains, such as powders, colloids, bubbles, and emulsions, behave as fragile solids above jamming density [2, 5, 8–10]. When we consider a response of such materials to an applied strain γ, the rigidity G is independent of the strain in the linear response regime, whereas it exhibits softening in the nonlinear regime [67–70, 134–139]. Above the yielding points, there are some plastic events, such as stress avalanches in the collection of grains.

The Hessian matrix determined by the configuration of grains is commonly used for amorphous solids consisting of frictionless grains [5, 8, 17, 82, 84, 87–89]. To determine the rigidity, eigenvalue analysis of the Hessian matrix [83, 86, 90, 107–109], is commonly used, although the quantitative accuracy of the theoretical rigidity has not been verified to the best of our knowledge. Some studies have suggested that the decrement of the non-zero smallest eigenvalue of the Hessian matrix with the strain is a precursor of an avalanche or stress drop near a critical strain γ_c [107,108,111–113]. Correspondingly, some studies indicated that the rigidity G and the stress σ should behave as $G - G_{\rm reg} \propto -1/\sqrt{\gamma_c - \gamma}$ and $\sigma - \sigma_{\rm reg} \propto \sqrt{\gamma_c - \gamma}$ near γ_c, where $G_{\rm reg}$ and $\sigma_{\rm reg}$ are the regular parts of the rigidity and stress conversing to constants at γ_c, respectively [107, 108, 110, 114].

In general, the frictional force between the grains cannot be ignored in physical situations. Because the frictional force generally depends on the contact

history, Hessian analysis is not applicable to such systems. Thus, Chattoraj et al. adopted the Jacobian matrix instead of the Hessian matrix to discuss the stability of the configuration of frictional grains under strain [115]. They performed eigenvalue analysis under athermal quasi-static shear processes and determined the existence of oscillatory instability originating from inter-particle friction at a certain strain [115–117]. Moreover, some studies have performed an analysis of the Hessian matrix with the aid of an effective potential for frictional grains [104, 105]. Recently, Liu et al. suggested that Hessian matrix analysis with another effective potential can be used, even if slip processes exist [106]. Previous studies [104,105] have reported that the friction between grains causes a continuous change in the functional form of the density of states (DOS), which differs from that of frictionless systems. So far, there have been few theoretical studies to determine the rigidity of the frictional grains.

In our previous study [119] corresponding to Chapter 3, we developed an analysis of the Jacobian matrix to determine the rigidity of two-dimensional amorphous solids consisting of frictional grains interacting with the Hertzian force in the linear response to an infinitesimal strain. In the study, we ignore the dynamic friction caused by the slip processes of contact points. We found that there are two modes in the DOS for a sufficiently small tangential-to-normal stiffness ratio. Rotational modes exist in the region of low-frequency or small eigenvalues, whereas translational modes exist in the region of high-frequency or large eigenvalues. The rigidity determined by the translational modes is in good agreement with that obtained by the molecular dynamics simulations, whereas the contribution of the rotational modes is almost zero. Nevertheless, there are several shortcomings in the previous analysis. (i) The analysis can be used only in the linear response regime, where the base state is not influenced by the applied strain. (ii) As a result, we cannot discuss the behavior of plastic deformations or avalanches of grains. (iii) Even if we restrict our interest to the linear response regime, we cannot include the effect of tangential contact for the preparation of the initial configuration. (iv) We also ignored the effect of dynamical slip between the contacted grains [119].

The purpose of this study is to overcome the shortcomings of our previous study except for point (iv) [119]. Thus, we analyze a collection of two-dimensional grains interacting with repulsive harmonic potentials within the contact radius, without considering the dynamical slip between the grains. Owing to the special properties of the harmonic potential, the eigenvalue analysis of the Jacobian matrix becomes equivalent to that of the Hessian matrix. Subsequently, using the eigenvalue analysis of the Hessian matrix, we demonstrate that the theoretical rigidity under a large strain agrees with that obtained by the simulation.

The remainder of this chapter is organized as follows. In Sec. 4.2, we introduce the model to be analyzed in this study. In Sec. 4.3, we summarize the theoretical framework for determining the rigidity of an amorphous solid consisting of frictional grains without considering the dynamical slip process. In Sec. 4.4, we present the results of the stress-strain relation obtained using the theory formulated in Sec. 4.3. We also compare the theoretical results with

the simulation results to demonstrate the relevancy of our theoretical analysis. In Sec. 4.5, we summarize the obtained results and address future tasks to be solved. In Appendix F, we numerically demonstrate the absence of history-dependent tangential deformations in our system. In Appendix G, we explain the detailed behavior of the eigenvalue near the stress-drop points. In Appendix H, we present some detailed properties of the Hessian matrix in a harmonic system. In Appendix I, we present some properties of the Jacobian matrix in a harmonic system and demonstrate its equivalency to the Hessian matrix. Appendix J presents the detailed properties of rigidity.

4.2 Model used in this Chapter

Our system contains N frictional circular disks embedded in a two-dimensional space. To prevent the system from crystallization, it contains an equal number of grains with diameters d and $d/1.4$ [78]. We assume that the mass of grain i is proportional to d_i^2, where d_i is the diameter of i-th grain. For later convenience, we introduce m as the mass of grain having a diameter d. In this study, x_i, y_i, and θ_i denote x and y components of the position of i-th grain, and the rotational angle of the i-th grain, respectively. We introduce the generalized coordinates of the i-th grain as follow:

$$\boldsymbol{q}_i := (\boldsymbol{r}_i^{\mathrm{T}}, \ell_i)^{\mathrm{T}} := (x_i, y_i, d_i\theta_i/2)^{\mathrm{T}}, \tag{4.1}$$

where the superscript T denotes the transposition.

Let the force, and z-component of the torque acting on the i-th grain be $\boldsymbol{F}_i := (F_i^x, F_i^y)^{\mathrm{T}}$ and T_i, respectively. Then, the equations of motion of i-th grain are expressed as

$$m_i \frac{d^2\boldsymbol{r}_i}{dt^2} = \boldsymbol{F}_i, \tag{4.2}$$

$$I_i \frac{d^2\theta_i}{dt^2} = T_i, \tag{4.3}$$

with mass m_i and momentum of inertia $I_i := m_i d_i^2/8$ of i-th grain. In a system without volume forces, such as gravity, we can write

$$\boldsymbol{F}_i = \sum_{j\neq i} \boldsymbol{f}_{ij} - m_i\eta_D\dot{\boldsymbol{r}}_i, \tag{4.4}$$

$$T_i = \sum_{j\neq i} T_{ij} - I_i\eta_D\dot{\theta}_i, \tag{4.5}$$

where we have adopted the notation $\dot{A} := dA/dt$ for arbitrary variable A such as $A = \boldsymbol{r}_i$ and θ_i. $\boldsymbol{f}_{ij}$ and T_{ij} are the force and z-component of the torque acting on the i-th grain from the j-th grain, respectively. Here, as a simplified description of the drag terms from the background fluid, η_D is a damping constant uniformly

acting on grains, and T_{ij} is given by

$$T_{ij} = -\frac{d_i}{2}(n_{ij}^x f_{ij}^y - n_{ij}^y f_{ij}^x), \tag{4.6}$$

where we have introduced the normal unit vector between i-th and j-th grains as $\boldsymbol{n}_{ij} := \boldsymbol{r}_{ij}/|\boldsymbol{r}_{ij}| := (\boldsymbol{r}_i - \boldsymbol{r}_j)/|\boldsymbol{r}_i - \boldsymbol{r}_j|$. The force $\boldsymbol{f}_{ij}$ can be divided into normal $\boldsymbol{f}_{N,ij}$ and tangential $\boldsymbol{f}_{T,ij}$ parts as

$$\boldsymbol{f}_{ij} = (\boldsymbol{f}_{N,ij} + \boldsymbol{f}_{T,ij})H(d_{ij}/2 - |\boldsymbol{r}_{ij}|), \tag{4.7}$$

where $d_{ij} := d_i + d_j$ and $H(x)$ is Heaviside's step function, taking $H(x) = 1$ for $x > 0$, and $H(x) = 0$ otherwise. We assume that the contact force is expressed as

$$\boldsymbol{f}_{N,ij} := k_N \xi_{N,ij} \boldsymbol{n}_{ij}, \tag{4.8}$$

$$\boldsymbol{f}_{T,ij} := k_T \xi_{T,ij} \boldsymbol{t}_{ij}, \tag{4.9}$$

where k_N and k_T are the stiffness parameters of normal and tangential contacts, respectively. The contact force can be derived from the harmonic potential. In Eqs. (4.8) and (4.9) we have introduced $\xi_{N,ij} := d_{ij}/2 - |\boldsymbol{r}_{ij}|$ and

$$\begin{aligned}\boldsymbol{\xi}_{T,ij}(t) := & \int_{C_{ij}(t')} dt' \boldsymbol{v}_{T,ij}(t') \\ & - \left[\left(\int_{C_{ij}(t')} dt' \boldsymbol{v}_{T,ij}(t') \right) \cdot \boldsymbol{n}_{ij}(t) \right] \boldsymbol{n}_{ij}(t),\end{aligned} \tag{4.10}$$

where we have used $\boldsymbol{v}_{T,ij} := \dot{\boldsymbol{r}}_{ij} - \dot{\boldsymbol{\xi}}_{N,ij} + \boldsymbol{u}_{ij}(d_i\dot{\theta}_i + d_j\dot{\theta}_j)/2$ with $\boldsymbol{u}_{ij} := (n_{ij}^y, -n_{ij}^x)^{\mathrm{T}}$, $\boldsymbol{t}_{ij} := -\boldsymbol{\xi}_{T,ij}/|\xi_{T,ij}|$, $\xi_{T,ij} := |\boldsymbol{\xi}_{T,ij}|$, and the integration over the duration time of contact between i-th and j-th grains $\int_{C_{ij}(t')} dt'$ with the trajectory $C_{ij}(t')$ of the contact point between i-th and j-th grains at t'. As shown in Appendix F, we have confirmed that the second term on the right-hand side (RHS) of Eq. (4.10) is zero for harmonic systems, although we do not have any mathematical proof for this statement thus far. For simplicity, we consider neither the effects of the dynamical slip processes in the tangential equation of motion nor the dissipative contact force.

We impose the Lees-Edwards boundary conditions [140, 141], where the direction parallel to the shear strain is the x-direction. After generating a stable grain configuration starting from a random configuration by using Eqs. (4.2)–(4.10) without strain, we apply a step strain $\Delta\gamma$ to all grains, where x-coordinate of the position of the i-th grain is shifted by an affine displacement $\Delta x_i(\Delta\gamma) := \Delta\gamma y_i^{\mathrm{FB}}(0)$. Here, the superscript FB denotes the force-balance (FB) state at which $\boldsymbol{F}_i = \boldsymbol{0}$ and $T_i = 0$ for arbitrary i. As shown in Sec. 4.3.1, the FB state is equivalent to the potential minimum for harmonic grains. Subsequently, the system is relaxed to an FB state. We further apply the step strain $\Delta\gamma$ associated with the subsequent relaxation process again to obtain the state at $2\Delta\gamma$. By repeating this process, we can reach a deformed state with the strain γ.

The plastic deformations for a large γ depend on the choice of $\Delta\gamma$ [89]. Moreover, the theoretical formulation assumes $\Delta\gamma \to 0$. Therefore, we adopt the backtracking method [143, 144]. If a plastic event is encountered under a fixed $\Delta\gamma_{\rm in}$, the system is restored to its original state without a plastic event. Subsequently, we apply a new strain, $0.1\Delta\gamma_{\rm in}$, to the system. Even if we encounter a plastic event with $0.1\Delta\gamma_{\rm in}$, we further examine the smaller step strain of $0.01\Delta\gamma_{\rm in}$. We repeat this procedure until we reach $\Delta\gamma < \Delta\gamma_{\rm Th}$ (see Appendix G).

We introduce the rate of nonaffine displacements for $r_i^{{\rm FB},\zeta}(\gamma)$ with $\zeta = x$ or y and $\ell_i^{\rm FB}(\gamma)$ as:

$$\frac{d\mathring{r}_i^{\zeta}(\gamma)}{d\gamma} := \lim_{\Delta\gamma\to 0} \frac{r_i^{{\rm FB},\zeta}(\gamma+\Delta\gamma) - r_i^{{\rm FB},\zeta}(\gamma)}{\Delta\gamma} - \delta_{\zeta x} y_i^{\rm FB}(\gamma), \tag{4.11}$$

$$\frac{d\mathring{\ell}_i(\gamma)}{d\gamma} := \lim_{\Delta\gamma\to 0} \frac{\ell_i^{\rm FB}(\gamma+\Delta\gamma) - \ell_i^{\rm FB}(\gamma)}{\Delta\gamma}. \tag{4.12}$$

Our system is characterized by the generalized coordinate

$$\boldsymbol{q}(\gamma) := (\boldsymbol{q}_1^{\rm T}(\gamma), \boldsymbol{q}_2^{\rm T}(\gamma), \cdots, \boldsymbol{q}_N^{\rm T}(\gamma))^{\rm T}. \tag{4.13}$$

The configuration in the FB state at strain γ is denoted by

$$\boldsymbol{q}^{\rm FB}(\gamma) := ((\boldsymbol{q}_1^{\rm FB}(\gamma))^{\rm T}, (\boldsymbol{q}_2^{\rm FB}(\gamma))^{\rm T}, \cdots, (\boldsymbol{q}_N^{\rm FB}(\gamma))^{\rm T})^{\rm T}. \tag{4.14}$$

The shear stress $\sigma(\gamma)$ at $\boldsymbol{q}^{\rm FB}(\gamma)$ for one sample is given by:

$$\begin{aligned}\sigma(\boldsymbol{q}^{\rm FB}(\gamma)) = -\frac{1}{2L^2}\sum_i\sum_{j>i}\big[&f_{ij}^x(\boldsymbol{q}^{\rm FB}(\gamma))r_{ij}^y(\boldsymbol{q}^{\rm FB}(\gamma)) \\ &+ f_{ij}^y(\boldsymbol{q}^{\rm FB}(\gamma))r_{ij}^x(\boldsymbol{q}^{\rm FB}(\gamma))\big].\end{aligned} \tag{4.15}$$

The rigidity g for one sample is defined as

$$g := \left.\frac{d\sigma(\boldsymbol{q}(\gamma))}{d\gamma}\right|_{\boldsymbol{q}(\gamma)=\boldsymbol{q}^{\rm FB}(\gamma)}, \tag{4.16}$$

where the differentiation on the RHS of Eq. (4.16) is defined as follows:

$$\begin{aligned}&\left.\frac{d\sigma(\boldsymbol{q}(\gamma))}{d\gamma}\right|_{\boldsymbol{q}(\gamma)=\boldsymbol{q}^{\rm FB}(\gamma)} \\ &\quad := \lim_{\Delta\gamma\to 0}\frac{\sigma(\boldsymbol{q}^{\rm FB}(\gamma+\Delta\gamma)) - \sigma(\boldsymbol{q}^{\rm FB}(\gamma))}{\Delta\gamma}.\end{aligned} \tag{4.17}$$

In the numerical calculation, we use a non-zero but sufficiently small $\Delta\gamma$ for the evaluation of g. Then, the averaged rigidity G is defined as

$$G := \langle g \rangle, \tag{4.18}$$

where $\langle\cdot\rangle$ is the ensemble average.

4.3 Theoretical Analysis

In this section, we introduce Hessian matrix in Sec. 4.3.1 and theoretical expressions of rigidity in Sec. 4.3.2.

4.3.1 Hessian matrix for frictional grains

Because the Hessian matrix is equivalent to the Jacobian matrix for harmonic grains, as shown in Appendices H.1 and I.3, in this study, we adopt the Hessian matrix ($\mathcal{H}$), where the element is given by [132]:

$$\mathcal{H}_{ij}^{\alpha\beta} := \left.\frac{\partial^2 \delta e_{ij}(\boldsymbol{q}(\gamma))}{\partial q_i^\alpha \partial q_j^\beta}\right|_{\boldsymbol{q}(\gamma)=\boldsymbol{q}^{\mathrm{FB}}(\gamma)}, \tag{4.19}$$

where α and β are any of x, y and ℓ, while i and j express the grain indices. Here, we have introduced the effective potential energy δe_{ij} between the contacted i-th and j-th grains as:

$$\delta e_{ij} := \frac{k_N}{2}(\delta \boldsymbol{r}_{ij} \cdot \boldsymbol{n}_{ij})^2 + \frac{k_T}{2}\delta \boldsymbol{r}_{ij,\perp}^2, \tag{4.20}$$

where $\delta \boldsymbol{r}_{ij,\perp}$ is defined as

$$\delta \boldsymbol{r}_{ij,\perp} := \delta \boldsymbol{r}_{ij} - (\delta \boldsymbol{r}_{ij} \cdot \boldsymbol{n}_{ij})\boldsymbol{n}_{ij} - \delta \boldsymbol{\ell}_{ij} \times \boldsymbol{n}_{ij} \tag{4.21}$$

with

$$\delta \boldsymbol{r}_{ij} := \delta \boldsymbol{r}_i - \delta \boldsymbol{r}_j, \tag{4.22}$$

$$\delta \boldsymbol{\ell}_{ij} := (\delta \ell_i + \delta \ell_j)\boldsymbol{e}_z \tag{4.23}$$

under the virtual displacements $\delta \boldsymbol{r}_i$ and $\delta \ell_i$ from the FB state at $\boldsymbol{r}_i^{\mathrm{FB}}$ and ℓ_i^{FB}, respectively.

The Hessian matrix introduced in Eq. (4.19) can be written as

$$\mathcal{H} = \begin{bmatrix} \mathcal{H}_{11} & \cdots & \mathcal{H}_{1i} & \cdots & \mathcal{H}_{1j} & \cdots & \mathcal{H}_{1N} \\ \vdots & \ddots & \vdots & & \vdots & & \vdots \\ \mathcal{H}_{i1} & \cdots & \mathcal{H}_{ii} & \cdots & \mathcal{H}_{ij} & \cdots & \mathcal{H}_{iN} \\ \vdots & & \vdots & \ddots & \vdots & & \vdots \\ \mathcal{H}_{j1} & \cdots & \mathcal{H}_{ji} & \cdots & \mathcal{H}_{jj} & \cdots & \mathcal{H}_{jN} \\ \vdots & & \vdots & & \vdots & \ddots & \vdots \\ \mathcal{H}_{N1} & \cdots & \mathcal{H}_{Ni} & \cdots & \mathcal{H}_{Nj} & \cdots & \mathcal{H}_{NN} \end{bmatrix}, \tag{4.24}$$

where $\mathcal{H}_{ij}$ is a 3×3 submatrix of the Hessian $\mathcal{H}$ for a pair of grains i and j satisfying:

$$\mathcal{H}_{ij} = \begin{bmatrix} \mathcal{H}_{ij}^{xx} & \mathcal{H}_{ij}^{xy} & \mathcal{H}_{ij}^{x\ell} \\ \mathcal{H}_{ij}^{yx} & \mathcal{H}_{ij}^{yy} & \mathcal{H}_{ij}^{y\ell} \\ \mathcal{H}_{ij}^{\ell x} & \mathcal{H}_{ij}^{\ell y} & \mathcal{H}_{ij}^{\ell\ell} \end{bmatrix}. \tag{4.25}$$

See Appendix H.1 for an explicit expression of each component of the Hessian matrix. Note that $\mathcal{H}_{ij}^{\alpha\beta} = 0$ if the i-th and j-th grains are not in contact with each other.

Because $\mathcal{H}$ is a real symmetric matrix, its eigenvalues and eigenvectors are also real. Using the decomposition of the potential, the Hessian matrix can be divided into

$$\mathcal{H}_{ij}^{\alpha\beta} = \mathcal{H}_{N,ij}^{\alpha\beta} + \mathcal{H}_{T,ij}^{\alpha\beta}, \tag{4.26}$$

where

$$\mathcal{H}_{N,ij}^{\alpha\beta} := \left.\frac{\partial^2 \delta e_{N,ij}^{\alpha}(\boldsymbol{q}(\gamma))}{\partial q_i^{\alpha} \partial q_j^{\beta}}\right|_{\boldsymbol{q}(\gamma)=\boldsymbol{q}^{\mathrm{FB}}(\gamma)}, \tag{4.27}$$

$$\mathcal{H}_{T,ij}^{\alpha\beta} := \left.\frac{\partial^2 \delta e_{T,ij}^{\alpha}(\boldsymbol{q}(\gamma))}{\partial q_i^{\alpha} \partial q_j^{\beta}}\right|_{\boldsymbol{q}(\gamma)=\boldsymbol{q}^{\mathrm{FB}}(\gamma)} \tag{4.28}$$

for $i \neq j$ and

$$\mathcal{H}_{N,ij}^{\alpha\beta} := \left.\frac{\partial^2 \delta e_{N,ik}^{\alpha}(\boldsymbol{q}(\gamma))}{\partial q_i^{\alpha} \partial q_i^{\beta}}\right|_{\boldsymbol{q}(\gamma)=\boldsymbol{q}^{\mathrm{FB}}(\gamma)}, \tag{4.29}$$

$$\mathcal{H}_{T,ij}^{\alpha\beta} := \left.\frac{\partial^2 \delta e_{T,ik}^{\alpha}(\boldsymbol{q}(\gamma))}{\partial q_i^{\alpha} \partial q_i^{\beta}}\right|_{\boldsymbol{q}(\gamma)=\boldsymbol{q}^{\mathrm{FB}}(\gamma)} \tag{4.30}$$

for $i = j$. Here, we have introduced

$$\delta e_{N,ij} := \frac{k_N}{2}(\delta \boldsymbol{r}_{ij} \cdot \boldsymbol{n}_{ij})^2, \tag{4.31}$$

$$\delta e_{T,ij} := \frac{k_T}{2} \delta \boldsymbol{r}_{ij,\perp}^2. \tag{4.32}$$

To determine the explicit expression of each component of the Hessian matrix, refer to Appendix H.1.

The eigenequation of the Hessian matrix $\mathcal{H}$ is given by

$$\mathcal{H} \left|\Phi_n\right\rangle = \lambda_n \left|\Phi_n\right\rangle, \tag{4.33}$$

where $|\Phi_n\rangle$ is the right eigenvector corresponding to the n-th eigenvalue λ_n of $\mathcal{H}$. Because the Hessian matrix is a real symmetric matrix, its left eigenequation is equivalent to its right eigenequation. Such properties remain unchanged even under the Lees-Edwards boundary conditions (see Appendix H.2). If all eigenstates are non-degenerate, $|\Phi_n\rangle$ satisfies the orthonormal relation $\langle\Phi_m|\Phi_n\rangle = \delta_{mn}$ with normalization $\langle\Phi_n|\Phi_n\rangle = 1$, where $\langle\Phi_n|\Phi_n\rangle := \sum_{i=1}^{N} \sum_{\alpha=x,y,\ell} (\Phi_{n,i}^{\alpha})^2$.

4.3.2 Expressions of the rigidity via eigenmodes

In this subsection, we consider the rigidity g introduced in Eq. (4.18). See Appendix J for the detailed properties of g.

Let us introduce $\tilde{\boldsymbol{F}}_i := (\tilde{F}_i^x, \tilde{F}_i^y, \tilde{F}_i^\ell)^{\mathrm{T}} := (F_i^x, F_i^y, 2T_i/d_i)^{\mathrm{T}}$ and $|\tilde{F}(\boldsymbol{q}(\gamma))\rangle$ as

$$|\tilde{F}(\boldsymbol{q}(\gamma))\rangle := [\tilde{\boldsymbol{F}}_1^{\mathrm{T}}(\boldsymbol{q}(\gamma)), \tilde{\boldsymbol{F}}_2^{\mathrm{T}}(\boldsymbol{q}(\gamma)), \cdots, \tilde{\boldsymbol{F}}_N^{\mathrm{T}}(\boldsymbol{q}(\gamma))]^{\mathrm{T}}. \tag{4.34}$$

Because the FB state is the minimum state of the potential energy, as shown in Appendix H.1, $|\tilde{F}(\boldsymbol{q}(\gamma))\rangle|_{\boldsymbol{q}(\gamma)=\boldsymbol{q}^{\mathrm{FB}}(\gamma)}$ satisfies

$$|\tilde{F}(\boldsymbol{q}(\gamma))\rangle\Big|_{\boldsymbol{q}(\gamma)=\boldsymbol{q}^{\mathrm{FB}}(\gamma)} = \frac{d\,|\tilde{F}(\boldsymbol{q}(\gamma))\rangle}{d\gamma}\Big|_{\boldsymbol{q}(\gamma)=\boldsymbol{q}^{\mathrm{FB}}(\gamma)} = |0\rangle\,, \tag{4.35}$$

where $|0\rangle$ is the ket vector containing 0 for all components.

Introducing

$$\left|\frac{d\mathring{q}}{d\gamma}\right\rangle := \left[\frac{d\mathring{r}_1^x}{d\gamma}, \frac{d\mathring{r}_1^y}{d\gamma}, \frac{d\mathring{\ell}_1}{d\gamma}, \cdots, \frac{d\mathring{r}_N^x}{d\gamma}, \frac{d\mathring{r}_N^y}{d\gamma}, \frac{d\mathring{\ell}_N}{d\gamma}\right]^{\mathrm{T}}, \tag{4.36}$$

one can write

$$\frac{d\,|\tilde{F}(\boldsymbol{q}(\gamma))\rangle}{d\gamma}\Big|_{\boldsymbol{q}(\gamma)=\boldsymbol{q}^{\mathrm{FB}}(\gamma)} = -\,|\Xi\rangle + \tilde{\mathcal{H}}\left|\frac{d\mathring{q}}{d\gamma}\right\rangle, \tag{4.37}$$

where we have used Eqs. (4.11) and (4.12). The first and second terms on the RHS of Eq. (4.37) represent the strain derivatives of the forces for the contributions from the affine and nonaffine displacements, respectively. In Eq. (4.37) we have introduced $|\Xi\rangle$, which is defined as:

$$|\Xi\rangle := \sum_j \begin{bmatrix} \mathcal{H}^{xx}_{N,j1} r^y_{1j} \\ \mathcal{H}^{xy}_{N,j1} r^y_{1j} \\ \mathcal{H}^{x\ell}_{N,j1} r^y_{1j} \\ \vdots \\ \mathcal{H}^{xx}_{N,jN} r^y_{Nj} \\ \mathcal{H}^{xy}_{N,jN} r^y_{Nj} \\ \mathcal{H}^{x\ell}_{N,jN} r^y_{Nj} \end{bmatrix}. \tag{4.38}$$

We have used $\tilde{\mathcal{H}}$ in Eq. (4.37), which is defined as

$$\tilde{\mathcal{H}}^{\alpha\beta}_{ii} := \begin{cases} -\mathcal{H}^{\ell x}_{ii} & (\alpha = \ell,\ \beta = x) \\ -\mathcal{H}^{\ell y}_{ii} & (\alpha = \ell,\ \beta = y) \\ \mathcal{H}^{\alpha\beta}_{ii} & (\text{otherwise}) \end{cases} \tag{4.39}$$

and

$$\tilde{\mathcal{H}}^{\alpha\beta}_{ij} := \begin{cases} -\mathcal{H}^{x\ell}_{ij} & (\alpha = x,\ \beta = \ell) \\ -\mathcal{H}^{y\ell}_{ij} & (\alpha = y,\ \beta = \ell) \\ \mathcal{H}^{\alpha\beta}_{ij} & (\text{otherwise}) \end{cases} \tag{4.40}$$

for $i \neq j$. Note that $\mathcal{H}^{\alpha\beta}_{T,ij}$ or $\tilde{\mathcal{H}}^{\alpha\beta}_{T,ij}$ does not affect $|\Xi\rangle$, because the affine displacements are instantaneously applied to the system as a step strain. Thus, the integral interval of the tangential displacement during the affine deformation is zero.

Expanding the nonaffine displacements by the eigenvectors of $\tilde{\mathcal{H}}$ and using the fact that the left-hand side of Eq. (4.37) is zero, we obtain

$$\left|\frac{d\mathring{q}}{d\gamma}\right\rangle = \sum_n{}' \frac{\langle\tilde{\Phi}_n|\Xi\rangle}{\tilde{\lambda}_n}|\tilde{\Phi}_n\rangle, \tag{4.41}$$

where $\tilde{\lambda}_n$ and $|\tilde{\Phi}_n\rangle$ are the n-th eigenvalues of $\tilde{\mathcal{H}}$, and the eigenvector corresponding to $\tilde{\lambda}_n$, respectively. Here, $\sum_n'$ on the RHS of Eq. (4.41) excludes low-frequency modes for $\tilde{\lambda}_n t_0^2/m \leq 10^{-12}$ to maintain the numerical accuracy. Note that $|\tilde{\Phi}_n\rangle$ satisfies the orthonormal relation $\langle\tilde{\Phi}_m|\tilde{\Phi}_n\rangle = \delta_{mn}$, if all eigenstates are non-degenerate. The expression for $d\mathring{q}/d\gamma$ in Eq. (4.41) leads to a discontinuous change in $d\mathring{q}/d\gamma$ at a critical strain γ_c for a plastic event because the eigenvectors and eigenvalues are discontinuously changed at this point.

The rigidity is decomposed into two parts:

$$g := g_{\rm A} + g_{\rm NA}, \tag{4.42}$$

where $g_{\rm A}$ and $g_{\rm NA}$ are the rigidities corresponding to the affine and nonaffine displacements, respectively, for one sample. With the aid of Eqs. (4.15), (4.18), and (4.40), the expressions for $g_{\rm A}$ and $g_{\rm NA}$ can be obtained as:

$$g_{\rm A} := \frac{1}{4L^2}\sum_{i,j(i\neq j)} r^y_{ij}\left[r^y_{ij}\mathcal{H}^{xx}_{N,ji} + r^x_{ij}\mathcal{H}^{yx}_{N,ji}\right], \tag{4.43}$$

$$g_{\rm NA} := \frac{1}{4L^2}\sum_{i,j(i\neq j)}\Bigg[\sum_{\zeta=x,y}\left(r^y_{ij}\tilde{\mathcal{H}}^{x\zeta}_{ij} + r^x_{ij}\tilde{\mathcal{H}}^{y\zeta}_{ij}\right)\frac{d\mathring{r}^\zeta_{ij}}{d\gamma} - \left(r^y_{ij}\tilde{\mathcal{H}}^{x\ell}_{ij} + r^x_{ij}\tilde{\mathcal{H}}^{y\ell}_{ij}\right)\frac{d\mathring{\ell}_{ij}}{d\gamma}\Bigg], \tag{4.44}$$

where we have introduced

$$\frac{d\mathring{r}^\zeta_{ij}}{d\gamma} := \frac{d\mathring{r}^\zeta_i}{d\gamma} - \frac{d\mathring{r}^\zeta_j}{d\gamma}, \tag{4.45}$$

$$\frac{d\mathring{\ell}_{ij}}{d\gamma} := \frac{d\mathring{\ell}_i}{d\gamma} + \frac{d\mathring{\ell}_j}{d\gamma}. \tag{4.46}$$

Substituting Eq. (4.41) into Eq. (4.44), $g_{\rm NA}$ can be rewritten as

$$g_{\rm NA} = -\frac{1}{L^2}\sum_n{}' \frac{\langle\tilde{\Phi}_n|\Xi\rangle\langle\Theta|\tilde{\Phi}_n\rangle}{\tilde{\lambda}_n}, \tag{4.47}$$

where we have introduced

$$\langle\Theta| := \frac{1}{2}\sum_j \begin{bmatrix} \left(r^y_{1j}\tilde{\mathcal{H}}^{xx}_{j1} + r^x_{1j}\tilde{\mathcal{H}}^{yx}_{j1}\right) \\ \left(r^y_{1j}\tilde{\mathcal{H}}^{xy}_{j1} + r^x_{1j}\tilde{\mathcal{H}}^{yy}_{j1}\right) \\ \left(r^y_{1j}\tilde{\mathcal{J}}^{x\ell}_{j1} + r^x_{1j}\tilde{\mathcal{J}}^{y\ell}_{j1}\right) \\ \vdots, \\ \left(r^y_{Nj}\tilde{\mathcal{J}}^{xx}_{jN} + r^x_{Nj}\tilde{\mathcal{J}}^{yx}_{jN}\right) \\ \left(r^y_{Nj}\tilde{\mathcal{H}}^{xy}_{jN} + r^x_{Nj}\tilde{\mathcal{H}}^{yy}_{jN}\right) \\ \left(r^y_{Nj}\tilde{\mathcal{H}}^{x\ell}_{jN} + r^x_{Nj}\tilde{\mathcal{H}}^{y\ell}_{jN}\right) \end{bmatrix}^{\mathrm{T}}. \tag{4.48}$$

The affine rigidity can be also expressed as

$$g_{\mathrm{A}} = \frac{1}{L^2}\langle Y|\Xi\rangle, \tag{4.49}$$

where

$$\langle Y| := [y_1, 0, 0, y_2, 0, 0, \cdots, y_N, 0, 0]. \tag{4.50}$$

To verify the validity of the theoretical treatment, we introduce the theoretical stress $\sigma^{\mathrm{th}}(\gamma)$ with the aid of Eq.(4.42) as

$$\sigma^{\mathrm{th}}(\gamma + \Delta\gamma) := \sigma(\boldsymbol{q}^{\mathrm{FB}}(\gamma)) + g(\gamma)\Delta\gamma. \tag{4.51}$$

4.4 Results and discussion

We verify the validity of the shear modulus obtained by the eigenvalue analysis by comparing it with that obtained by the simulation. First, we have confirmed the quantitative accuracy of our analysis to obtain the rigidity in the linear response regime of our system (see Appendix J.2), as in Ref. [119] (Chapter 3).

For the numerical FB condition, we use the condition $|\tilde{F}^{\alpha}_i| < F_{\mathrm{Th}}$ for arbitrary i, where we adopt $F_{\mathrm{Th}} = 1.0 \times 10^{-14} k_N d$ for the numerical calculation. In our simulation, we also adopt $\eta_D = \sqrt{k_N/m}$. In this study, we present the results for $k_T/k_N = 1$, $\phi = 0.90$, and $\Delta\gamma_{\mathrm{in}} = 1.0 \times 10^{-4}$ with the ensemble averages of 30 samples, except for Appendix J.2. We ignore the effect of dissipation in the eigenequation because the velocity of each grain is sufficiently small to incur infinitesimal agitation from the FB state. The time step used for the simulation, Δt, is set to $\Delta t = 1.0 \times 10^{-2} t_0$ with $t_0 := \sqrt{m/k_N}$, and numerical integration is performed using the velocity Verlet method.

Now, let us consider a nonlinear regime in which there are many plastic events caused by stress avalanches. Here, we regard an event as plastic if the condition (i) $\sigma(\gamma) - \sigma(\gamma - \Delta\gamma) < 0$ or (ii) $G(\gamma - \Delta\gamma) - G(\gamma) > 1.0 \times 10^{-2} k_N$ is satisfied.

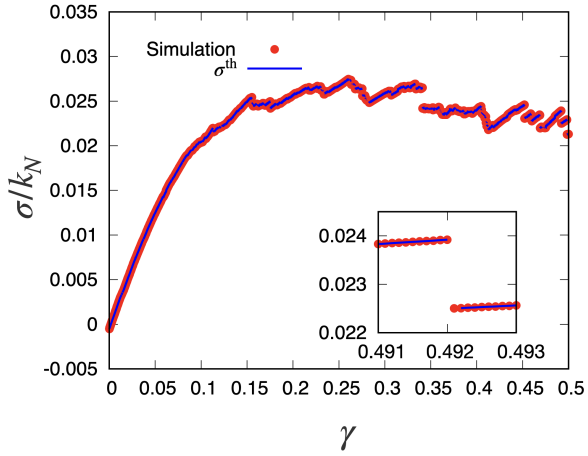

Figure 4.1: A stress-strain curve for $0 \leq \gamma \leq 0.5$ for one sample of the collection of grains ($N = 128$), which includes the theoretical results (line) and simulation results (filled symbols) under the condition$\Delta\gamma_{\mathrm{Th}} = \Delta\gamma_{\mathrm{in}} = 10^{-4}$. The inset is a close-up of the stress-strain curve in the vicinity of a stress-drop event.

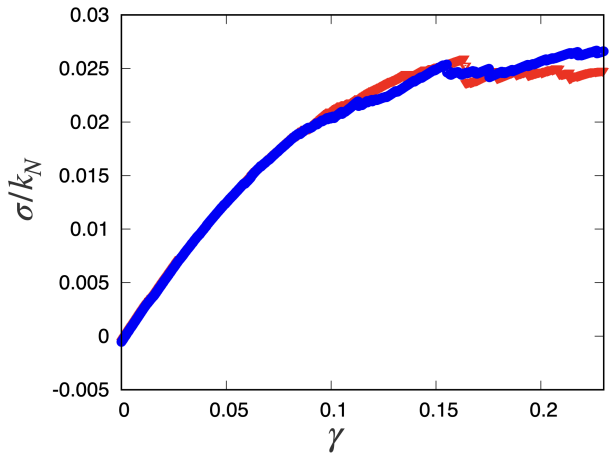

Figure 4.2: Stress-strain relations for $\Delta\gamma_{\mathrm{Th}} = 1.0 \times 10^{-4}$ (blue circles) and $\Delta\gamma_{\mathrm{Th}} = 1.0 \times 10^{-8}$ (red triangles) with $N = 128$.

Figure 4.1 shows a typical example of the stress-strain curve obtained by one sample of the collection of grains based on both the simulation and eigenvalue analysis developed in the previous section under the condition $\Delta\gamma_{\rm Th} = \Delta\gamma_{\rm in}$. It should be noted that the difference between the theoretical and simulation results is almost invisible, even in the presence of avalanches. However, the eigenvalue analysis cannot be used immediately after plastic events, that is, for $\gamma \approx \gamma_c$ (see the inset of Fig. 4.1), because the stress is not determined by Eq. (4.51) immediately after a plastic event.

Figure 4.2 shows a comparison of the stress-strain curve for $\Delta\gamma_{\rm Th} = 10^{-4}\Delta\gamma_{\rm in}$ (blue circles) with those for $\Delta\gamma_{\rm Th} = \Delta\gamma_{\rm in}$ (red triangles). From the figure, we cannot find any $\Delta\gamma_{\rm Th}$ dependence for $\gamma < 0.08$, but some differences for larger γ can be observed as a result of stress avalanches.

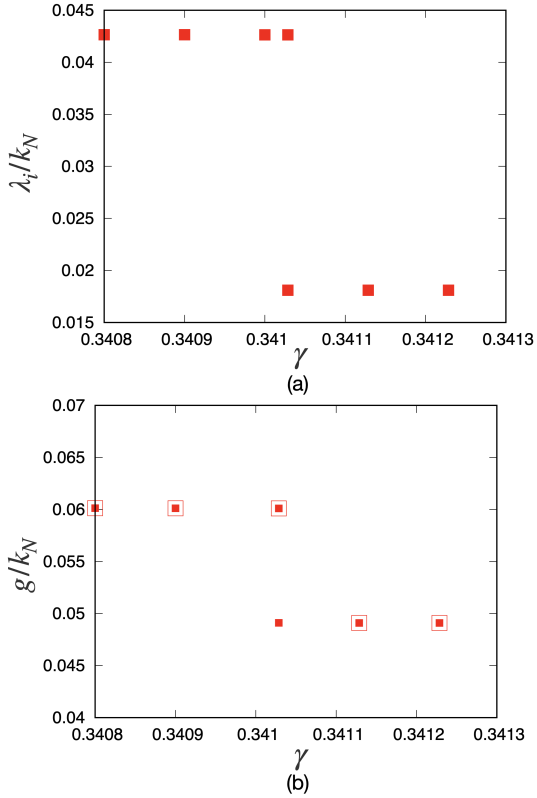

Figure 4.3: Plots of (a) the smallest eigenvalue except for the zero modes and (b) the rigidity g based on the eigenvalue analysis (open symbols) and numerical shear stress (filled symbols) against γ for $0.3408 \leq \gamma \leq 0.3413$ and $N = 128$.

We might expect that some precursors of a stress-drop event can be detected from the behavior of the smallest non-zero eigenvalue. To verify this expectation, we plot the smallest non-zero eigenvalues in Fig. 4.3(a) near a critical strain

with $\Delta\gamma_{\rm Th} = 10^{-8}$. It can be observed that the eigenvalues changes discontinuously at the critical strain ($\gamma_c = 0.34102862$ for $\gamma_{\rm Th} = 10^{-8}$), where the critical strain converges if $\Delta\gamma_{\rm Th} < 10^{-6}$ (see Appendix G for details). Notably, there is no precursor for the smallest eigenvalue below the critical strain, in contrast to Refs. [107, 108, 111, 112], where non-harmonic potentials are used. Correspondingly, we cannot find any singularity of the rigidity as $g - g_{\rm reg} \sim -(\gamma_c - \gamma)^{-1/2}$ as in Fig. 4.3(b) for $\gamma \lesssim \gamma_c$ predicted in Refs. [107,108,110,114]. The absence of the precursors and singularities in our model can be understood in the form of the Hessian matrix presented in Appendix I.3. In non-harmonic systems, some elements of the Hessian matrix become zero as $\xi_{N,ij} \to 0$ when the contact between the i-th and j-th grains disappears. This leads to the precursors and singularities [107,108]. However, in the harmonic systems, the corresponding element approaches a non-zero constant in the limit $\xi_{N,ij} \to 0$ (see Appendix I.3), which results in the absence of the precursors.

Figure 4.4 shows a set of plots of the eigenvectors corresponding to the smallest eigenvalue at (a) γ_{c-} and at (b)γ_{c+}, where γ_{c+} is the strain immediately after the plastic event, and $\gamma_{c-} := \gamma_{c+} - \Delta\gamma_{\rm Th}$ is the strain just before the event. As shown in Fig. 4.4, changes in eigenvectors owing to the stress drop event can be observed. Here, we find the existence of domains of grains of clockwise rotation and counter-clockwise rotation, and the collective motion of grains between two domains. We may observe the excitation of the quadrupole-like mode, although its structure is not sufficiently clear.

Figure 4.5 is the comparison of $|d\mathring{q}/d\gamma\rangle$ obtained by the eigenvalue analysis (a) with that by the simulation (b) at $\gamma = \gamma_{c+}$, where $|d\mathring{q}/d\gamma\rangle$ in the simulation is evaluated by $(\mathring{\boldsymbol{q}}(\gamma_{c+} + \Delta\gamma_{\rm Th}) - \mathring{\boldsymbol{q}}(\gamma_{c+}))/\Delta\gamma_{\rm Th}$ with $\Delta\gamma_{\rm Th} = 1.0 \times 10^{-8}$. It is obvious that the difference between the two figures is invisible, though the quadrupole-like structure cannot be clearly seen as in Fig. 4.4. Nevertheless, we can find the collective motion of grains in both figures.

Because we cannot use the eigenvalue analysis at the critical strain γ_c for a plastic event, let us analyze the nonaffine displacement $\Delta\mathring{\boldsymbol{q}}$ between γ_{c-} and γ_{c+} caused by an avalanche using the simulation:

$$\Delta\mathring{\boldsymbol{q}}|_c := \begin{bmatrix} \Delta\mathring{\boldsymbol{q}}_1|_c \\ \Delta\mathring{\boldsymbol{q}}_2|_c \\ \vdots \\ \Delta\mathring{\boldsymbol{q}}_N|_c \end{bmatrix}, \tag{4.52}$$

where

$$\Delta\mathring{\boldsymbol{q}}_i|_c := \begin{bmatrix} r_i^{{\rm FB},x}(\gamma_{c+}) - r_i^{{\rm FB},x}(\gamma_{c-}) - \Delta\gamma r_i^{{\rm FB},y}(\gamma_{c-}) \\ r_i^{{\rm FB},y}(\gamma_{c+}) - r_i^{{\rm FB},y}(\gamma_{c-}) \\ \ell_i^{\rm FB}(\gamma_{c+}) - \ell_i^{\rm FB}(\gamma_{c-}) \end{bmatrix}. \tag{4.53}$$

Figure 4.6 shows a plot of the nonaffine displacement $\Delta\mathring{\boldsymbol{q}}|_c$ around a yielding point based on the simulation for $N = 1024$ at $\Delta\gamma_{\rm Th} = 1.0 \times 10^{-8}$. This figure indicates that (i) grains move with rotations, which is one of the effects of mutual frictions between grains, and (ii) the existence of a quadrupole consisting

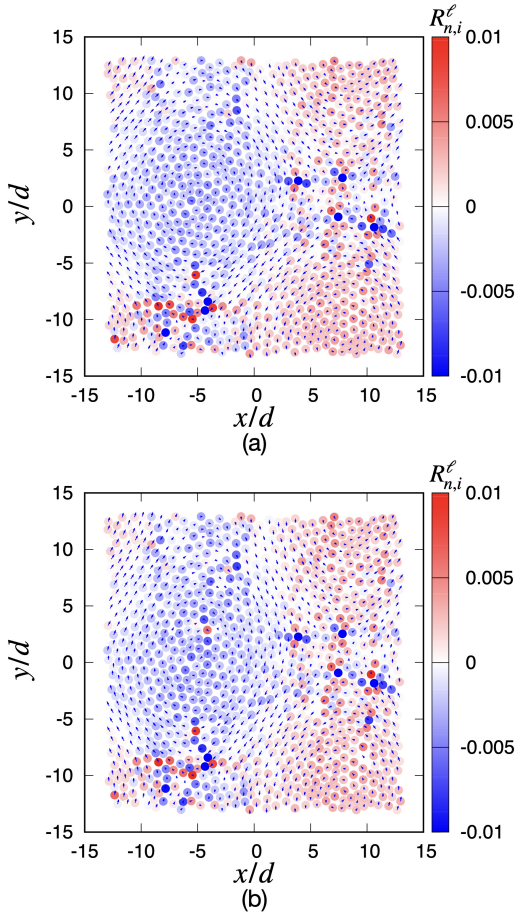

Figure 4.4: Plots of eigenvectors at (a) γ_{c-} and at (b) γ_{c+} corresponding to the smallest eigenvalue. For visualization, the magnitudes of the vectors are three times larger than their true values ($N = 1024$).

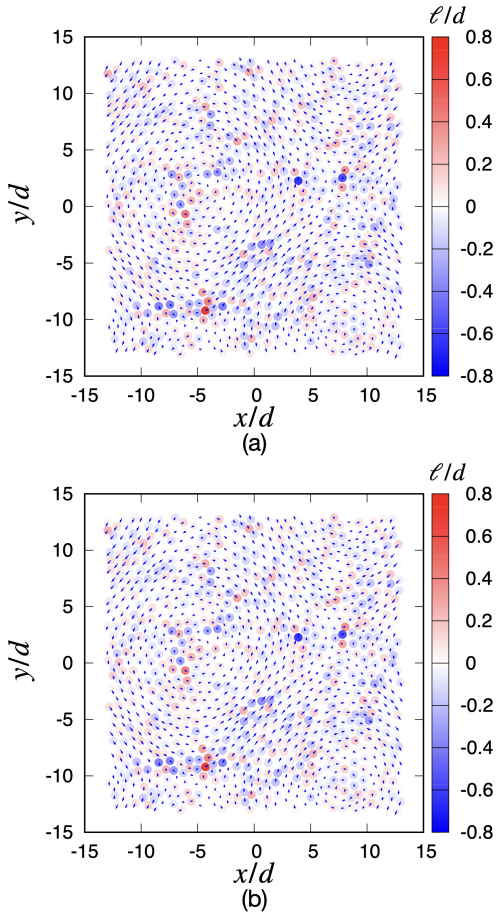

Figure 4.5: Plots of $|d\mathring{q}/d\gamma\rangle$ at $\gamma = \gamma_{c+}$ for $N = 1024$ and $\Delta\gamma_{\rm Th} = 1.0 \times 10^{-8}$, where (a) and (b) are based on the eigenvalue analysis and simulation, respectively. For visualization, we magnify the magnitudes of the vectors with the factor 10.0.

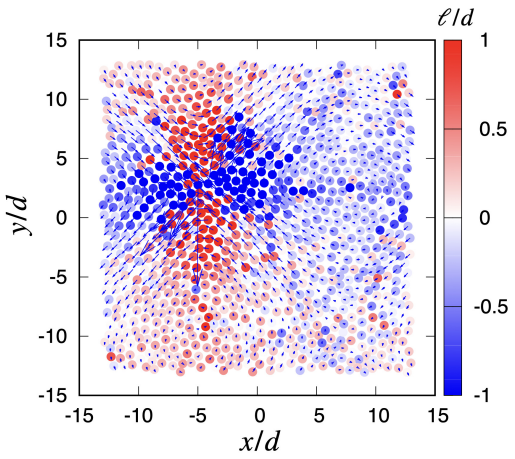

Figure 4.6: Plot of $\Delta\mathring{q}|_c$ in the simulation for $N = 1024$ and $\Delta\gamma_{\rm Th} = 1.0\times10^{-8}$. For visualization, we magnify $\Delta\mathring{q}|_c$ with the factor 1.0×10^3.

of four domains of collective rotating grains exists. In particular, the rotations of the grains are sharply changed on the boundary between the domains. Unfortunately, $\Delta\mathring{\boldsymbol{q}}|_c$ cannot be described by the eigenvalue analysis, because $\Delta\mathring{\boldsymbol{q}}|_c$ expresses the configuration change, which is unstable for a small change in γ.

Figures 4.7 (a) and (b) show plots of the rigidity and smallest eigenvalue from $\gamma = 0$ to 0.002, which includes two plastic events based on the one-sample calculation of the collection of grains with $N = 128$. One can find an almost perfect agreement of the rigidity between the eigenvalue analysis and simulation, except for the yielding points (see Fig. 4.7 (a)). We find discontinuous changes in the smallest eigenvalue at the yielding point, where the rigidity changes discontinuously (see Figs. 4.7 (b). As expected, the magnitude of the discontinuous change in rigidity at the yielding point in Fig. 4.7 (a) for $\gamma \approx 0.001$ is smaller than that for a point of a stress drop for $\gamma \approx 0.341$, as shown in Fig. 4.3.

Figure 4.8 shows the stress-strain curve corresponding to Fig. 4.7. It is difficult to find the plastic events in the main figure of Fig. 4.8, but we can find a small stress drop at this point if we use a close-up figure in the inset. We verify the creation and annihilation of contacting pairs at the stress drop points. The stress expression in Eq. (4.51) cannot be used at the yielding point; thus a disagreement exists between the eigenvalue analysis and simulation at the point in the inset of Fig. 4.8.

Figure 4.9 plots the rigidity of G over 30 samples for $N = 128$, where we have omitted the data if stress drop events take place. We verify that rigidity based on the eigenvalue analysis reproduces the results of the simulation. Note that non-monotonic changes in G originate from changes in the contact points and configuration of grains.

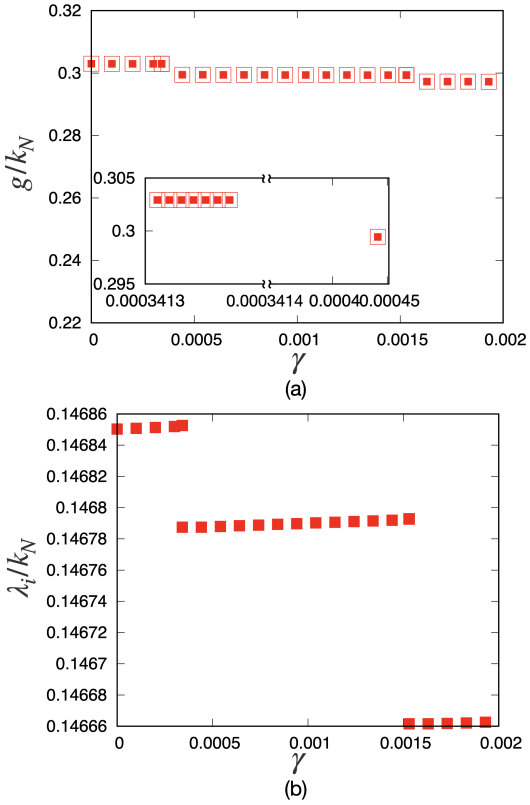

Figure 4.7: Plots of the shear modulus with (a) the theoretical evaluation (open symbols) and the simulation results (filled symbols) except for critical strain with the close-up of g near a yielding point (inset), and (b) the smallest eigenvalue, except for zero modes against γ for $0 \leq \gamma \leq 0.002$ for $N = 128$. Note that the rigidity is not plotted at the yielding points, because it diverges there.

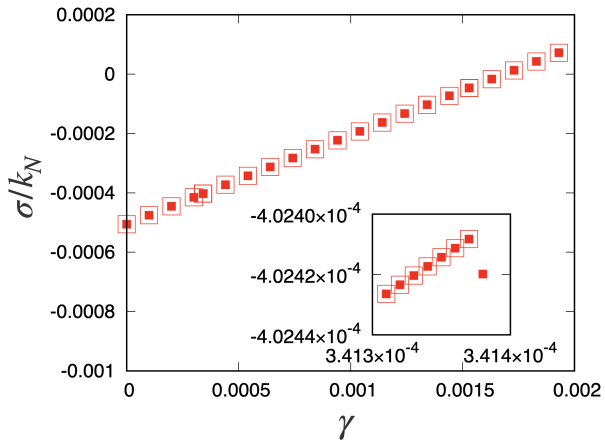

Figure 4.8: The plot of the stress-strain curve in the region $0 \leq \gamma \leq 0.002$ for $N = 128$.

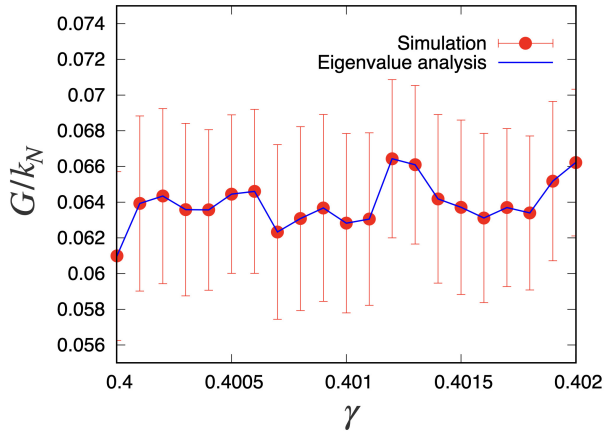

Figure 4.9: Plots of the rigidity G based on the eigenvalue analysis (line) and on the simulation (filled symbols) with $\Delta\gamma_{\rm Th} = 1.0 \times 10^{-4}$. We have used 30 samples for $N = 128$, where the error bars represent the standard deviations for γ. Note that we have omitted the data if stress-drop events occur.

4.5 Conclusion of this Chapter

In this Chapter, we have demonstrated that eigenvalue analysis of the Hessian matrix provides precise descriptions of the rigidity and stress of dispersed frictional grains in which the contact force is described by the harmonic potential, in spite of stress-drop events, such as stress avalanches. However, our model does not contain any slip processes between contacting grains. This success is a natural extension of the previous studies on frictionless grains [107, 108] to frictional grains and of our previous study on the linear response regime (Chapter 3) [119] to the nonlinear response regime. Two remarkable features of the contacting model are described by the harmonic potential. First, the tangential contact force in this model is no longer a history-dependent one. This leads to the significant simplification of the theoretical analysis. Second, unlike the naive expectation, the eigenvalues in our model do not indicate any precursors for the stress-drop events. In essence, stress-drop events take place suddenly by releasing contact points.

Some future tasks that need to be addressed are as follows. First, we need to consider the effect of slips, which causes a significant difference from our model because history-dependent contacts play important roles in the presence of slip events. Second, we must extend our analysis to nonlinear interacting models, such as the Hertzian contact model in a three-dimensional space. We plan on working on these points in the future.

Chapter 5

Conclusions and outlook

5.1 Conclusions

Chapter 3 presented an analysis of the eigenmodes of the Jacobian matrix for systems of grains interacting with Hertzian force. Consequently, an expression for the rigidity of amorphous solids comprising frictional grains interacting with the Hertzian force under an infinitesimal strain was obtained. It was confirmed that the DOS could be divided into two regions. In the low-frequency region (Region I), the rotation of the grains was dominant. These modes are characterized by the frequency $(k_T/k_N)^{1/2}/t_0$, where $t_0 := (m/k_N)^{1/2}d^{-1/4}$. Region I was found to merge into the high-frequency region (Region II) in case of large k_T/k_N, with translational modes dominating Region II. For a sufficiently small k_T/k_N, the DOS obtained from the eigenvalue analysis of the Jacobian matrix was similar to that obtained using the Hessian matrix analysis. However, the difference between the DOS obtained using the Jacobian and that using the Hessian was visible for $k_T \geq k_N$. Therefore, the eigenvalue analysis is significant for large k_T/k_N. Moreover, the rigidity obtained by the Jacobian matrix was consistent with that obtained from the simulation. Furthermore, it was confirmed that the translational modes determined the rigidity.

Chapter 4 demonstrated that the eigenvalue analysis of the Hessian matrix provided precise descriptions of the rigidity and stress of dispersed frictional grains wherein the contact force was described by the harmonic potential, despite the existence of stress-drop events such as stress avalanches. The proposed model did not contain any slip processes between contacting grains. This success is a natural extension of the previous studies on frictionless grains [107, 108] to frictional grains and a previous study on the linear response regime presented in Chapter 3 to the nonlinear response regime. The harmonic potential described two remarkable features of the contacting model. First, the tangential contact force in this model is no longer history-dependent. This resulted in the significant simplification of the theoretical analysis. Second, in contrast to the naive expectation, the eigenvalues in the proposed model did not indicate

any precursors for the stress-drop events. In essence, the stress-drop events occurred suddenly through the release of contact points. Third, this analysis should be extended without using the data of grains' configuration. Although the analysis is consistent with the results of the simulation, it cannot be a purely theoretical one because the configuration is determined by the simulation. If an approximate configuration of grains can be formulated based on a theory, it can be claimed that the problem has been solved based on the theory. Thus, the theoretical determination of grains ' configuration will be important in future work.

5.2 Outlook

Some future tasks that need to be addressed are as follows. First, the effect of slips must be considered, as they cause a significant difference from the proposed model because history-dependent contacts play essential roles in the presence of slip events. Second, the proposed analysis must be extended to nonlinear interacting models for finite strain, such as the Hertzian contact model in a three-dimensional space. These aspects will be worked upon in future studies.

Acknowledgments

I would like to express my sincere gratitude to Prof. Hisao Hayakawa, who is my supervisor in the graduate course of science at Kyoto University. I appreciate many things he taught me about physics, research and scientific thinking. I am grateful for all the advice he gave me in writing this thesis. I am also grateful to all supporting staff of Yukawa Institute for Theoretical Physics (YITP) and the Division of Physics and Astronomy, Kyoto University, for their kind guidance and support.

I also thank Prof. Satoshi Takada, Prof. Takeshi Kawasaki, Prof. Ryohei Seto, Dr. Norihiro Oyama, and Japanese researchers belonging to granular physics community for their great help and fruitful discussions. I would also like to thank Prof. Kuniyasu Saitoh and Prof. Michio Otsuki for their cooperation on parts of this thesis and for agreeing to include the results of joint papers written in Chapters 3 and 4 in this thesis. I would be grateful to Prof. Frederic van Wijland, Prof. Itamar Procaccia, and Mr. Federico Ghimenti for the fruitful discussion and comments. I also appreciate Prof. Ryo Hanai and Dr. Amit Kumar Chatterjee for their critical reading of this thesis. Some of the numerical calculations in this thesis were performed using computers at YITP. My research was partially supported by Grant-in-Aid from the Japan Society for Promotion of Science JSPS Research Fellow (Grant No. JP20J20292), Grants-in-Aid of MEXT Japan for Scientific Research (Grant Nos. JP16H04025 and JP21H01006), Programs YITP-T-18-03, YITP-W-18-17, and YITP-W-22-15 and ISHIZUE 2020 of Kyoto University Research Development Program.

I am grateful to my current and previous lab mates, Prof. Tomohiko Sano, Dr. Pradipto, Dr. Ville M. M. Paasonen, Mr. Yuki Hino, Prof. Hiroyasu Tajima, Dr. Yu Watanabe, and Mr. Kazuhito Kuramoto, and my colleague Mr. Kiwamu Yoshii for their insights and moral supports. Finally, I would like to express my gratitude to my family, including my wife, Rina, and friends, for supporting my research and understanding my life.

Appendix A

Jacobian properties

In this appendix, we summarize the properties of the Jacobian introduced in Eq. (3.20).

A.1 Jacobian block elements

Let us write 3×3 sub-matrix $\mathcal{J}_{ij}$, which is (ij) block element of the Jacobian obtained from Eq. (3.20):

$$
\begin{aligned}
[\mathcal{J}_{ij}]^{\alpha\beta} &:= -\frac{\partial \tilde{F}_i^{\alpha}}{\partial q_j^{\beta}} \\
&= \begin{bmatrix} -\partial_{q_j^x} F_i^x & -\partial_{q_j^y} F_i^x & -\partial_{q_j^\ell} F_i^x \\ -\partial_{q_j^x} F_i^y & -\partial_{q_j^y} F_i^y & -\partial_{q_j^\ell} F_i^y \\ -\partial_{q_j^x} \tilde{T}_i & -\partial_{q_j^y} \tilde{T}_i & -\partial_{q_j^\ell} \tilde{T}_i \end{bmatrix} \\
&= \begin{bmatrix} -\sum_{k=1;k\neq j}^N \partial_{q_j^x} f_{ik}^x & -\sum_{k=1;k\neq j}^N \partial_{q_j^y} f_{ik}^x & -\sum_{k=1;k\neq j}^N \partial_{q_j^\ell} f_{ik}^x \\ -\sum_{k=1;k\neq j}^N \partial_{q_j^x} f_{ik}^y & -\sum_{k=1;k\neq j}^N \partial_{q_j^y} f_{ik}^y & -\sum_{k=1;k\neq j}^N \partial_{q_j^\ell} f_{ik}^y \\ -\sum_{k=1;k\neq j}^N \partial_{q_j^x} \tilde{T}_{ik} & -\sum_{k=1;k\neq j}^N \partial_{q_j^y} \tilde{T}_{ik} & -\sum_{k=1;k\neq j}^N \partial_{q_j^\ell} \tilde{T}_{ik} \end{bmatrix} \\
&= \begin{cases} \begin{bmatrix} -\partial_{q_j^x} f_{ij}^x & -\partial_{q_j^y} f_{ij}^x & -\partial_{q_j^\ell} f_{ij}^x \\ -\partial_{q_j^x} f_{ij}^y & -\partial_{q_j^y} f_{ij}^y & -\partial_{q_j^\ell} f_{ij}^y \\ -\partial_{q_j^x} \tilde{T}_{ij} & -\partial_{q_j^y} \tilde{T}_{ij} & -\partial_{q_j^\ell} \tilde{T}_{ij} \end{bmatrix} (i \neq j) \\ \begin{bmatrix} -\sum_{k=1;k\neq i}^N \partial_{q_i^x} f_{ik}^x & -\sum_{k=1;k\neq i}^N \partial_{q_i^y} f_{ik}^x & -\sum_{k=1;k\neq i}^N \partial_{q_i^\ell} f_{ik}^x \\ -\sum_{k=1;k\neq i}^N \partial_{q_i^x} f_{ik}^y & -\sum_{k=1;k\neq i}^N \partial_{q_i^y} f_{ik}^y & -\sum_{k=1;k\neq i}^N \partial_{q_i^\ell} f_{ik}^y \\ -\sum_{k=1;k\neq i}^N \partial_{q_i^x} \tilde{T}_{ik} & -\sum_{k=1;k\neq i}^N \partial_{q_i^y} \tilde{T}_{ik} & -\sum_{k=1;k\neq i}^N \partial_{q_i^\ell} \tilde{T}_{ik} \end{bmatrix} (i = j) \end{cases},
\end{aligned}
\tag{A.1}
$$

where the superscripts α and β correspond to x, y, ℓ-components, and i and j are the grain numbers (see Appendix B for each component of $\mathcal{J}$). Here, $f_{ij}^{\zeta}, \tilde{T}_{ij}$

are ζ-component of $\boldsymbol{f}_{ij}$ and scaled torque that the i-th grain receives from the j-th grain, respectively. The sub-matrix for $i = j$ is given by

$$[\mathcal{J}_{ii}]^{\alpha\beta} = \begin{bmatrix} \sum_{k=1;k\neq i}^{N} \partial_{q_k^x} f_{ik}^x & \sum_{k=1;k\neq i}^{N} \partial_{q_k^y} f_{ik}^x & -\sum_{k=1;k\neq i}^{N} \partial_{q_k^\ell} f_{ik}^x \\ \sum_{k=1;k\neq i}^{N} \partial_{q_k^x} f_{ik}^y & \sum_{k=1;k\neq i}^{N} \partial_{q_k^y} f_{ik}^y & -\sum_{k=1;k\neq i}^{N} \partial_{q_k^\ell} f_{ik}^y \\ \sum_{k=1;k\neq i}^{N} \partial_{q_k^x} \tilde{T}_{ik} & \sum_{k=1;k\neq i}^{N} \partial_{q_k^y} \tilde{T}_{ik} & -\sum_{k=1;k\neq i}^{N} \partial_{q_k^\ell} \tilde{T}_{ik} \end{bmatrix}, \quad \text{(A.2)}$$

where we have used $\partial_{q_i^\kappa} f_{ik}^\zeta = -\partial_{q_k^\kappa} f_{ik}^\zeta, \partial_{q_i^\kappa} \tilde{T}_{ik} = -\partial_{q_i^\kappa} \tilde{T}_{ik}, \partial_{q_i^\ell} f_{ik}^\zeta = \partial_{q_k^\ell} f_{ik}^\zeta$, and $\partial_{q_i^\ell} \tilde{T}_{ik} = \partial_{q_i^\ell} \tilde{T}_{ik}$. Here, the superscripts ζ and κ correspond to x, y components.

From Eqs. (A.1) and (A.2) $\mathcal{J}_{ij}^{\zeta\beta}$ satisfies

$$\mathcal{J}_{ii}^{\zeta\beta} = -\sum_{j\neq i} \mathcal{J}_{ij}^{\zeta\beta} \quad \text{(A.3)}$$

Thus, introducing J_{nm} $(n, m = 1, 2, \cdots, 3N)$ which is a rewriting of $\mathcal{J}_{ij}^{\alpha\beta}$ in Eq. (3.21) by the index from i and α to n, we obtain

$$\sum_{n=1,4,\cdots,3N-2} J_{nm} = 0, \quad \text{(A.4)}$$

$$\sum_{n=2,5,\cdots,3N-1} J_{nm} = 0. \quad \text{(A.5)}$$

where $\sum_{n=1,4,\cdots,3N-2}$ and $\sum_{n=2,5,\cdots,3N-1}$ express the summations of modulus 1 and modulus 2 with the intervals 3, respectively. Here, we write $3N$-dimensional vector translating in the x direction $\boldsymbol{e}_x$ as

$$\boldsymbol{e}_x = \begin{bmatrix} \boldsymbol{e}_{x,1} \\ \boldsymbol{e}_{x,2} \\ \vdots \\ \boldsymbol{e}_{x,N} \end{bmatrix}. \quad \text{(A.6)}$$

where $\boldsymbol{e}_{x,i} := (1, 0, 0)^{\mathrm{T}}$ for $i = 1, 2, \cdots, N$. Here, the n-th component of the action of $\mathcal{J}$ on $\boldsymbol{e}_x$ satisfies

$$\begin{aligned} \{\mathcal{J}\boldsymbol{e}_x\}_n &= \sum_m J_{nm} e_{x,m} \\ &= \sum_{m=1,4,\cdots,3N-2} J_{nm} \\ &= 0, \end{aligned} \quad \text{(A.7)}$$

where we have used Eq. (A.4) for the last equality. Thus, we obtain $\mathcal{J}\boldsymbol{e}_x = \boldsymbol{0}$, where $\boldsymbol{0}$ is zero vector. Similarly, using

$$\boldsymbol{e}_y = \begin{bmatrix} \boldsymbol{e}_{y,1} \\ \boldsymbol{e}_{y,2} \\ \vdots \\ \boldsymbol{e}_{y,N} \end{bmatrix}, \quad \text{(A.8)}$$

with $\boldsymbol{e}_{y,i} := (0,1,0)^{\mathrm{T}}$ we also obtain $\mathcal{J}\boldsymbol{e}_y = \mathbf{0}$. Therefore, $\boldsymbol{e}_x$ and $\boldsymbol{e}_y$ are the zero modes for $\mathcal{J}$.

Appendix B

Explicit Jacobian expressions with Hertzian force

In this appendix, we present the explicit expressions of the Jacobian with the Hertzian contact force based on Eqs. (3.6)–(3.8). Then, we clarify the difference between the present results and the case where the tangential force is approximated by the conservative force used in the previous studies [104, 105].

B.1 Calculation of Jacobian

Let us consider only the normal and tangential elastic contact forces

$$\boldsymbol{f}_{N,ij} = k_N \xi_{N,ij}^{3/2} \boldsymbol{n}_{ij}, \tag{B.1}$$

$$\boldsymbol{f}_{T,ij} = k_T \xi_{N,ij}^{1/2} \boldsymbol{\xi}_{T,ij}, \tag{B.2}$$

where the integration of $d\boldsymbol{\xi}_{T,ij}$

$$\boldsymbol{\xi}_{T,ij} := \int_{C_{ij}} d\boldsymbol{\xi}_{T,ij} \tag{B.3}$$

is performed during the contact between i and j grains. Since Eq. (B.3) does not contain the second term on RHS of Eq. (3.9), $\boldsymbol{\xi}_{T,ij}$ may not be perpendicular to $\boldsymbol{\xi}_{N,ij}$. Neverthelss, we adopt Eq. (B.3) for simplicity. Here, $d\boldsymbol{\xi}_{T,ij}$ is defined as

$$d\boldsymbol{\xi}_{T,ij} = d\boldsymbol{r}_{ij} - (d\boldsymbol{r}_{ij} \cdot \boldsymbol{n}_{ij})\boldsymbol{n}_{ij} - d\boldsymbol{\ell}_{ij} \times \boldsymbol{n}_{ij}, \tag{B.4}$$

where $\boldsymbol{\ell}_{ij}$ is defined as

$$\boldsymbol{\ell}_{ij} := \begin{bmatrix} 0 \\ 0 \\ \ell_i + \ell_j \end{bmatrix}. \tag{B.5}$$

Each component of Eq. (B.4) is written as

$$d\xi^x_{T,ij} = dr^x_{ij} - (d\boldsymbol{r}_{ij} \cdot \boldsymbol{n}_{ij}) n^x_{ij} + d\ell_{ij} n^y_{ij}, \tag{B.6}$$
$$d\xi^y_{T,ij} = dr^y_{ij} - (d\boldsymbol{r}_{ij} \cdot \boldsymbol{n}_{ij}) n^y_{ij} - d\ell_{ij} n^x_{ij}. \tag{B.7}$$

The derivative of the normal force is given by

$$\partial_{r_i^\zeta} f^\kappa_{N,ij} = k_N \left[\delta_{\zeta\kappa} \frac{\xi^{3/2}_{N,ij}}{r_{ij}} - \left(\frac{3}{2} + \frac{\xi_{N,ij}}{r_{ij}} \right) \xi^{1/2}_{N,ij} n^\zeta_{ij} n^\kappa_{ij} \right], \tag{B.8}$$
$$\partial_{\ell_i} f^\kappa_{N,ij} = 0, \tag{B.9}$$

where Kronecker's delta $\delta_{\zeta\kappa}$ satisfies $\delta_{\zeta\kappa} = 1$ for $\zeta = \kappa$ and $\delta_{\zeta\kappa} = 0$ otherwise. We have used

$$\frac{\partial n^\zeta_{ij}}{\partial r^\kappa_i} = \frac{1}{r_{ij}} \left(\delta_{\zeta\kappa} - n^\zeta_{ij} n^\kappa_{ij} \right), \tag{B.10}$$
$$\frac{\partial r_{ij}}{\partial r^\zeta_i} = n^\zeta_{ij} \tag{B.11}$$

to obtain Eq. (B.8).

The derivative of the tangential force is written as

$$\partial_{r_i^\zeta} f^\kappa_{T,ij} = \frac{1}{2} k_T \xi^{-1/2}_{N,ij} n^\zeta_{ij} \xi^\kappa_{T,ij} - k_T \xi^{1/2}_{N,ij} \left(\delta_{\zeta\kappa} - n^\zeta_{ij} n^\kappa_{ij} \right), \tag{B.12}$$
$$\partial_{\ell_i} f^\kappa_{T,ij} = -\varepsilon^\kappa k_T \xi^{1/2}_{N,ij} n^{\nu_\kappa}_{ij}, \tag{B.13}$$

where ε^ζ and ν_ζ are, respectively, defined as

$$\varepsilon^\zeta := \begin{cases} 1 & (\zeta = x) \\ -1 & (\zeta = y), \end{cases} \tag{B.14}$$
$$\nu_\zeta := \begin{cases} y & (\zeta = x) \\ x & (\zeta = y). \end{cases} \tag{B.15}$$

Here, $\partial_{r_i^\zeta} \xi^\kappa_{T,ij}$ and $\partial_{\ell_i} \xi^\kappa_{T,ij}$ in Eqs. (B.12) and (B.13) satisfy

$$\frac{\partial \xi^\kappa_{T,ij}}{\partial r^\zeta_i} = \delta_{\zeta\kappa} - n^\zeta_{ij} n^\kappa_{ij}, \tag{B.16}$$
$$\frac{\partial \xi^\kappa_{T,ij}}{\partial \ell_i} = \epsilon^\kappa n^{\nu_\kappa}_{ij}. \tag{B.17}$$

The derivation of Eqs. (B.16) and (B.17) are as follows [115]. From Eq. (B.4) $d\xi^{\zeta}_{T,ij}$ can be written as

$$d\xi^{\zeta}_{T,ij} = dr^{\zeta}_{ij} - (d\boldsymbol{r}_{ij}\cdot\boldsymbol{n}_{ij})n^{\zeta}_{ij} + (-1)^{\zeta}(d\ell_i + d\ell_j)n^{\nu_\zeta}_{ij}. \tag{B.18}$$

Then, $d\xi^{x}_{T,ij}$ satisfies

$$\begin{aligned} d\xi^{x}_{T,ij} &= dr^{x}_{ij} - \sum_{\kappa=x,y} dr^{\kappa}_{ij}n^{\kappa}_{ij}n^{x}_{ij} + n^{y}_{ij}(d\ell_i + d\ell_j) \\ &= (1-(n^{x}_{ij})^2)dr^{x}_{ij} - n^{x}_{ij}n^{y}_{ij}dr^{y}_{ij} + n^{y}_{ij}(d\ell_i + d\ell_j) \\ &= (n^{y}_{ij})^2 dr^{x}_{ij} - n^{x}_{ij}n^{y}_{ij}dr^{y}_{ij} + n^{y}_{ij}(d\ell_i + d\ell_j) \\ &= (n^{y}_{ij})^2(dx_i - dx_j) - n^{x}_{ij}n^{y}_{ij}(dy_i - dy_j) + n^{y}_{ij}(d\ell_i + d\ell_j). \end{aligned} \tag{B.19}$$

Similarly, $d\xi^{y}_{T,ij}$ also satisfies

$$d\xi^{y}_{T,ij} = -n^{x}_{ij}n^{y}_{ij}(dx_i - dx_j) + (n^{y}_{ij})^2(dy_i - dy_j) - n^{x}_{ij}(d\ell_i + d\ell_j). \tag{B.20}$$

Here, $d\xi^{\zeta}_{T,ij}$is the function of $x_i, y_i, \ell_i, x_j, y_j$, and ℓ_j. We obtain the differential form of $d\xi^{\zeta}_{T,ij}$:

$$\begin{aligned} d\xi^{\zeta}_{T,ij} = &\left(\frac{\partial\xi^{\zeta}_{T,ij}}{\partial x_i}\right)_{(y_i,\ell_i,x_j,y_j,\ell_j)} dx_i + \left(\frac{\partial\xi^{\zeta}_{T,ij}}{\partial x_j}\right)_{(x_i,y_i,\ell_i,y_j,\ell_j)} dx_j \\ &+ \left(\frac{\partial\xi^{\zeta}_{T,ij}}{\partial y_i}\right)_{(x_i,\ell_i,x_j,y_j,\ell_j)} dy_i + \left(\frac{\partial\xi^{\zeta}_{T,ij}}{\partial y_j}\right)_{(x_i,y_i,\ell_i,x_j,\ell_j)} dy_j \\ &+ \left(\frac{\partial\xi^{\zeta}_{T,ij}}{\partial \ell_i}\right)_{(x_i,y_i,x_j,y_j,\ell_j)} d\ell_i + \left(\frac{\partial\xi^{\zeta}_{T,ij}}{\partial \ell_j}\right)_{(x_i,y_i,\ell_i,x_j,y_j)} d\ell_j. \end{aligned} \tag{B.21}$$

Then, we obtain Eqs. (B.16), (B.17), by comparing Eqs. (B.19) and (B.20) with Eq. (B.21).

Since the scaled torque $\tilde{T}_{ij}$ satisfies

$$\tilde{T}_{ij} := \frac{2T_{ij}}{d_i} = -n^{x}_{ij}f^{y}_{T,ij} + n^{y}_{ij}f^{x}_{T,ij}, \tag{B.22}$$

we obtain

$$\begin{aligned}
\partial_{r_i^\zeta}\tilde{T}_{ij} &= -\left(\partial_{r_i^\zeta}n_{ij}^x\right)f_{T,ij}^y - n_{ij}^x\partial_{r_i^\zeta}f_{T,ij}^y + \left(\partial_{r_i^\zeta}n_{ij}^y\right)f_{T,ij}^x + n_{ij}^y\partial_{r_i^\zeta}f_{T,ij}^x \\
&= -\left(\frac{\delta_{\zeta x}}{r_{ij}} - \frac{n_{ij}^\zeta n_{ij}^x}{r_{ij}}\right)f_{T,ij}^y - n_{ij}^x\left[\frac{1}{2}k_T\xi_{N,ij}^{-1/2}\xi_{T,ij}n_{ij}^\zeta t_{ij}^y - k_T\xi_{N,ij}^{1/2}\left(\delta_{\zeta y} - n_{ij}^\zeta n_{ij}^y\right)\right] \\
&\quad + \left(\frac{\delta_{\zeta y}}{r_{ij}} - \frac{n_{ij}^\zeta n_{ij}^y}{r_{ij}}\right)f_{T,ij}^x + n_{ij}^y\left[\frac{1}{2}k_T\xi_{N,ij}^{-1/2}\xi_{T,ij}n_{ij}^\zeta t_{ij}^x - k_T\xi_{N,ij}^{1/2}\left(\delta_{\zeta x} - n_{ij}^\zeta n_{ij}^x\right)\right] \\
&= -n_{ij}^x\left[\frac{1}{2}k_T\xi_{N,ij}^{-1/2}\xi_{T,ij}n_{ij}^\zeta t_{ij}^y - k_T\xi_{N,ij}^{1/2}\left(\delta_{\zeta y} - n_{ij}^\zeta n_{ij}^y\right)\right] \\
&\quad + n_{ij}^y\left[\frac{1}{2}k_T\xi_{N,ij}^{-1/2}\xi_{T,ij}n_{ij}^\zeta t_{ij}^x - k_T\xi_{N,ij}^{1/2}\left(\delta_{\zeta x} - n_{ij}^\zeta n_{ij}^x\right)\right] \\
&= -n_{ij}^x\left[\frac{1}{2}k_T\xi_{N,ij}^{-1/2}\xi_{T,ij}n_{ij}^\zeta t_{ij}^y - k_T\xi_{N,ij}^{1/2}\delta_{\zeta y}\right] + n_{ij}^y\left[\frac{1}{2}k_T\xi_{N,ij}^{-1/2}\xi_{T,ij}n_{ij}^\zeta t_{ij}^x - k_T\xi_{N,ij}^{1/2}\delta_{\zeta x}\right],
\end{aligned} \tag{B.23}$$

$$\begin{aligned}
\partial_{\ell_i}\tilde{T}_{ij} &= -n_{ij}^x\partial_{\ell_i}f_{T,ij}^y + n_{ij}^y\partial_{\ell_i}f_{T,ij}^x \\
&= -n_{ij}^x k_T\xi_{N,ij}^{1/2}n_{ij}^x - n_{ij}^y k_T\xi_{N,ij}^{1/2}n_{ij}^y \\
&= -k_T\xi_{N,ij}^{1/2},
\end{aligned} \tag{B.24}$$

where we have used $\sum_\zeta f_{T,ij}^\zeta n_{ij}^\zeta = 0$.

The terms proportional to $\xi_{T,ij}$ in the Jacobian include the history-dependent tangential displacements which are ignored in the effective potential (see Appendix E) [104–106]. The reason we use the Jacobian is to include the history-dependent tangential displacements in the dynamical matrix.

B.2 Explicit Jacobian expressions

In this section, we have written down the explicit results of $\mathcal{J}_N$ and $\mathcal{J}_T$. From the results for the derivative of $\tilde{F}_i^\alpha$, the non-diagonal block elements $\mathcal{J}_{N,ij}^{\alpha\beta}, \mathcal{J}_{T,ij}^{\alpha\beta}(i \neq$

j) are given by

$$\mathcal{J}^{xx}_{N,ij} = k_N \frac{\xi^{3/2}_{N,ij}}{r_{ij}} - k_N \left[\frac{3}{2} + \frac{\xi_{N,ij}}{r_{ij}}\right] \xi^{1/2}_{N,ij} (n^x_{ij})^2, \tag{B.25}$$

$$\mathcal{J}^{xx}_{T,ij} - k_T \xi^{1/2}_{N,ij} (n^y_{ij})^2 + \frac{1}{2} k_T \xi^{-1/2}_{N,ij} \xi_{T,ij} n^x_{ij} t^x_{ij}, \tag{B.26}$$

$$\mathcal{J}^{xy}_{N,ij} = -k_N \left[\frac{3}{2} + \frac{\xi_{N,ij}}{r_{ij}}\right] \xi^{1/2}_{N,ij} n^x_{ij} n^y_{ij}, \tag{B.27}$$

$$\mathcal{J}^{xy}_{T,ij} = k_T \xi^{1/2}_{N,ij} n^x_{ij} n^y_{ij} + \frac{1}{2} k_T \xi^{-1/2}_{N,ij} \xi_{T,ij} n^x_{ij} t^y_{ij}, \tag{B.28}$$

$$\mathcal{J}^{x\ell}_{N,ij} = 0, \tag{B.29}$$

$$\mathcal{J}^{x\ell}_{T,ij} = k_T \xi^{1/2}_{N,ij} n^y_{ij} + \frac{1}{2} k_T \xi^{-1/2}_{N,ij} \xi_{T,ij} n^x_{ij} (n^x_{ij} t^y_{ij} - n^y_{ij} t^x_{ij}), \tag{B.30}$$

$$\mathcal{J}^{yx}_{N,ij} = -k_N \left[\frac{3}{2} + \frac{\xi_{N,ij}}{r_{ij}}\right] \xi^{1/2}_{N,ij} n^x_{ij} n^y_{ij}, \tag{B.31}$$

$$\mathcal{J}^{yx}_{T,ij} = k_T \xi^{1/2}_{N,ij} n^x_{ij} n^y_{ij} + \frac{1}{2} k_T \xi^{-1/2}_{N,ij} \xi_{T,ij} n^y_{ij} t^x_{ij}, \tag{B.32}$$

$$\mathcal{J}^{yy}_{N,ij} = k_N \frac{\xi^{3/2}_{N,ij}}{r_{ij}} - k_N \left[\frac{3}{2} + \frac{\xi_{N,ij}}{r_{ij}}\right] \xi^{1/2}_{N,ij} (n^y_{ij})^2, \tag{B.33}$$

$$\mathcal{J}^{yy}_{T,ij} = -k_T \xi^{1/2}_{N,ij} (n^x_{ij})^2 + \frac{1}{2} k_T \xi^{-1/2}_{N,ij} \xi_{T,ij} n^y_{ij} t^y_{ij}, \tag{B.34}$$

$$\mathcal{J}^{y\ell}_{N,ij} = 0, \tag{B.35}$$

$$\mathcal{J}^{y\ell}_{T,ij} = -k_T \xi^{1/2}_{N,ij} n^x_{ij} + \frac{1}{2} k_T \xi^{-1/2}_{N,ij} \xi_{T,ij} n^y_{ij} (n^x_{ij} t^y_{ij} - n^y_{ij} t^x_{ij}), \tag{B.36}$$

$$\mathcal{J}^{\ell x}_{N,ij} = 0, \tag{B.37}$$

$$\mathcal{J}^{\ell x}_{T,ij} = -k_T \xi^{1/2}_{N,ij} n^y_{ij}, \tag{B.38}$$

$$\mathcal{J}^{\ell y}_{N,ij} = 0, \tag{B.39}$$

$$\mathcal{J}^{\ell y}_{T,ij} = k_T \xi^{1/2}_{N,ij} n^x_{ij}, \tag{B.40}$$

$$\mathcal{J}^{\ell\ell}_{N,ij} = 0, \tag{B.41}$$

$$\mathcal{J}^{\ell\ell}_{T,ij} = k_T \xi^{1/2}_{N,ij}. \tag{B.42}$$

Similarly, the diagonal block elements $\mathcal{J}_{N,ij}^{\alpha\beta}, \mathcal{J}_{T,ij}^{\alpha\beta}(i=j)$ are given by

$$\mathcal{J}_{N,ii}^{xx} = -\sum_{j\neq i}\left\{k_N\frac{\xi_{N,ij}^{3/2}}{r_{ij}} - k_N\left[\frac{3}{2}+\frac{\xi_{N,ij}}{r_{ij}}\right]\xi_{N,ij}^{1/2}(n_{ij}^x)^2\right\}, \tag{B.43}$$

$$\mathcal{J}_{T,ii}^{xx} = -\sum_{j\neq i}\left\{-k_T\xi_{N,ij}^{1/2}(n_{ij}^y)^2 + \frac{1}{2}k_T\xi_{N,ij}^{-1/2}\xi_{T,ij}n_{ij}^x t_{ij}^x\right\}, \tag{B.44}$$

$$\mathcal{J}_{N,ii}^{xy} = -\sum_{j\neq i}\left\{-k_N\left[\frac{3}{2}+\frac{\xi_{N,ij}}{r_{ij}}\right]\xi_{N,ij}^{1/2}n_{ij}^x n_{ij}^y\right\}, \tag{B.45}$$

$$\mathcal{J}_{T,ii}^{xy} = -\sum_{j\neq i}\left\{k_T\xi_{N,ij}^{1/2}n_{ij}^x n_{ij}^y + \frac{1}{2}k_T\xi_{N,ij}^{-1/2}\xi_{T,ij}n_{ij}^x t_{ij}^y\right\}, \tag{B.46}$$

$$\mathcal{J}_{N,ii}^{x\ell} = 0, \tag{B.47}$$

$$\mathcal{J}_{T,ii}^{x\ell} = \sum_{j\neq i}\left\{k_T\xi_{N,ij}^{1/2}n_{ij}^y + \frac{1}{2}\xi_{N,ij}^{-1/2}\xi_{T,ij}n_{ij}^x(n_{ij}^x t_{ij}^y - n_{ij}^y t_{ij}^x)\right\}, \tag{B.48}$$

$$\mathcal{J}_{N,ii}^{yx} = -\sum_{j\neq i}\left\{-k_N\left[\frac{3}{2}+\frac{\xi_{N,ij}}{r_{ij}}\right]\xi_{N,ij}^{1/2}n_{ij}^x n_{ij}^y\right\}, \tag{B.49}$$

$$\mathcal{J}_{T,ii}^{yx} = -\sum_{j\neq i}\left\{k_T\xi_{N,ij}^{1/2}n_{ij}^x n_{ij}^y + \frac{1}{2}k_T\xi_{N,ij}^{-1/2}\xi_{T,ij}n_{ij}^y t_{ij}^x\right\}, \tag{B.50}$$

$$\mathcal{J}_{N,ii}^{yy} = -\sum_{j\neq i}\left\{k_N\frac{\xi_{N,ij}^{3/2}}{r_{ij}} - k_N\left[\frac{3}{2}+\frac{\xi_{N,ij}}{r_{ij}}\right]\xi_{N,ij}^{1/2}(n_{ij}^y)^2\right\}, \tag{B.51}$$

$$\mathcal{J}_{T,ii}^{yy} = -\sum_{j\neq i}\left\{-k_T\xi_{N,ij}^{1/2}(n_{ij}^x)^2 + \frac{1}{2}k_T\xi_{N,ij}^{-1/2}\xi_{T,ij}n_{ij}^y t_{ij}^y\right\}, \tag{B.52}$$

$$\mathcal{J}_{N,ii}^{yy} = 0, \tag{B.53}$$

$$\mathcal{J}_{T,ii}^{y\ell} = -\sum_{j\neq i}\left\{k_T\xi_{N,ij}^{1/2}n_{ij}^x + \frac{1}{2}k_T\xi_{N,ij}^{-1/2}\xi_{T,ij}n_{ij}^y(n_{ij}^x t_{ij}^y - n_{ij}^y t_{ij}^x)\right\}, \tag{B.54}$$

$$\mathcal{J}_{N,ii}^{\ell x} = 0, \tag{B.55}$$

$$\mathcal{J}_{T,ii}^{\ell x} = \sum_{j\neq i}k_T\xi_{N,ij}^{1/2}n_{ij}^y, \tag{B.56}$$

$$\mathcal{J}_{N,ii}^{\ell y} = 0, \tag{B.57}$$

$$\mathcal{J}_{T,ii}^{\ell y} = -\sum_{j\neq i}k_T\xi_{N,ij}^{1/2}n_{ij}^x, \tag{B.58}$$

$$\mathcal{J}_{N,ii}^{\ell\ell} = 0, \tag{B.59}$$

$$\mathcal{J}_{T,ii}^{\ell\ell} = \sum_{j\neq i}k_T\xi_{N,ij}^{1/2}. \tag{B.60}$$

Note that the terms proportional to $\xi_{T,ij}$ in $\mathcal{J}_T$ include the history-dependent tangential displacements which are ignored in the effective potential [104–106].

Appendix C

The detailed derivation of G in the Jacobian analysis

In this appendix, we derive Eq. (3.40) that gives the rigidity. First, nonaffine displacements are expanded in terms of eigenfunctions of the Jacobian. Next, we express the rigidity as the eigenvalues and eigenfunctions of the Jacobian. Note that we adopt the abbreviation $dA(\boldsymbol{q}^{\rm FB}(0))/d\gamma := dA(\boldsymbol{q}(\gamma))/d\gamma|_{\boldsymbol{q}(\gamma)=\boldsymbol{q}^{\rm FB}(0)}$ in this appendix.

C.1 Expansion for nonaffine displacements via eigenfunction of Jacobian

At FB state, $\tilde{F}_i^\alpha/d\gamma$ is expressed as

$$\begin{aligned}\frac{d\tilde{F}_i^\alpha}{d\gamma} &= \lim_{\Delta\gamma\to 0}\frac{\tilde{F}_i^\alpha(\boldsymbol{q}^{\rm FB}(\Delta\gamma)) - \tilde{F}_i^\alpha(\boldsymbol{q}^{\rm FB}(0))}{\Delta\gamma} \\ &= \sum_{j\neq i}\left[\frac{\partial f_{ij}^\alpha}{\partial q_i^x}y_{ij}(\boldsymbol{q}^{\rm FB}(0)) + \sum_{\zeta=x,y}\frac{\partial f_{ij}^\alpha}{\partial r_i^\zeta}\frac{d\mathring{r}_{ij}^\zeta(\boldsymbol{q}^{\rm FB}(0))}{d\gamma} + \frac{\partial f_{ij}^\alpha}{\partial \ell_i}\left(\frac{d\mathring{\ell}_i(\boldsymbol{q}^{\rm FB}(0))}{d\gamma} + \frac{d\mathring{\ell}_j(\boldsymbol{q}^{\rm FB}(0))}{d\gamma}\right)\right].\end{aligned} \tag{C.1}$$

Using the Jacobian, we rewrite Eq. (C.1) as

$$\frac{d\tilde{F}_i^\alpha}{d\gamma} = -\sum_{j\neq i}\left[\mathcal{J}_{ji}^{\alpha x}y_{ij}(\boldsymbol{q}^{\rm FB}(0)) + \sum_{\zeta=x,y}\mathcal{J}_{ji}^{\alpha\zeta}\frac{d\mathring{r}_{ij}^\zeta(\boldsymbol{q}^{\rm FB}(0))}{d\gamma} + \mathcal{J}_{ji}^{\alpha\ell}\left(\frac{d\mathring{\ell}_i(\boldsymbol{q}^{\rm FB}(0))}{d\gamma} + \frac{d\mathring{\ell}_j(\boldsymbol{q}^{\rm FB}(0))}{d\gamma}\right)\right], \tag{C.2}$$

where the first and second terms on the RHS represent the contributions from the affine and nonaffine displacements, respectively. Since the affine displacements are applied to our system instantaneously as a step strain, the integral interval of tangential displacements during the affine deformation are zero. Thus,

only the normal contributions in the first term on RHS of Eq. (C.2) survive in the affine displacements. Then, we rewrite $\mathcal{J}_{ij}^{\alpha\beta}$ as $\mathcal{J}_{N,ij}^{\alpha\beta}$ in Eq. (C.2):

$$\frac{d\tilde{F}_i^\alpha}{d\gamma} = -\sum_{j\neq i}\left[\mathcal{J}_{N,ji}^{\alpha x} y_{ij}(\boldsymbol{q}^{\rm FB}(0)) + \sum_{\zeta=x,y}\mathcal{J}_{ji}^{\alpha\zeta}\frac{d\mathring{r}_{ij}^{\zeta}(\boldsymbol{q}^{\rm FB}(0))}{d\gamma} + \mathcal{J}_{ji}^{\alpha\ell}\left(\frac{d\mathring{\ell}_i(\boldsymbol{q}^{\rm FB}(0))}{d\gamma} + \frac{d\mathring{\ell}_j(\boldsymbol{q}^{\rm FB}(0))}{d\gamma}\right)\right]. \tag{C.3}$$

Introducing

$$|\Xi_i\rangle := \begin{bmatrix} \sum_{j\neq i}\mathcal{J}_{N,ji}^{xx} y_{ij} \\ \sum_{j\neq i}\mathcal{J}_{N,ji}^{xy} y_{ij} \\ \sum_{j\neq i}\mathcal{J}_{N,ji}^{x\ell} y_{ij} \end{bmatrix} \tag{C.4}$$

and with the aid of $d\tilde{F}_i^\alpha/d\gamma = 0$ at the FB state in Eq. (C.3), we obtain

$$\Xi_i^\alpha = -\sum_{j\neq i}\left[\sum_{\zeta=x,y}\mathcal{J}_{ji}^{\alpha\zeta}\frac{d\mathring{r}_{ij}^{\zeta}}{d\gamma} + \mathcal{J}_{ji}^{\alpha\ell}\left(\frac{d\mathring{\ell}_i}{d\gamma} + \frac{d\mathring{\ell}_j}{d\gamma}\right)\right]. \tag{C.5}$$

Since $\mathcal{J}$ satisfies $\mathcal{J}_{ii}^{\kappa\beta} = -\sum_{j\neq i}\mathcal{J}_{ji}^{\kappa\beta}$, we obtain

$$\begin{aligned}
\Xi_i^\kappa &= -\sum_{\zeta=x,y}\left[\left(\sum_{j\neq i}\mathcal{J}_{ji}^{\kappa\zeta}\right)\frac{d\mathring{r}_i^\zeta}{d\gamma} - \sum_{j\neq i}\mathcal{J}_{ji}^{\kappa\zeta}\frac{d\mathring{r}_j^\zeta}{d\gamma}\right] - \left[\left(\sum_{j\neq i}\mathcal{J}_{ji}^{\kappa\ell}\right)\frac{d\mathring{\ell}_i}{d\gamma} + \sum_{j\neq i}\mathcal{J}_{ji}^{\kappa\ell}\frac{d\mathring{\ell}_j}{d\gamma}\right] \\
&= -\sum_{\zeta=x,y}\left[-\mathcal{J}_{ii}^{\kappa\zeta}\frac{d\mathring{r}_i^\zeta}{d\gamma} - \sum_{j\neq i}\mathcal{J}_{ji}^{\kappa\zeta}\frac{d\mathring{r}_j^\zeta}{d\gamma}\right] - \left[-\mathcal{J}_{ii}^{\kappa\ell}\frac{d\mathring{\ell}_i}{d\gamma} + \sum_{j\neq i}\mathcal{J}_{ji}^{\kappa\ell}\frac{d\mathring{\ell}_j}{d\gamma}\right] \\
&= \sum_{\zeta=x,y}\sum_{j=1}^{N}\mathcal{J}_{ji}^{\kappa\zeta}\frac{d\mathring{r}_j^\zeta}{d\gamma} + \mathcal{J}_{ii}^{\kappa\ell}\frac{d\mathring{\ell}_i}{d\gamma} - \sum_{j\neq i}\mathcal{J}_{ji}^{\kappa\ell}\frac{d\mathring{\ell}_j}{d\gamma}.
\end{aligned} \tag{C.6}$$

Since $\mathcal{J}$ satisfies $\mathcal{J}_{ii}^{\ell\beta} = \sum_{j\neq i}\mathcal{J}_{ji}^{\ell\beta}$, we obtain

$$\begin{aligned}
\Xi_i^\ell &= -\sum_{\zeta=x,y}\left[\left(\sum_{j\neq i}\mathcal{J}_{ji}^{\ell\zeta}\right)\frac{d\mathring{r}_i^\zeta}{d\gamma} - \sum_{j\neq i}\mathcal{J}_{ji}^{\ell\zeta}\frac{d\mathring{r}_j^\zeta}{d\gamma}\right] - \left[\left(\sum_{j\neq i}\mathcal{J}_{ji}^{\ell\ell}\right)\frac{d\mathring{\ell}_i}{d\gamma} + \sum_{j\neq i}\mathcal{J}_{ji}^{\ell\ell}\frac{d\mathring{\ell}_j}{d\gamma}\right] \\
&= -\sum_{\zeta=x,y}\left[\mathcal{J}_{ii}^{\ell\zeta}\frac{d\mathring{r}_i^\zeta}{d\gamma} - \sum_{j\neq i}\mathcal{J}_{ji}^{\ell\zeta}\frac{d\mathring{r}_j^\zeta}{d\gamma}\right] + \left[\mathcal{J}_{ii}^{\ell\ell}\frac{d\mathring{\ell}_i}{d\gamma} + \sum_{j\neq i}\mathcal{J}_{ji}^{\ell\ell}\frac{d\mathring{\ell}_j}{d\gamma}\right] \\
&= -\sum_{\zeta=x,y}\left[\mathcal{J}_{ii}^{\ell\zeta}\frac{d\mathring{r}_i^\zeta}{d\gamma} - \sum_{j\neq i}\mathcal{J}_{ji}^{\ell\zeta}\frac{d\mathring{r}_j^\zeta}{d\gamma}\right] + \sum_{j=1}^{N}\mathcal{J}_{ji}^{\ell\ell}\frac{d\mathring{\ell}_j}{d\gamma}.
\end{aligned} \tag{C.7}$$

Let us introduce $\tilde{\mathcal{J}}_{ii}^{\alpha\beta}$ as

$$\tilde{\mathcal{J}}_{ii}^{\alpha\beta} := \begin{cases} -\mathcal{J}_{ii}^{\ell x} & (\alpha=\ell,\ \beta=x) \\ -\mathcal{J}_{ii}^{\ell y} & (\alpha=\ell,\ \beta=y) \\ \mathcal{J}_{ii}^{\alpha\beta} & (\text{otherwise}) \end{cases} \tag{C.8}$$

and

$$\tilde{\mathcal{J}}_{ij}^{\alpha\beta} := \mathcal{J}_{ij}^{\alpha\beta}. \tag{C.9}$$

Here, $\tilde{\mathcal{J}}_{ij}$ satisfies

$$\tilde{\mathcal{J}}_{ji}^{\alpha\beta} = \begin{cases} -\mathcal{J}_{ij}^{x\ell} & (\alpha = x,\ \beta = \ell) \\ -\mathcal{J}_{ij}^{y\ell} & (\alpha = y,\ \beta = \ell) \\ \mathcal{J}_{ij}^{\alpha\beta} & (\text{otherwise}). \end{cases} \tag{C.10}$$

With the aid of $\tilde{\mathcal{J}}$ Eqs. (C.6) and (C.7) are rewritten as

$$\begin{aligned} \Xi_i^{\alpha} &= \sum_{\zeta=x,y} \sum_{j=1}^{N} \tilde{\mathcal{J}}_{ij}^{\alpha\zeta} \frac{d\mathring{r}_j^{\zeta}}{d\gamma} + \tilde{\mathcal{J}}_{ii}^{\alpha\ell} \frac{d\mathring{\ell}_i}{d\gamma} + \sum_{j\neq i} \tilde{\mathcal{J}}_{ij}^{\alpha\ell} \frac{d\mathring{\ell}_j}{d\gamma} \\ &= \sum_{\zeta=x,y} \sum_{j=1}^{N} \tilde{\mathcal{J}}_{ij}^{\alpha\zeta} \frac{d\mathring{r}_j^{\zeta}}{d\gamma} + \sum_{j=1}^{N} \tilde{\mathcal{J}}_{ij}^{\alpha\ell} \frac{d\mathring{\ell}_j}{d\gamma} \\ &= \sum_{\beta=x,y,\ell} \sum_{j=1}^{N} \tilde{\mathcal{J}}_{ij}^{\alpha\beta} \frac{d\mathring{q}_j^{\beta}}{d\gamma}, \end{aligned} \tag{C.11}$$

$$\begin{aligned} \Xi_i^{\ell} &= \sum_{\zeta=x,y} \left[\mathcal{J}_{ii}^{\ell\zeta} \frac{d\mathring{r}_i^{\zeta}}{d\gamma} + \sum_{j\neq i} \mathcal{J}_{ij}^{\ell\zeta} \frac{d\mathring{r}_j^{\zeta}}{d\gamma} \right] + \sum_{j=1}^{N} \mathcal{J}_{ji}^{\ell\ell} \frac{d\mathring{\ell}_j}{d\gamma} \\ &= \sum_{\zeta=x,y} \sum_{j=1}^{N} \mathcal{J}_{ij}^{\ell\zeta} \frac{d\mathring{r}_j^{\zeta}}{d\gamma} + \sum_{j=1}^{N} \mathcal{J}_{ji}^{\ell\ell} \frac{d\mathring{\ell}_j}{d\gamma} \\ &= \sum_{\beta=x,y,\ell} \sum_{j=1}^{N} \mathcal{J}_{ij}^{\ell\beta} \frac{d\mathring{q}_j^{\beta}}{d\gamma}. \end{aligned} \tag{C.12}$$

Equations (C.11) and (C.12) can be rewritten as

$$\Xi_i^{\alpha} = \sum_{j=1}^{N} \sum_{\beta=x,y,\ell} \tilde{\mathcal{J}}_{ij}^{\alpha\beta} \frac{d\mathring{q}_j^{\beta}}{d\gamma}. \tag{C.13}$$

Furthermore, Eq. (C.13) can be expressed as

$$|\Xi\rangle = \tilde{\mathcal{J}} \left| \frac{d\mathring{q}}{d\gamma} \right\rangle, \tag{C.14}$$

which corresponds to Eq. (3.36) in Sec. 4.3.2, where $|d\mathring{q}/d\gamma\rangle$ is introduced in Eq. (3.35).

Let us expand $|d\mathring{q}/d\gamma\rangle$ by the right eigenfunction $|\tilde{R}_n\rangle$ of $\tilde{\mathcal{J}}$ as

$$\left| \frac{d\mathring{q}}{d\gamma} \right\rangle = a_n \left| \tilde{R}_n \right\rangle. \tag{C.15}$$

Substituting Eq. (C.15) into Eq. (C.14), we obtain

$$|\Xi\rangle = \tilde{\lambda}_n a_n |\tilde{R}_n\rangle . \tag{C.16}$$

Multiplying $\langle \tilde{L}_m|$ to Eq. (C.16) with the aid of the orthonormal relation, we obtain

$$\begin{aligned} \left\langle \tilde{L}_m \middle| \Xi \right\rangle &= \tilde{\lambda}_n a_n \left\langle \tilde{L}_m \middle| \tilde{R}_n \right\rangle \\ &= \tilde{\lambda}_m a_m. \end{aligned} \tag{C.17}$$

Substituting this into Eq. (C.15), we obtain Eq. (3.40).

C.2 The expression of G

Let us evaluate the rigidity G defined as Eq. (3.19). Substituting Eqs. (3.16) and (3.17) into Eq. (3.19), we obtain

$$G = -\left\langle \lim_{\Delta\gamma\to 0} \frac{1}{2\Delta\gamma L^2} \sum_{i,j(i\neq j)} \left[f_{ij}^x(\boldsymbol{q}^{\mathrm{FB}}(\Delta\gamma)) r_{ij}^y(\boldsymbol{q}^{\mathrm{FB}}(\Delta\gamma)) - f_{ij}^x(\boldsymbol{q}^{\mathrm{FB}}(0)) r_{ij}^y(\boldsymbol{q}^{\mathrm{FB}}(0)) \right] \right\rangle, \tag{C.18}$$

where we have adopted the symmetric expression for i and j in the summation in Eq. (C.18).

Expanding $r_{ij}^\alpha(\boldsymbol{q}^{\mathrm{FB}}(\Delta\gamma))$ in Eq. (C.18) by $\Delta\gamma$ from the zero strain state, we obtain

$$\begin{aligned} r_{ij}^\alpha(\boldsymbol{q}^{\mathrm{FB}}(\Delta\gamma)) &= r_i^\alpha(\boldsymbol{q}^{\mathrm{FB}}(\Delta\gamma)) - r_j^\alpha(\boldsymbol{q}^{\mathrm{FB}}(\Delta\gamma)) \\ &\simeq r_{ij}^\alpha(\boldsymbol{q}^{\mathrm{FB}}(0)) + \Delta\gamma \left\{ \delta_{\alpha x} \left(y_i(\boldsymbol{q}^{\mathrm{FB}}(0)) - y_j(\boldsymbol{q}^{\mathrm{FB}}(0)) \right) + \frac{d\mathring{r}_i^\alpha(\boldsymbol{q}^{\mathrm{FB}}(0))}{d\gamma} - \frac{d\mathring{r}_j^\alpha(\boldsymbol{q}^{\mathrm{FB}}(0))}{d\gamma} \right\} \\ &= r_{ij}^\alpha(\boldsymbol{q}^{\mathrm{FB}}(0)) + \Delta\gamma \left\{ \delta_{\alpha x} y_{ij}(\boldsymbol{q}^{\mathrm{FB}}(0)) + \frac{d\mathring{r}_{ij}^\alpha(\boldsymbol{q}^{\mathrm{FB}}(0))}{d\gamma} \right\}. \end{aligned} \tag{C.19}$$

Similarly, expanding $f_{ij}^\alpha(\Delta\gamma)$ in Eq. (C.18) from the zero strain state, we obtain

$$\begin{aligned} f_{ij}^\alpha(\boldsymbol{q}^{\mathrm{FB}}(\Delta\gamma)) &\simeq f_{ij}^\alpha(\boldsymbol{q}^{\mathrm{FB}}(0)) + \sum_{k=1}^N \sum_{\zeta=x,y} \Delta\gamma \frac{\partial f_{ij}^\alpha}{\partial r_k^\zeta} \frac{dr_k^\zeta}{d\gamma} + \sum_{k=1}^N \Delta\gamma \frac{\partial f_{ij}^\alpha}{\partial \ell_k} \frac{d\ell_k}{d\gamma} \\ &= f_{ij}^\alpha(\boldsymbol{q}^{\mathrm{FB}}(0)) + \sum_{\zeta=x,y} \Delta\gamma \left[\frac{\partial f_{ij}^\alpha}{\partial r_i^\zeta} \left(\delta_{\zeta x} y_i(\boldsymbol{q}^{\mathrm{FB}}(0)) + \frac{d\mathring{r}_i^\zeta(\boldsymbol{q}^{\mathrm{FB}}(0))}{d\gamma} \right) \right. \\ &\quad \left. + \frac{\partial f_{ij}^\alpha}{\partial r_j^\zeta} \left(\delta_{\zeta x} y_j(\boldsymbol{q}^{\mathrm{FB}}(0)) + \frac{d\mathring{r}_j^\zeta(\boldsymbol{q}^{\mathrm{FB}}(0))}{d\gamma} \right) \right] \\ &\quad + \Delta\gamma \left[\frac{\partial f_{ij}^\alpha}{\partial \ell_i} \left(\delta_{\ell x} y_i(\boldsymbol{q}^{\mathrm{FB}}(0)) + \frac{d\mathring{\ell}_i(\boldsymbol{q}^{\mathrm{FB}}(0))}{d\gamma} \right) + \frac{\partial f_{ij}^\alpha}{\partial \ell_j} \left(\delta_{\ell x} y_j(\boldsymbol{q}^{\mathrm{FB}}(0)) + \frac{d\mathring{\ell}_j(\boldsymbol{q}^{\mathrm{FB}}(0))}{d\gamma} \right) \right]. \end{aligned} \tag{C.20}$$

Furthermore, using $\partial f_{ij}^{\alpha}/\partial r_j^{\zeta} = -\partial f_{ij}^{\alpha}/\partial r_i^{\zeta}$ and $\partial f_{ij}^{\alpha}/\partial \ell_j = \partial f_{ij}^{\alpha}/\partial \ell_i$, f_{ij}^{α} can be written as

$$\begin{aligned} f_{ij}^{\alpha}(\boldsymbol{q}^{\mathrm{FB}}(\Delta\gamma)) = f_{ij}^{\alpha}(\boldsymbol{q}^{\mathrm{FB}}(0)) \\ + \sum_{\zeta=x,y} \Delta\gamma \frac{\partial f_{ij}^{\alpha}}{\partial r_i^{\zeta}} \left(\delta_{\zeta x} y_{ij}(\boldsymbol{q}^{\mathrm{FB}}(0)) + \frac{d\mathring{r}_{ij}^{\zeta}(\boldsymbol{q}^{\mathrm{FB}}(0))}{d\gamma} \right) \\ + \Delta\gamma \frac{\partial f_{ij}^{\alpha}}{\partial \ell_i} \left(\frac{d\mathring{\ell}_i(\boldsymbol{q}^{\mathrm{FB}}(0))}{d\gamma} + \frac{d\mathring{\ell}_j(\boldsymbol{q}^{\mathrm{FB}}(0))}{d\gamma} \right). \end{aligned} \tag{C.21}$$

Substituting Eqs. (C.19) and (C.21) into Eq. (C.18), we obtain

$$\begin{aligned} G = -\frac{1}{2L^2} \Bigg\langle \sum_{i,j(i\neq j)} \Bigg[f_{ij}^{x}(\boldsymbol{q}^{\mathrm{FB}}(0)) \frac{d\mathring{q}_{ij}^{x}(\boldsymbol{q}^{\mathrm{FB}}(0))}{d\gamma} \\ + \sum_{\zeta=x,y} \frac{\partial f_{ij}^{x}(\boldsymbol{q}^{\mathrm{FB}}(0))}{\partial r_i^{\zeta}} r_{ij}^{y}(\boldsymbol{q}^{\mathrm{FB}}(0)) \left(\delta_{\zeta x} y_{ij}(\boldsymbol{q}^{\mathrm{FB}}(0)) + \frac{d\mathring{r}_{ij}^{\zeta}(\boldsymbol{q}^{\mathrm{FB}}(0))}{d\gamma} \right) \\ + \frac{\partial f_{ij}^{x}(\boldsymbol{q}^{\mathrm{FB}}(0))}{\partial \ell_i} r_{ij}^{y}(\boldsymbol{q}^{\mathrm{FB}}(0)) \left(\frac{d\mathring{\ell}_i(\boldsymbol{q}^{\mathrm{FB}}(0))}{d\gamma} + \frac{d\mathring{\ell}_j(\boldsymbol{q}^{\mathrm{FB}}(0))}{d\gamma} \right) \Bigg] \Bigg\rangle. \end{aligned} \tag{C.22}$$

Because $\sum_{i(i\neq j)} f_{ij}^{\alpha}(\boldsymbol{q}^{\mathrm{FB}}(0)) = 0$ at the FB state, the first term on RHS of Eq. (C.22) can be written as

$$\begin{aligned} \sum_{i,j(i\neq j)} f_{ij}^{x}(\boldsymbol{q}^{\mathrm{FB}}(0)) \frac{d\mathring{q}_{ij}^{x}(\boldsymbol{q}^{\mathrm{FB}}(0))}{d\gamma} &= \sum_{i,j(i\neq j)} f_{ij}^{x}(\boldsymbol{q}^{\mathrm{FB}}(0)) \left(\frac{d\mathring{q}_{i}^{x}(\boldsymbol{q}^{\mathrm{FB}}(0))}{d\gamma} - \frac{d\mathring{q}_{j}^{x}(\boldsymbol{q}^{\mathrm{FB}}(0))}{d\gamma} \right) \\ &= \sum_{j} \left(\sum_{j(j\neq i)} f_{ij}^{x}(\boldsymbol{q}^{\mathrm{FB}}(0)) \right) \frac{d\mathring{q}_{i}^{x}(\boldsymbol{q}^{\mathrm{FB}}(0))}{d\gamma} \\ &\quad - \sum_{i} \left(\sum_{i(i\neq j)} f_{ij}^{x}(\boldsymbol{q}^{\mathrm{FB}}(0)) \right) \frac{d\mathring{q}_{j}^{x}(\boldsymbol{q}^{\mathrm{FB}}(0))}{d\gamma} \\ &= 0. \end{aligned} \tag{C.23}$$

Thus, G is expressed as

$$\begin{aligned} G = -\frac{1}{2L^2} \Bigg\langle \sum_{i,j(i\neq j)} \Bigg[\sum_{\zeta=x,y} \frac{\partial f_{ij}^{x}(\boldsymbol{q}^{\mathrm{FB}}(0))}{\partial r_i^{\zeta}} y_{ij}(\boldsymbol{q}^{\mathrm{FB}}(0)) \left(\delta_{\zeta x} y_{ij}(\boldsymbol{q}^{\mathrm{FB}}(0)) + \frac{d\mathring{r}_{ij}^{\zeta}(\boldsymbol{q}^{\mathrm{FB}}(0))}{d\gamma} \right) \\ + \frac{\partial f_{ij}^{x}(\boldsymbol{q}^{\mathrm{FB}}(0))}{\partial \ell_i} y_{ij}(\boldsymbol{q}^{\mathrm{FB}}(0)) \left(\frac{d\mathring{\ell}_i(\boldsymbol{q}^{\mathrm{FB}}(0))}{d\gamma} + \frac{d\mathring{\ell}_j(\boldsymbol{q}^{\mathrm{FB}}(0))}{d\gamma} \right) \Bigg] \Bigg\rangle. \end{aligned} \tag{C.24}$$

With the aid of $\mathcal{J}_{ij}^{\alpha\beta} := -\partial_{q_j^\beta} f_{ij}^\alpha$ $(i \neq j)$, we can express G as

$$
\begin{aligned}
G = \frac{1}{2L^2} \Bigg\langle \sum_{i,j(i\neq j)} \Bigg[& \sum_{\zeta=x,y} y_{ij}(\boldsymbol{q}^{\mathrm{FB}}(0)) \mathcal{J}_{ji}^{x\zeta}(\boldsymbol{q}^{\mathrm{FB}}(0)) \left(\delta_{\zeta x} y_{ij}(\boldsymbol{q}^{\mathrm{FB}}(0)) + \frac{d\mathring{r}_{ij}^{\zeta}(\boldsymbol{q}^{\mathrm{FB}}(0))}{d\gamma} \right) \\
& + y_{ij}(\boldsymbol{q}^{\mathrm{FB}}(0)) \mathcal{J}_{ji}^{x\ell}(\boldsymbol{q}^{\mathrm{FB}}(0)) \left(\frac{d\mathring{\ell}_i(\boldsymbol{q}^{\mathrm{FB}}(0))}{d\gamma} + \frac{d\mathring{\ell}_j(\boldsymbol{q}^{\mathrm{FB}}(0))}{d\gamma} \right) \Bigg] \Bigg\rangle \\
= \frac{1}{2L^2} \Bigg\langle \sum_{i,j(i\neq j)} \Bigg[& y_{ij}^2(\boldsymbol{q}^{\mathrm{FB}}(0)) \mathcal{J}_{ji}^{xx}(\boldsymbol{q}^{\mathrm{FB}}(0)) + \sum_{\zeta=x,y} y_{ij}(\boldsymbol{q}^{\mathrm{FB}}(0)) \mathcal{J}_{ji}^{x\zeta}(\boldsymbol{q}^{\mathrm{FB}}(0)) \frac{d\mathring{r}_{ij}^{\zeta}(\boldsymbol{q}^{\mathrm{FB}}(0))}{d\gamma} \\
& + y_{ij}(\boldsymbol{q}^{\mathrm{FB}}(0)) \mathcal{J}_{ji}^{x\ell}(\boldsymbol{q}^{\mathrm{FB}}(0)) \left(\frac{d\mathring{\ell}_i(\boldsymbol{q}^{\mathrm{FB}}(0))}{d\gamma} + \frac{d\mathring{\ell}_j(\boldsymbol{q}^{\mathrm{FB}}(0))}{d\gamma} \right) \Bigg] \Bigg\rangle .
\end{aligned}
\tag{C.25}
$$

Thus, with Eqs (3.38) and (3.39), we obtain Eqs. (3.41)–(3.43).

Appendix D

Effects of rattlers

In this appendix, we investigate the effects of rattlers. In the first section, we investigate the effects of rattlers for the DOS. In the second section, we clarify the contributions of rattlers by using the participation ratio.

D.1 Effects of rattlers on the DOS

In this section, we investigate the role of rattlers. We call grain i a rattler, if its coordination number Z_i is $Z_i \leq Z_{\rm Th}$. Since the coordination number of isostatic state is three, $Z_{\rm Th}$ can be 1 or 2 for frictional grains. The rattlers are determined by the following method. Given a grain configuration, we measure the coordination number $Z_i^{(n=1)}$ of each grain. Then, we regard N_1 grains satisfying $Z_i^{(n=1)} \leq Z_{\rm Th}$ as rattlers at the first trial. We measure the coordination number $Z_i^{(n=2)}$ after we remove the rattler grains. In the second trial, we regard grains satisfying $Z_i^{(n=2)} \leq Z_{\rm Th}$ as new rattlers. We repeat these processes until the number of rattlers is converged. As shown in Fig. D.1, at which we adopt $Z_{\rm Th} = 2$, low frequency modes in Region I and a doubling pair between Regions I and II are contributions from rattlers.

D.2 Participation ratio

In this section, to clarify whether the mode at ω_n is localized or spread to the whole system, we introduce a participation ratio p_n [96, 98]

$$p_n := \frac{\left(\sum_{i=1}^{N} |\boldsymbol{R}_{n,i}|^2\right)^2}{N \sum_{i=1}^{N} |\boldsymbol{R}_{n,i}|^4}. \tag{D.1}$$

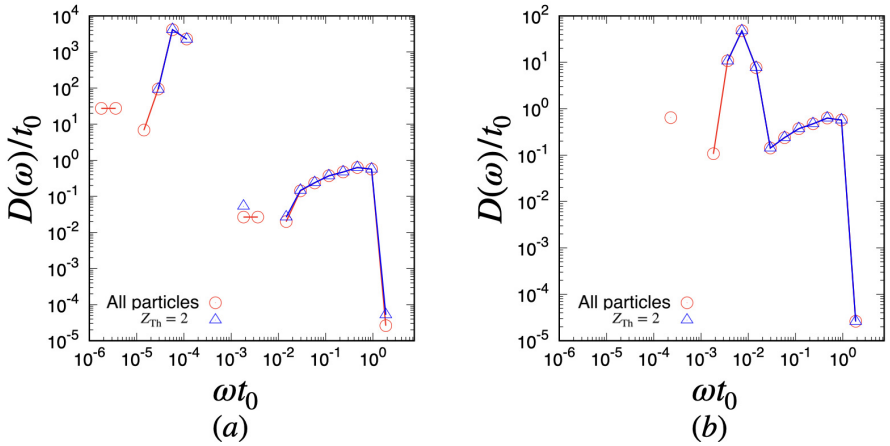

Figure D.1: Double logarithmic plots of $D(\omega)$ with (red circles) and without (blue triangles by using $Z_{\rm Th} = 2$) rattlers for $\phi = 0.90$ at (a) $k_T/k_N = 1.0\times10^{-8}$ and (b) $k_T/k_N = 1.0 \times 10^{-4}$. These figures are based on numerical results for $N = 1024$.

We plot $p(\omega)$ defined as

$$p(\omega) := \frac{\sum_{n=1}^{3N} \langle p_n \delta(\omega - \omega_n)\rangle}{\sum_{n=1}^{3N} \langle \delta(\omega - \omega_n)\rangle} \tag{D.2}$$

against ωt_0 for $\phi = 0.90$ in Fig. D.2. Note that $p(\omega)$ are set to be zero if there is no right eigenvalue in the region $(\omega^{(s)} < \omega < \omega^{(s+1)})$. Figure D.2 shows that the modes $\omega t_0 \approx 10^{-6}$ and $\omega t_0 \approx 10^{-3}$ in Fig. D.2 (a) and $\omega t_0 \approx 10^{-4}$ in Fig. D.2 (b) are nearly equal to $p \approx 1/N$. Recalling that those modes consist of the rattler, we conclude that the contribution of the rattler is localized. In the middle range of ω in Fig. D.2, there is an isolated band which shifts to the large ω as k_T/k_N increases with keeping its shape which can be seen in Sec. 3.4.1.

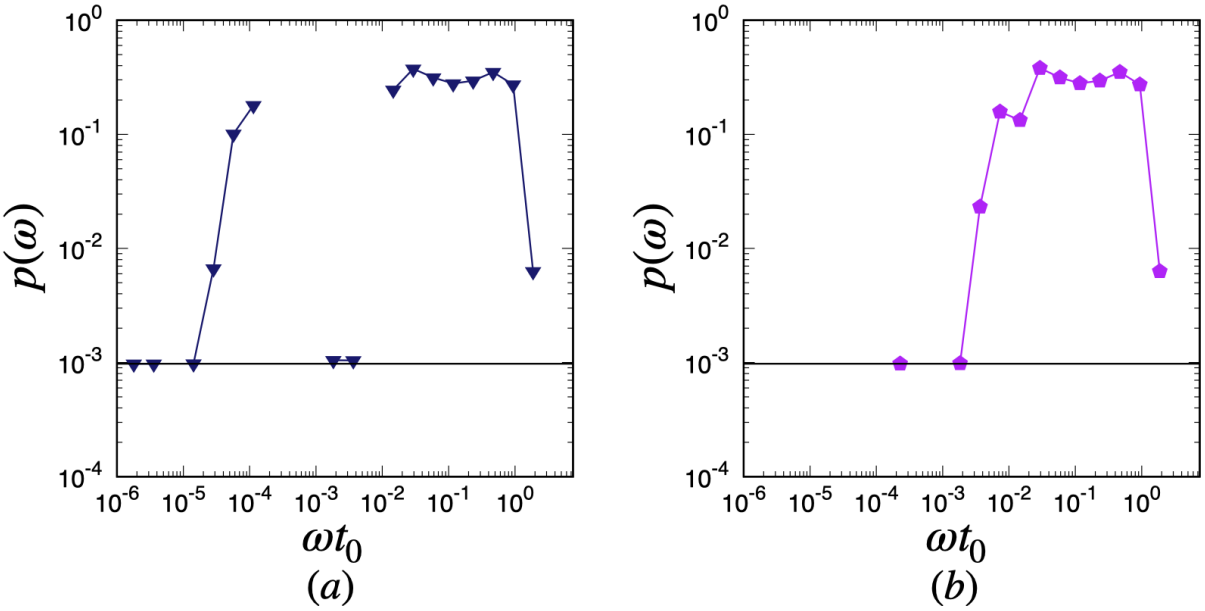

Figure D.2: Double logarithmic plots of $p(\omega)$ for $\phi = 0.90$ at (a) $k_T/k_N = 1.0 \times 10^{-8}$ and (b) $k_T/k_N = 1.0 \times 10^{-4}$, where the guide line is $1/N$. These figures are based on numerical results for $N = 1024$.

Appendix E

DOS in terms of the effective Hessian

In this appendix, we introduce the DOS with the aid of the effective Hessian as in Refs. [104–106]. The effective Hessian $\mathcal{H}$ at the FB state is defined as

$$\mathcal{H}_{ij}^{\alpha\beta} := \left.\frac{\partial^2 U_{\rm eff}}{\partial q_i^\alpha \partial q_j^\beta}\right|_{\boldsymbol{q}(\gamma)=\boldsymbol{q}^{\rm FB}(0)}, \tag{E.1}$$

where $U_{\rm eff}$ is the effective potential defined as

$$U_{\rm eff} := \frac{1}{2}\sum_{\langle ij\rangle}\left[k_N(\delta\boldsymbol{r}_{ij}\cdot\boldsymbol{n}_{ij})^2 - \frac{|\boldsymbol{f}_{N,ij}|}{r_{ij}^{\rm FB}}(\delta\boldsymbol{r}_{ij}\cdot\boldsymbol{t}_{ij})^2 + k_T\delta t_{ij}^2\right] \tag{E.2}$$

with $\delta\boldsymbol{r}_{ij} := \delta\boldsymbol{r}_i - \delta\boldsymbol{r}_j, \delta\boldsymbol{r}_i := \boldsymbol{r}_i - \boldsymbol{r}_i^{\rm FB}, r_{ij}^{\rm FB} := |\boldsymbol{r}_i^{\rm FB} - \boldsymbol{r}_j^{\rm FB}|, \delta t_{ij} := \delta\boldsymbol{r}_{ij}\cdot\boldsymbol{t}_{ij} - (\delta\ell_i + \delta\ell_j)$, and $\delta\ell_i := \ell_i - \ell_i^{\rm FB}$. Here, $\boldsymbol{r}_i^{\rm FB}$ and $\ell_i^{\rm FB}$ are the position of i-th grain and 3rd component of $\boldsymbol{q}_i$ at the FB state, respectively. Thus, $\mathcal{H}$ is a $3N\times 3N$ matrix corresponding to the Jacobian. We note that this Hessian matrix is a real symmetric matrix, and thus, it can be diagonalized by an orthogonal matrix, where the eigenvectors are orthogonal with each other, and the corresponding eigenvalues are real number.

The eigenvalue equation of $\mathcal{H}$ is expressed as

$$\mathcal{H}\,|n\rangle = \lambda_{H,n}\,|n\rangle\,, \tag{E.3}$$

where $\lambda_{H,n}$ and $|n\rangle$ are the n-th eigenvalue and eigenvector of $\mathcal{H}$, respectively. Note that the left eigenvalue is also given by $\langle n|\mathcal{H} = \lambda_{H,n}\langle n|$, where $\langle n| = |n\rangle^T$. Then, we introduce the DOS D_H in terms of $\mathcal{H}$ as

$$D_H(\omega) := \frac{1}{3N}\sum_{n=1}^{3N}\langle\delta(\omega-\omega_{H,n})\rangle, \tag{E.4}$$

where $\omega_{H,n} := \sqrt{\lambda_{H,n}}$.

Appendix F

Absence of the second term on RHS of Eq. (4.10)

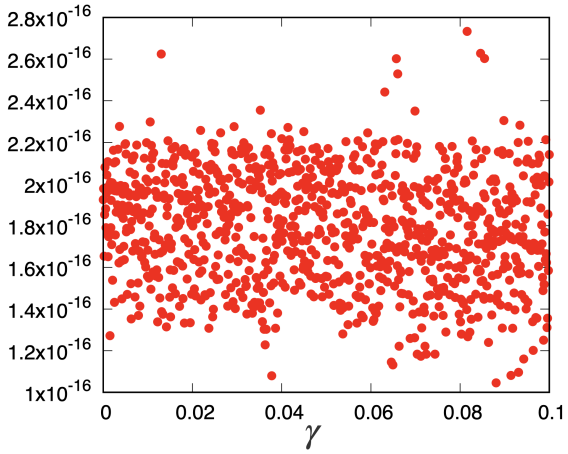

Figure F.1: Plot of the maximum Err against γ.

Thus far, we could not prove that the second term on RHS of Eq. (4.10) can be regarded as zero with numerical accuracy, but we verify that this term is zero, at least, in the numerical simulation of harmonic systems as follows: Let us calculate the ratio of the second term in Eq. (4.10) to the first term using

$$\text{Err} := \frac{\left|\left[\left(\int_{C_{ij}} dt \boldsymbol{v}_{T,ij}\right) \cdot \boldsymbol{n}_{ij}\right] \boldsymbol{n}_{ij}\right|}{\left|\int_{C_{ij}} dt \boldsymbol{v}_{T,ij}\right|}. \tag{F.1}$$

Figure F.1 shows the plots of the largest Err in contacting pairs against γ, which indicates $|\text{Err}| < 3 \times 10^{-16}$. As our calculation is based on double precision,

which has only 16 significant digits, Err can be regarded as zero.

Appendix G

The behavior of the smallest eigenvalue near stress-drop points

In this appendix, we provide an in-depth explain the behavior of the smallest eigenvalue in the vicinity of the stress-drop points in detail. We adopt the following protocol to reduce the step strain small in the vicinity of the stress-drop point. We adopt $\Delta\gamma_{\rm in} = 10^{-4}$ in the appendix. We use $\Delta\gamma = \Delta\gamma_{\rm in}$ if there is no plastic event during the strain increment $\Delta\gamma$. If we find a stress drop during the strain from γ to $\gamma + \Delta\gamma$, we restore the system to the state γ, and examine $\gamma + 0.1\Delta\gamma_{\rm in}$. If we do not find any stress drop, we further add the strain with $\Delta\gamma_{\rm in}$; if we still have a stress drop, we repeat the procedure of restoring and adding strain $0.01\Delta\gamma_{\rm in}$. This protocol is repeated to detect stress drop events until we reach $\Delta\gamma < \Delta\gamma_{\rm Th}$. In this appendix, we illustrate how the results depend on the choice of $\Delta\gamma_{\rm Th}$, where the smallest value of $\Delta\gamma_{\rm Th}$ is 10^{-10}.

Figure G.1 presents the stress-strain curves obtained using this protocol. The upper branch in Fig. G.1 represents the shear stress below the stress drop, and the lower branch represents the shear stress above the stress drop. The smallest γ in the lower branch and the largest γ in the upper branch strongly depend on $\Delta\gamma_{\rm Th}$. As shown in Fig. G.2, the stress drop takes place at $\gamma \approx 0.01330$ for $\Delta\gamma_{\rm Th} = 10^{-4}$, whereas the critical strain γ_c for the stress drop approaches 0.013334 as $\Delta\gamma_{\rm Th}$ decreases, where γ_c is 0.013334 for $\Delta\gamma_{\rm Th} \leq 10^{-6}$.

Figure G.3 plots the behavior of the smallest eigenvalue against γ corresponding to Fig. G.1 for $\Delta\gamma_{\rm Th} = 10^{-10}$ immediately below the stress drop point, where the symbols correspond to the analysis for the corresponding $\Delta\gamma$ as in Fig. G.1. We have confirmed that there is no precursor of the eigenvalues below γ_c as observed in Hertzian and Lennard-Jones systems [107, 108, 111]. Thus, the harmonic system does not have any precursors in the behavior of the smallest eigenvalue.

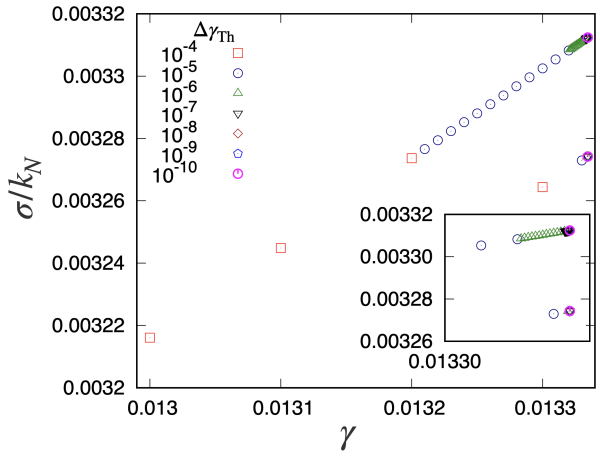

Figure G.1: The stress-strain curve for $N = 128$, which are the stress drop points for various $\Delta\gamma_{\mathrm{Th}}$ (from $\Delta\gamma_{\mathrm{Th}} = 10^{-4}$ and $\Delta\gamma_{\mathrm{Th}} = 10^{-10}$).

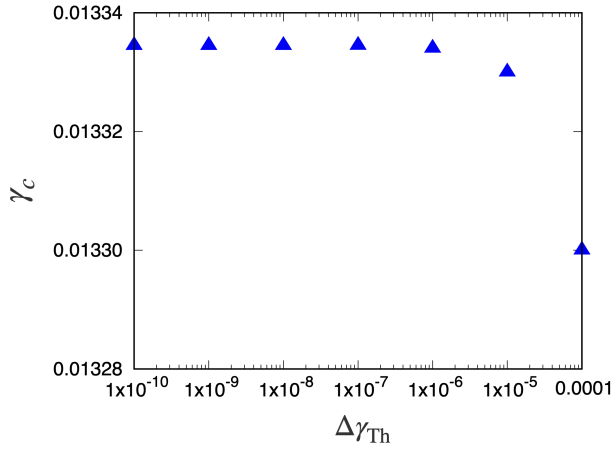

Figure G.2: Plot of the critical strain γ_c against $\Delta\gamma_{\mathrm{Th}}$ for $N = 128$.

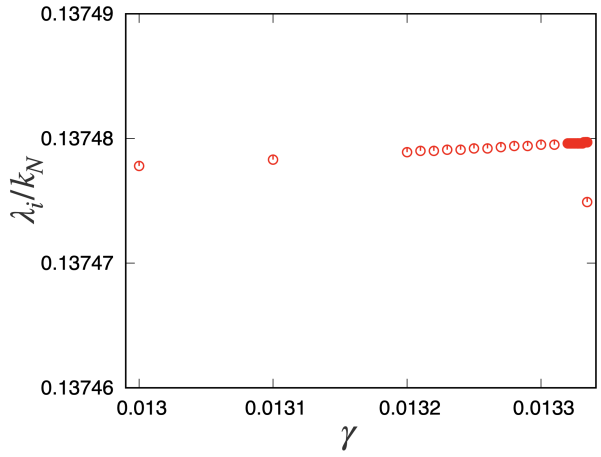

Figure G.3: The plot of the smallest non-zero eigenvalue in the vicinity of γ_c for $\Delta\gamma_{\mathrm{Th}} = 1.0 \times 10^{-10}$.

Appendix H

Some properties of the Hessian matrix in a harmonic potential

In this appendix, we briefly summarize the properties of the Hessian matrix of the harmonic potential. In Sec. H.1, we explicitly express the elements of the Hessian matrix in this model. In Sec. H.2, we demonstrate that the symmetry of the Hessian matrix still holds even under the Lees-Edwards boundary condition.

H.1 The explicit expression for the Hessian matrix

In this section, we present an explicit expression for the Hessian matrix. To this end, we return to the effective potential in Eq. (4.20). It is straightforward to

obtain

$$\frac{\partial^2 \delta \boldsymbol{r}_{ij,\perp}^2}{\partial x_i^2} = 2 - 2(n_{ij}^x)^2, \tag{H.1}$$

$$\frac{\partial^2 \delta \boldsymbol{r}_{ij,\perp}^2}{\partial x_i \partial y_i} = -2 n_{ij}^x n_{ij}^y, \tag{H.2}$$

$$\frac{\partial^2 \delta \boldsymbol{r}_{ij,\perp}^2}{\partial x_i \partial \ell_i} = 2 n_{ij}^y, \tag{H.3}$$

$$\frac{\partial^2 \delta \boldsymbol{r}_{ij,\perp}^2}{\partial y_i \partial x_i} = \frac{\partial^2 \delta \boldsymbol{r}_{ij,\perp}^2}{\partial x_i \partial y_i}, \tag{H.4}$$

$$\frac{\partial^2 \delta \boldsymbol{r}_{ij,\perp}^2}{\partial y_i^2} = 2 - 2(n_{ij}^y)^2, \tag{H.5}$$

$$\frac{\partial^2 \delta \boldsymbol{r}_{ij,\perp}^2}{\partial y_i \partial \ell_i} = 2 n_{ij}^x, \tag{H.6}$$

$$\frac{\partial^2 \delta \boldsymbol{r}_{ij,\perp}^2}{\partial \ell_i \partial x_i} = \frac{\partial^2 \delta \boldsymbol{r}_{ij,\perp}^2}{\partial x_i \partial \ell_i}, \tag{H.7}$$

$$\frac{\partial^2 \delta \boldsymbol{r}_{ij,\perp}^2}{\partial \ell_i \partial y_i} = \frac{\partial^2 \delta \boldsymbol{r}_{ij,\perp}^2}{\partial y_i \partial \ell_i}, \tag{H.8}$$

$$\frac{\partial^2 \delta \boldsymbol{r}_{ij,\perp}^2}{\partial \ell_i^2} = 2. \tag{H.9}$$

Thus, we obtain

$$\mathcal{H}_{ij}^{xx} = \frac{\partial^2 \delta e_{ij}}{\partial x_i \partial x_j} = -\frac{\partial^2 \delta e_{ij}}{\partial x_i^2} = -k_N + k_N \left[1 + \frac{\xi_{N,ij}}{|\boldsymbol{r}_{ij}|}\right] (n_{ij}^y)^2 - k_T (n_{ij}^y)^2, \tag{H.10}$$

$$\mathcal{H}_{ij}^{xy} = \frac{\partial^2 \delta e_{ij}}{\partial x_i \partial y_j} = -\frac{\partial^2 \delta e_{ij}}{\partial x_i \partial y_i} = -k_N \left[1 + \frac{\xi_{N,ij}}{|\boldsymbol{r}_{ij}|}\right] n_{ij}^x n_{ij}^y + k_T n_{ij}^x n_{ij}^y, \tag{H.11}$$

$$\mathcal{H}_{ij}^{x\ell} = \frac{\partial^2 \delta e_{ij}}{\partial x_i \partial \ell_j} = \frac{\partial^2 \delta e_{ij}}{\partial x_i \partial \ell_i} = k_T n_{ij}^y, \tag{H.12}$$

$$\mathcal{H}_{ij}^{yy} = \frac{\partial^2 \delta e_{ij}}{\partial y_i \partial y_j} = -\frac{\partial^2 \delta e_{ij}}{\partial y_i^2} = -k_N + k_N \left[1 + \frac{\xi_{N,ij}}{|\boldsymbol{r}_{ij}|}\right] (n_{ij}^x)^2 - k_T (n_{ij}^x)^2, \tag{H.13}$$

$$\mathcal{H}_{ij}^{y\ell} = \frac{\partial^2 \delta e_{ij}}{\partial y_i \partial \ell_j} = \frac{\partial^2 \delta e_{ij}}{\partial y_i \partial \ell_i} = -k_T n_{ij}^x, \tag{H.14}$$

$$\mathcal{H}_{ij}^{\ell\ell} = \frac{\partial^2 \delta e_{ij}}{\partial \ell_i \partial \ell_j} = \frac{\partial^2 \delta e_{ij}}{\partial \ell_i^2} = k_T \tag{H.15}$$

for $i \neq j$ and

$$\mathcal{H}_{ii}^{xx} = \sum_{j\neq i} \frac{\partial^2 \delta e_{ij}}{\partial x_i^2} = -\sum_{j\neq i} \left[-k_N + k_N \left[1 + \frac{\xi_{N,ij}}{|\boldsymbol{r}_{ij}|} \right] (n_{ij}^y)^2 - k_T (n_{ij}^y)^2 \right], \quad \text{(H.16)}$$

$$\mathcal{H}_{ii}^{xy} = \sum_{j\neq i} \frac{\partial^2 \delta e_{ij}}{\partial x_i \partial y_i} = -\sum_{j\neq i} \left[-k_N \left[1 + \frac{\xi_{N,ij}}{|\boldsymbol{r}_{ij}|} \right] n_{ij}^x n_{ij}^y + k_T n_{ij}^x n_{ij}^y \right], \quad \text{(H.17)}$$

$$\mathcal{H}_{ii}^{x\ell} = \sum_{j\neq i} \frac{\partial^2 \delta e_{ij}}{\partial x_i \partial \ell_i} = \sum_{j\neq i} k_T n_{ij}^y, \quad \text{(H.18)}$$

$$\mathcal{H}_{ii}^{yy} = \sum_{j\neq i} \frac{\partial^2 \delta e_{ij}}{\partial y_i^2} = \sum_{j\neq i} \left[-k_N + k_N \left[1 + \frac{\xi_{N,ij}}{|\boldsymbol{r}_{ij}|} \right] (n_{ij}^x)^2 - k_T (n_{ij}^x)^2 \right], \quad \text{(H.19)}$$

$$\mathcal{H}_{ii}^{y\ell} = \sum_{j\neq i} \frac{\partial^2 \delta e_{ij}}{\partial y_i \partial \ell_i} = -\sum_{j\neq i} k_T n_{ij}^x, \quad \text{(H.20)}$$

$$\mathcal{H}_{ii}^{\ell\ell} = \sum_{j\neq i} \frac{\partial^2 \delta e_{ij}}{\partial \ell_i^2} = \sum_{j\neq i} k_T. \quad \text{(H.21)}$$

H.2 Effect of the boundary condition to the Hessian matrix

In this section, we explain the influence of strain and the boundary condition on the Hessian matrix in detail to determine whether the symmetry of the Hessian matrix is still maintained, even if we consider a system with non-zero strain.

First, let us consider the case in which grain i interacts with the grain j through a mirror image in x-direction, as shown in Fig. H.1. In this case, $\boldsymbol{r}_{ij}$ is given by

$$\boldsymbol{r}_{ij} := \boldsymbol{r}_i - \boldsymbol{r}_j - L\boldsymbol{e}_x, \quad \text{(H.22)}$$

where $\boldsymbol{e}_x := (1,0)^{\mathrm{T}}$. Similarly, $\boldsymbol{r}_{ji}$ is given by

$$\boldsymbol{r}_{ji} := \boldsymbol{r}_j - \boldsymbol{r}_i + L\boldsymbol{e}_x. \quad \text{(H.23)}$$

Thus, $\boldsymbol{r}_{ij}$ satisfies

$$\boldsymbol{r}_{ji} = -\boldsymbol{r}_{ij}. \quad \text{(H.24)}$$

Then, we obtain

$$\begin{aligned} \xi_{N,ij} :&= \frac{d_i + d_j}{2} - |\boldsymbol{r}_{ij}| \\ &= \frac{d_i + d_j}{2} - |\boldsymbol{r}_{ji}| \\ &= \xi_{N,ji}. \end{aligned} \quad \text{(H.25)}$$

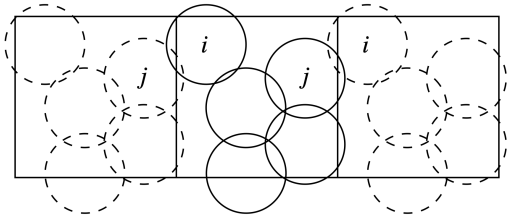

Figure H.1: A schematic of the case where the grain i interacts with the grain j through the mirror image in x-direction.

Thus, the result is independent of the strain, and the symmetry of the Hessian is still valid in this case.

Next, let us consider the case in which the grain i interacts with the grain j through a mirror image in the y-direction (see Fig. H.2). In this case, $\boldsymbol{r}_{ij}$ is given by

$$\boldsymbol{r}_{ij} := \boldsymbol{r}_i - \boldsymbol{r}_j + L\boldsymbol{e}_y + \gamma L\boldsymbol{e}_x, \tag{H.26}$$

where $\boldsymbol{e}_y := (0,1)^{\mathrm{T}}$. Similarly, $\boldsymbol{r}_{ji}$ is given by

$$\boldsymbol{r}_{ji} := \boldsymbol{r}_j - \boldsymbol{r}_i - L\boldsymbol{e}_y - \gamma L\boldsymbol{e}_x. \tag{H.27}$$

Since the relation

$$\boldsymbol{r}_{ji} = -\boldsymbol{r}_{ij}, \tag{H.28}$$

we obtain

$$\begin{aligned} \xi_{N,ij} :&= \frac{d_i + d_j}{2} - |\boldsymbol{r}_{ij}| \\ &= \frac{d_i + d_j}{2} - |\boldsymbol{r}_{ji}| \\ &= \xi_{N,ji}. \end{aligned} \tag{H.29}$$

Thus, $\xi_{N,ij}$ and $\xi_{N,ji}$ depend on γ in the same way. With the aid of Eqs. (H.26),(H.27) and (H.29), the Hessian matrix depends on γ if the grain interacts with another grain through the mirror image in y-direction, although the symmetry of the Hessian is still maintained.

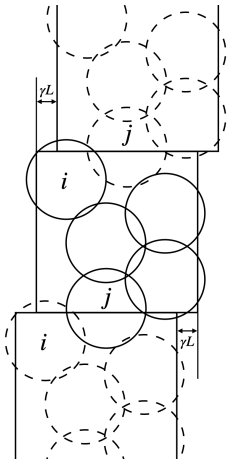

Figure H.2: A schematic of the case that the grain i interacts with the grain j through the mirror image in y-direction.

Appendix I

Some properties of the Jacobian matrix in a harmonic system and its equivalency to the Hessian matrix

In this appendix, we briefly summarize the properties of the Jacobian matrix for the harmonic contact model that was previously used in the description of frictional grains [115–117, 119]. In Sec.I.1, we present explicit forms of the diagonal and non-diagonal blocks of the Jacobian matrix. In Sec.I.2, we present the derivation of the Jacobian for the harmonic contact model. In Sec. I.3, we explicitly write the elements of the Jacobian matrix in the model.

I.1 Jacobian block elements

Let us write a 3×3 sub-matrix $\mathcal{J}_{ij}$, which is the (ij) block element of the Jacobian obtained from Eq. (4.19):

$$
\begin{aligned}
\left[\mathcal{J}_{ij}^{\alpha\beta}\right] &:= \left[-\frac{\partial \tilde{F}_i^{\alpha}}{\partial q_j^{\beta}}\right] \\
&= \begin{bmatrix} -\partial_{q_j^x} F_i^x & -\partial_{q_j^y} F_i^x & -\partial_{q_j^\ell} F_i^x \\ -\partial_{q_j^x} F_i^y & -\partial_{q_j^y} F_i^y & -\partial_{q_j^\ell} F_i^y \\ -\partial_{q_j^x} \tilde{T}_i & -\partial_{q_j^y} \tilde{T}_i & -\partial_{q_j^\ell} \tilde{T}_i \end{bmatrix} \\
&= \begin{bmatrix} -\sum_{k=1;k\neq j}^{N} \partial_{q_j^x} f_{ik}^x & -\sum_{k=1;k\neq j}^{N} \partial_{q_j^y} f_{ik}^x & -\sum_{k=1;k\neq j}^{N} \partial_{q_j^\ell} f_{ik}^x \\ -\sum_{k=1;k\neq j}^{N} \partial_{q_j^x} f_{ik}^y & -\sum_{k=1;k\neq j}^{N} \partial_{q_j^y} f_{ik}^y & -\sum_{k=1;k\neq j}^{N} \partial_{q_j^\ell} f_{ik}^y \\ -\sum_{k=1;k\neq j}^{N} \partial_{q_j^x} \tilde{T}_{ik} & -\sum_{k=1;k\neq j}^{N} \partial_{q_j^y} \tilde{T}_{ik} & -\sum_{k=1;k\neq j}^{N} \partial_{q_j^\ell} \tilde{T}_{ik} \end{bmatrix} \\
&= \begin{cases} \begin{bmatrix} -\partial_{q_j^x} f_{ij}^x & -\partial_{q_j^y} f_{ij}^x & -\partial_{q_j^\ell} f_{ij}^x \\ -\partial_{q_j^x} f_{ij}^y & -\partial_{q_j^y} f_{ij}^y & -\partial_{q_j^\ell} f_{ij}^y \\ -\partial_{q_j^x} \tilde{T}_{ij} & -\partial_{q_j^y} \tilde{T}_{ij} & -\partial_{q_j^\ell} \tilde{T}_{ij} \end{bmatrix} & (i \neq j) \\ \begin{bmatrix} -\sum_{k=1;k\neq i}^{N} \partial_{q_i^x} f_{ik}^x & -\sum_{k=1;k\neq i}^{N} \partial_{q_i^y} f_{ik}^x & -\sum_{k=1;k\neq i}^{N} \partial_{q_i^\ell} f_{ik}^x \\ -\sum_{k=1;k\neq i}^{N} \partial_{q_i^x} f_{ik}^y & -\sum_{k=1;k\neq i}^{N} \partial_{q_i^y} f_{ik}^y & -\sum_{k=1;k\neq i}^{N} \partial_{q_i^\ell} f_{ik}^y \\ -\sum_{k=1;k\neq i}^{N} \partial_{q_i^x} \tilde{T}_{ik} & -\sum_{k=1;k\neq i}^{N} \partial_{q_i^y} \tilde{T}_{ik} & -\sum_{k=1;k\neq i}^{N} \partial_{q_i^\ell} \tilde{T}_{ik} \end{bmatrix} & (i = j) \end{cases},
\end{aligned}
\tag{I.1}
$$

where the superscripts α and β correspond to x, y, ℓ-components, and i and j are the grain numbers. Here, $f_{ij}^{\zeta}, \tilde{T}_{ij}$ are ζ-component of $\boldsymbol{f}_{ij}$ and scaled torque that the i-th grain receives from the j-th grain, respectively. The sub-matrix for $i = j$ is given by

$$
\left[\mathcal{J}_{ii}^{\alpha\beta}\right] = \begin{bmatrix} \sum_{k=1;k\neq i}^{N} \partial_{q_k^x} f_{ik}^x & \sum_{k=1;k\neq i}^{N} \partial_{q_k^y} f_{ik}^x & -\sum_{k=1;k\neq i}^{N} \partial_{q_k^\ell} f_{ik}^x \\ \sum_{k=1;k\neq i}^{N} \partial_{q_k^x} f_{ik}^y & \sum_{k=1;k\neq i}^{N} \partial_{q_k^y} f_{ik}^y & -\sum_{k=1;k\neq i}^{N} \partial_{q_k^\ell} f_{ik}^y \\ \sum_{k=1;k\neq i}^{N} \partial_{q_k^x} \tilde{T}_{ik} & \sum_{k=1;k\neq i}^{N} \partial_{q_k^y} \tilde{T}_{ik} & -\sum_{k=1;k\neq i}^{N} \partial_{q_k^\ell} \tilde{T}_{ik} \end{bmatrix}, \tag{I.2}
$$

where we have used $\partial_{q_i^\kappa} f_{ik}^{\zeta} = -\partial_{q_k^\kappa} f_{ik}^{\zeta}, \partial_{q_i^\kappa} \tilde{T}_{ik} = -\partial_{q_i^\kappa} \tilde{T}_{ik}, \partial_{q_i^\ell} f_{ik}^{\zeta} = \partial_{q_k^\ell} f_{ik}^{\zeta}$, and $\partial_{q_i^\ell} \tilde{T}_{ik} = \partial_{q_i^\ell} \tilde{T}_{ik}$. Here, the superscripts ζ and κ correspond to x, y components.

I.2 Derivation of Jacobian matrix in the harmonic system

Let us consider only the normal and tangential elastic contact forces

$$
\boldsymbol{f}_{N,ij} = k_N \xi_{N,ij} \boldsymbol{n}_{ij}, \tag{I.3}
$$

$$
\boldsymbol{f}_{T,ij} = -k_T \boldsymbol{\xi}_{T,ij}, \tag{I.4}
$$

where the integration of $d\boldsymbol{\xi}_{T,ij}$

$$\boldsymbol{\xi}_{T,ij} := \int_{C_{ij}} d\boldsymbol{\xi}_{T,ij} \tag{I.5}$$

is performed during the contact between the i-th and j-th grains. Since Eq. (I.5) does not contain the second term on RHS of Eq. (4.10), $\boldsymbol{\xi}_{T,ij}$ may not be perpendicular to $\boldsymbol{\xi}_{N,ij}$. Nevertheless, we adopt Eq. (I.5) for simplicity. Here, $d\boldsymbol{\xi}_{T,ij}$ is defined as

$$d\boldsymbol{\xi}_{T,ij} = d\boldsymbol{r}_{ij} - (d\boldsymbol{r}_{ij} \cdot \boldsymbol{n}_{ij})\boldsymbol{n}_{ij} - d\boldsymbol{\ell}_{ij} \times \boldsymbol{n}_{ij}, \tag{I.6}$$

where $\boldsymbol{\ell}_{ij}$ is defined as

$$\boldsymbol{\ell}_{ij} := \begin{bmatrix} 0 \\ 0 \\ \ell_i + \ell_j \end{bmatrix}. \tag{I.7}$$

Each component of Eq. (I.6) is written as

$$d\xi^x_{T,ij} = dr^x_{ij} - (d\boldsymbol{r}_{ij} \cdot \boldsymbol{n}_{ij})n^x_{ij} + d\ell_{ij}n^y_{ij}, \tag{I.8}$$

$$d\xi^y_{T,ij} = dr^y_{ij} - (d\boldsymbol{r}_{ij} \cdot \boldsymbol{n}_{ij})n^y_{ij} - d\ell_{ij}n^x_{ij}. \tag{I.9}$$

The derivative of the normal force is given by

$$\partial_{r^\zeta_i} f^\kappa_{N,ij} = k_N \left[\frac{\xi_{N,ij}}{r_{ij}} \delta_{\zeta\kappa} - \left(1 + \frac{\xi_{N,ij}}{r_{ij}} \right) n^\zeta_{ij} n^\kappa_{ij} \right], \tag{I.10}$$

$$\partial_{\ell_i} f^\kappa_{N,ij} = 0, \tag{I.11}$$

where Kronecker's delta $\delta_{\zeta\kappa}$ satisfies $\delta_{\zeta\kappa} = 1$ for $\zeta = \kappa$ and $\delta_{\zeta\kappa} = 0$ otherwise. We have used

$$\frac{\partial n^\zeta_{ij}}{\partial r^\kappa_i} = \frac{1}{r_{ij}} \left(\delta_{\zeta\kappa} - n^\zeta_{ij} n^\kappa_{ij} \right), \tag{I.12}$$

$$\frac{\partial r_{ij}}{\partial r^\zeta_i} = n^\zeta_{ij} \tag{I.13}$$

to obtain Eq. (I.10).

The derivative of the tangential force is written as

$$\partial_{r^\zeta_i} f^\kappa_{T,ij} = -k_T \left(\delta_{\zeta\kappa} - n^\zeta_{ij} n^\kappa_{ij} \right), \tag{I.14}$$

$$\partial_{\ell_i} f^\kappa_{T,ij} = -\varepsilon_\kappa k_T n^{\nu_\kappa}_{ij}, \tag{I.15}$$

where ε_ζ and ν_ζ are defined, respectively, as

$$\varepsilon_\zeta := \begin{cases} 1 & (\zeta = x) \\ -1 & (\zeta = y), \end{cases} \tag{I.16}$$

$$\nu_\zeta := \begin{cases} y & (\zeta = x) \\ x & (\zeta = y). \end{cases} \tag{I.17}$$

Here, $\partial_{r_i^\zeta}\xi^\kappa_{T,ij}$ and $\partial_{\ell_i}\xi^\kappa_{T,ij}$ in Eqs. (I.14) and (I.15) satisfy the following:

$$\frac{\partial \xi^\kappa_{T,ij}}{\partial r_i^\zeta} = \delta_{\zeta\kappa} - n^\zeta_{ij} n^\kappa_{ij}, \tag{I.18}$$

$$\frac{\partial \xi^\kappa_{T,ij}}{\partial \ell_i} = \varepsilon_\kappa n_{ij}^{\nu_\kappa}. \tag{I.19}$$

The derivation of Eqs. (I.18) and (I.19) are as follows [115]. From Eq. (I.6), $d\xi^\zeta_{T,ij}$ can be written as

$$d\xi^\zeta_{T,ij} = dr^\zeta_{ij} - (d\boldsymbol{r}_{ij}\cdot\boldsymbol{n}_{ij})n^\zeta_{ij} + (-1)^\zeta(d\ell_i + d\ell_j)n_{ij}^{\nu_\zeta}. \tag{I.20}$$

Then, $d\xi^x_{T,ij}$ satisfies

$$\begin{aligned} d\xi^x_{T,ij} &= dr^x_{ij} - \sum_{\kappa=x,y} dr^\kappa_{ij} n^\kappa_{ij} n^x_{ij} + n^y_{ij}(d\ell_i + d\ell_j) \\ &= (1-(n^x_{ij})^2)dr^x_{ij} - n^x_{ij}n^y_{ij}dr^y_{ij} + n^y_{ij}(d\ell_i + d\ell_j) \\ &= (n^y_{ij})^2 dr^x_{ij} - n^x_{ij}n^y_{ij}dr^y_{ij} + n^y_{ij}(d\ell_i + d\ell_j) \\ &= (n^y_{ij})^2(dx_i - dx_j) - n^x_{ij}n^y_{ij}(dy_i - dy_j) + n^y_{ij}(d\ell_i + d\ell_j). \end{aligned} \tag{I.21}$$

Similarly, $d\xi^y_{T,ij}$ also satisfies

$$d\xi^y_{T,ij} = -n^x_{ij}n^y_{ij}(dx_i - dx_j) + (n^y_{ij})^2(dy_i - dy_j) - n^x_{ij}(d\ell_i + d\ell_j). \tag{I.22}$$

Here, $d\xi^\zeta_{T,ij}$is the function of $x_i, y_i, \ell_i, x_j, y_j$, and ℓ_j. We obtain the differential form of $d\xi^\zeta_{T,ij}$:

$$\begin{aligned} d\xi^\zeta_{T,ij} = &\left(\frac{\partial \xi^\zeta_{T,ij}}{\partial x_i}\right)_{(y_i,\ell_i,x_j,y_j,\ell_j)} dx_i + \left(\frac{\partial \xi^\zeta_{T,ij}}{\partial x_j}\right)_{(x_i,y_i,\ell_i,y_j,\ell_j)} dx_j \\ &+ \left(\frac{\partial \xi^\zeta_{T,ij}}{\partial y_i}\right)_{(x_i,\ell_i,x_j,y_j,\ell_j)} dy_i + \left(\frac{\partial \xi^\zeta_{T,ij}}{\partial y_j}\right)_{(x_i,y_i,\ell_i,x_j,\ell_j)} dy_j \\ &+ \left(\frac{\partial \xi^\zeta_{T,ij}}{\partial \ell_i}\right)_{(x_i,y_i,x_j,y_j,\ell_j)} d\ell_i + \left(\frac{\partial \xi^\zeta_{T,ij}}{\partial \ell_j}\right)_{(x_i,y_i,\ell_i,x_j,y_j)} d\ell_j. \end{aligned} \tag{I.23}$$

Next, we obtain Eqs. (I.18), (I.19), by comparing Eqs. (I.21) and (I.22) using Eq. (I.23).

Because the scaled torque $\tilde{T}_{ij}$ satisfies

$$\tilde{T}_{ij} := \frac{2T_{ij}}{d_i} = -n^x_{ij} f^y_{T,ij} + n^y_{ij} f^x_{T,ij}, \tag{I.24}$$

we obtain

$$\begin{aligned}
\partial_{r_i^\zeta}\tilde{T}_{ij} &= -\left(\partial_{r_i^\zeta} n_{ij}^x\right) f_{T,ij}^y - n_{ij}^x \partial_{r_i^\zeta} f_{T,ij}^y + \left(\partial_{r_i^\zeta} n_{ij}^y\right) f_{T,ij}^x + n_{ij}^y \partial_{r_i^\zeta} f_{T,ij}^x \\
&= -\left(\frac{\delta_{\zeta x}}{r_{ij}} - \frac{n_{ij}^\zeta n_{ij}^x}{r_{ij}}\right) f_{T,ij}^y + k_T n_{ij}^x \left(\delta_{\zeta y} - n_{ij}^\zeta n_{ij}^y\right) + \left(\frac{\delta_{\zeta y}}{r_{ij}} - \frac{n_{ij}^\zeta n_{ij}^y}{r_{ij}}\right) f_{T,ij}^x - k_T n_{ij}^y \left(\delta_{\zeta x} - n_{ij}^\zeta n_{ij}^x\right) \\
&= -\varepsilon_\kappa \frac{n_{ij}^{\nu_\kappa}}{r_{ij}} \left(\boldsymbol{n}_{ij} \cdot \boldsymbol{f}_{T,ij}\right) - \varepsilon_\kappa n_{ij}^{\nu_\kappa} \left(\boldsymbol{n}_{ij} \cdot \boldsymbol{n}_{ij}\right) - \varepsilon_\kappa n_{ij}^{\nu_\kappa}, \qquad \text{(I.25)} \\
\partial_{\ell_i}\tilde{T}_{ij} &= -n_{ij}^x \partial_{\ell_i} f_{T,ij}^y + n_{ij}^y \partial_{\ell_i} f_{T,ij}^x \\
&= -n_{ij}^x k_T n_{ij}^x - n_{ij}^y k_T n_{ij}^y \\
&= -k_T, \qquad \text{(I.26)}
\end{aligned}$$

where we have used $\boldsymbol{f}_{T,ij} \cdot \boldsymbol{n}_{ij} = 0$ and $\boldsymbol{n}_{ij} \cdot \boldsymbol{n}_{ij} = 1$.

I.3 Explicit form of Jacobian for grains interacting with harmonic potential

From Sec. I.2, the off-diagonal elements of the Jacobian matrix $\mathcal{J}_{ij}^{\alpha\beta} := -\partial_{q_j^s} \tilde{F}_i^r$ ($\alpha, \beta = x, y, \ell$) with $i \neq j$ are given by

$$\mathcal{J}_{ij}^{xx} = -k_N + k_N \left[1 + \frac{\xi_{N,ij}}{r_{ij}}\right] (n_{ij}^y)^2 - k_T (n_{ij}^y)^2, \qquad \text{(I.27)}$$

$$\mathcal{J}_{ij}^{xy} = -k_N \left[1 + \frac{\xi_{N,ij}}{r_{ij}}\right] n_{ij}^x n_{ij}^y + k_T n_{ij}^x n_{ij}^y, \qquad \text{(I.28)}$$

$$\mathcal{J}_{ij}^{x\ell} = -k_T n_{ij}^y, \qquad \text{(I.29)}$$

$$\mathcal{J}_{ij}^{yx} = -k_N \left[1 + \frac{\xi_{N,ij}}{r_{ij}}\right] n_{ij}^x n_{ij}^y + k_T n_{ij}^x n_{ij}^y, \qquad \text{(I.30)}$$

$$\mathcal{J}_{ij}^{yy} = -k_N + k_N \left[1 + \frac{\xi_{N,ij}}{r_{ij}}\right] (n_{ij}^x)^2 - k_T (n_{ij}^x)^2, \qquad \text{(I.31)}$$

$$\mathcal{J}_{ij}^{y\ell} = k_T n_{ij}^x, \qquad \text{(I.32)}$$

$$\mathcal{J}_{ij}^{\ell x} = k_T n_{ij}^y, \qquad \text{(I.33)}$$

$$\mathcal{J}_{ij}^{\ell y} = -k_T n_{ij}^x, \qquad \text{(I.34)}$$

$$\mathcal{J}_{ij}^{\ell\ell} = k_T. \qquad \text{(I.35)}$$

Notably, the elements of the Jacobian matrix are independent of $\xi_{T,ij}$.

With the aid of Eq. (I.1), the elements in the diagonal block $\mathcal{J}_{ii}^{rs}$ are given

by

$$\mathcal{J}_{ii}^{xx} = -\sum_{j\neq i}\left\{-k_N + k_N\left[1+\frac{\xi_{N,ij}}{r_{ij}}\right](n_{ij}^y)^2 - k_T(n_{ij}^y)^2\right\}, \tag{I.36}$$

$$\mathcal{J}_{ii}^{xy} = -\sum_{j\neq i}\left\{-k_N\left[1+\frac{\xi_{N,ij}}{r_{ij}}\right]n_{ij}^x n_{ij}^y + k_T n_{ij}^x n_{ij}^y\right\}, \tag{I.37}$$

$$\mathcal{J}_{ii}^{x\ell} = \sum_{j\neq i} k_T n_{ij}^y, \tag{I.38}$$

$$\mathcal{J}_{ii}^{yx} = -\sum_{j\neq i}\left\{-k_N\left[1+\frac{\xi_{N,ij}}{r_{ij}}\right]n_{ij}^x n_{ij}^y + k_T n_{ij}^x n_{ij}^y\right\}, \tag{I.39}$$

$$\mathcal{J}_{ii}^{yy} = -\sum_{j\neq i}\left\{-k_N + k_N\left[1+\frac{\xi_{N,ij}}{r_{ij}}\right](n_{ij}^x)^2 - k_T(n_{ij}^x)^2\right\}, \tag{I.40}$$

$$\mathcal{J}_{ii}^{y\ell} = -\sum_{j\neq i} k_T n_{ij}^x, \tag{I.41}$$

$$\mathcal{J}_{ii}^{\ell x} = \sum_{j\neq i} k_T n_{ij}^y, \tag{I.42}$$

$$\mathcal{J}_{ii}^{\ell y} = -\sum_{j\neq i} k_T n_{ij}^x, \tag{I.43}$$

$$\mathcal{J}_{ii}^{\ell\ell} = \sum_{j\neq i} k_T. \tag{I.44}$$

The expressions in Eqs. (I.27)–(I.44) are equivalent to Eqs. (H.10)–(H.21) for a Hessian matrix. Thus, we conclude that the Jacobian matrix is equivalent to the Hessian matrix for the harmonic system without considering dynamical slip.

Appendix J

The detailed properties of rigidity

This appendix consists of two sections. In Appendix J.1, we present the detailed expressions of rigidity g. In Appendix J.2, we demonstrate the quantitative accuracy of the Hessian analysis in the linear response regime by comparing the theoretical evaluation of the rigidity with that obtained by the numerical simulation as in Ref. [119].

J.1 The expression of g

The symmetrized shear stress in Eq. (4.15) is expressed as

$$\sigma(\boldsymbol{q}^{\mathrm{FB}}(\gamma)) = \frac{\sigma_{xy}(\boldsymbol{q}^{\mathrm{FB}}(\gamma)) + \sigma_{yx}(\boldsymbol{q}^{\mathrm{FB}}(\gamma))}{2}, \tag{J.1}$$

where

$$\sigma_{\alpha\beta}(\boldsymbol{q}^{\mathrm{FB}}(\gamma)) := -\frac{1}{2L^2}\sum_{i,j(i\neq j)} f_{ij}^{\alpha}(\boldsymbol{q}^{\mathrm{FB}}(\gamma)) r_{ij}^{\beta}(\boldsymbol{q}^{\mathrm{FB}}(\gamma)). \tag{J.2}$$

Substituting Eq. (J.1) into Eq. (4.17), we obtain

$$\begin{aligned} g(\gamma) &= \lim_{\Delta\gamma\to 0}\frac{1}{2\Delta\gamma}\left[\sigma_{xy}(\boldsymbol{q}^{\mathrm{FB}}(\gamma+\Delta\gamma)) + \sigma_{yx}(\boldsymbol{q}^{\mathrm{FB}}(\gamma+\Delta\gamma)) - \left\{\sigma_{xy}(\boldsymbol{q}^{\mathrm{FB}}(\gamma)) + \sigma_{yx}(\boldsymbol{q}^{\mathrm{FB}}(\gamma))\right\}\right] \\ &= -\lim_{\Delta\gamma\to 0}\frac{1}{4\Delta\gamma L^2}\left[f_{ij}^{x}(\boldsymbol{q}^{\mathrm{FB}}(\gamma+\Delta\gamma)) r_{ij}^{y}(\boldsymbol{q}^{\mathrm{FB}}(\gamma+\Delta\gamma)) + f_{ij}^{y}(\boldsymbol{q}^{\mathrm{FB}}(\gamma+\Delta\gamma)) r_{ij}^{x}(\boldsymbol{q}^{\mathrm{FB}}(\gamma+\Delta\gamma))\right. \\ &\qquad \left. - \left\{f_{ij}^{x}(\boldsymbol{q}^{\mathrm{FB}}(\gamma)) r_{ij}^{y}(\boldsymbol{q}^{\mathrm{FB}}(\gamma)) + f_{ij}^{y}(\boldsymbol{q}^{\mathrm{FB}}(\gamma)) r_{ij}^{x}(\boldsymbol{q}^{\mathrm{FB}}(\gamma))\right\}\right]. \end{aligned} \tag{J.3}$$

Substituting Eq. (J.3) into Eq. (J.1), the rigidity g is expressed as

$$g(\gamma) = -\lim_{\Delta\gamma\to 0}\frac{1}{4\Delta\gamma L^2}\left[f_{ij}^x(\boldsymbol{q}^{\mathrm{FB}}(\gamma+\Delta\gamma))r_{ij}^y(\boldsymbol{q}^{\mathrm{FB}}(\gamma+\Delta\gamma)) + f_{ij}^y(\boldsymbol{q}^{\mathrm{FB}}(\gamma+\Delta\gamma))r_{ij}^x(\boldsymbol{q}^{\mathrm{FB}}(\gamma+\Delta\gamma))\right.$$
$$\left. - \left\{f_{ij}^x(\boldsymbol{q}^{\mathrm{FB}}(\gamma))r_{ij}^y(\boldsymbol{q}^{\mathrm{FB}}(\gamma)) + f_{ij}^y(\boldsymbol{q}^{\mathrm{FB}}(\gamma))r_{ij}^x(\boldsymbol{q}^{\mathrm{FB}}(\gamma))\right\}\right]. \tag{J.4}$$

By expanding $r_{ij}^\alpha(\boldsymbol{q}^{\mathrm{FB}}(\gamma+\Delta\gamma))$ in Eq. (J.4) by $\Delta\gamma$ from the finite strain γ, we obtain

$$\begin{aligned} r_{ij}^\alpha(\boldsymbol{q}^{\mathrm{FB}}(\gamma+\Delta\gamma)) &= r_i^\alpha(\boldsymbol{q}^{\mathrm{FB}}(\gamma+\Delta\gamma)) - r_j^\alpha(\boldsymbol{q}^{\mathrm{FB}}(\gamma+\Delta\gamma)) \\ &\simeq r_{ij}^\alpha(\boldsymbol{q}^{\mathrm{FB}}(\gamma)) + \Delta\gamma\left\{\delta_{\alpha x}\left(y_i(\boldsymbol{q}^{\mathrm{FB}}(\gamma)) - y_j(\boldsymbol{q}^{\mathrm{FB}}(\gamma))\right) + \frac{d\mathring{r}_i^\alpha(\boldsymbol{q}^{\mathrm{FB}}(\gamma))}{d\gamma} - \frac{d\mathring{r}_j^\alpha(\boldsymbol{q}^{\mathrm{FB}}(\gamma))}{d\gamma}\right\} \\ &= r_{ij}^\alpha(\boldsymbol{q}^{\mathrm{FB}}(\gamma)) + \Delta\gamma\left\{\delta_{\alpha x}y_{ij}(\boldsymbol{q}^{\mathrm{FB}}(\gamma)) + \frac{d\mathring{r}_{ij}^\alpha(\boldsymbol{q}^{\mathrm{FB}}(\gamma))}{d\gamma}\right\}. \end{aligned} \tag{J.5}$$

Similarly, by expanding $f_{ij}^\alpha(\gamma+\Delta\gamma)$ in Eq. (J.4) from the zero strain state, we obtain

$$\begin{aligned} f_{ij}^\alpha(\boldsymbol{q}^{\mathrm{FB}}(\gamma+\Delta\gamma)) &\simeq f_{ij}^\alpha(\boldsymbol{q}^{\mathrm{FB}}(\gamma)) + \sum_{k=1}^N\sum_{\zeta=x,y}\Delta\gamma\frac{\partial f_{ij}^\alpha}{\partial r_k^\zeta}\frac{dr_k^\zeta}{d\gamma} + \sum_{k=1}^N\Delta\gamma\frac{\partial f_{ij}^\alpha}{\partial \ell_k}\frac{d\ell_k}{d\gamma} \\ &= f_{ij}^\alpha(\boldsymbol{q}^{\mathrm{FB}}(\gamma)) \\ &\quad + \sum_{\zeta=x,y}\Delta\gamma\left[\frac{\partial f_{ij}^\alpha}{\partial r_i^\zeta}\left(\delta_{\zeta x}y_i(\boldsymbol{q}^{\mathrm{FB}}(\gamma)) + \frac{d\mathring{r}_i^\zeta(\boldsymbol{q}^{\mathrm{FB}}(\gamma))}{d\gamma}\right)\right. \\ &\quad \left. + \frac{\partial f_{ij}^\alpha}{\partial r_j^\zeta}\left(\delta_{\zeta x}y_j(\boldsymbol{q}^{\mathrm{FB}}(\gamma)) + \frac{d\mathring{r}_j^\zeta(\boldsymbol{q}^{\mathrm{FB}}(\gamma))}{d\gamma}\right)\right] \\ &\quad + \Delta\gamma\left[\frac{\partial f_{ij}^\alpha}{\partial \ell_i}\left(\delta_{\ell x}y_i(\boldsymbol{q}^{\mathrm{FB}}(\gamma)) + \frac{d\mathring{\ell}_i(\boldsymbol{q}^{\mathrm{FB}}(\gamma))}{d\gamma}\right)\right. \\ &\quad \left. + \frac{\partial f_{ij}^\alpha}{\partial \ell_j}\left(\delta_{\ell x}y_j(\boldsymbol{q}^{\mathrm{FB}}(\gamma)) + \frac{d\mathring{\ell}_j(\boldsymbol{q}^{\mathrm{FB}}(\gamma))}{d\gamma}\right)\right]. \end{aligned} \tag{J.6}$$

Moreover, using $\partial f_{ij}^\alpha/\partial r_j^\zeta = -\partial f_{ij}^\alpha/\partial r_i^\zeta$ and $\partial f_{ij}^\alpha/\partial \ell_j = \partial f_{ij}^\alpha/\partial \ell_i$, and f_{ij}^α can be written as

$$\begin{aligned} f_{ij}^\alpha(\boldsymbol{q}^{\mathrm{FB}}(\gamma+\Delta\gamma)) &= f_{ij}^\alpha(\boldsymbol{q}^{\mathrm{FB}}(\gamma)) + \sum_{\zeta=x,y}\Delta\gamma\frac{\partial f_{ij}^\alpha}{\partial r_i^\zeta}\left(\delta_{\zeta x}y_{ij}(\boldsymbol{q}^{\mathrm{FB}}(\gamma)) + \frac{d\mathring{r}_{ij}^\zeta(\boldsymbol{q}^{\mathrm{FB}}(\gamma))}{d\gamma}\right) \\ &\quad + \Delta\gamma\frac{\partial f_{ij}^\alpha}{\partial \ell_i}\left(\frac{d\mathring{\ell}_i(\boldsymbol{q}^{\mathrm{FB}}(\gamma))}{d\gamma} + \frac{d\mathring{\ell}_j(\boldsymbol{q}^{\mathrm{FB}}(\gamma))}{d\gamma}\right). \end{aligned} \tag{J.7}$$

Substituting Eqs. (J.5) and (J.7) into Eq. (J.4), we obtain

$$
\begin{aligned}
g(\gamma) = -\frac{1}{4L^2}\sum_{i,j(i\neq j)}\Bigg[& f_{ij}^{x}(\boldsymbol{q}^{\mathrm{FB}}(\gamma))\frac{d\mathring{r}_{ij}^{y}(\boldsymbol{q}^{\mathrm{FB}}(\gamma))}{d\gamma} + f_{ij}^{y}(\boldsymbol{q}^{\mathrm{FB}}(\gamma))\frac{d\mathring{r}_{ij}^{x}(\boldsymbol{q}^{\mathrm{FB}}(\gamma))}{d\gamma} \\
& + \sum_{\zeta=x,y}\left(\frac{\partial f_{ij}^{x}(\boldsymbol{q}^{\mathrm{FB}}(\gamma))}{\partial r_i^{\zeta}} r_{ij}^{y}(\boldsymbol{q}^{\mathrm{FB}}(\gamma)) + \frac{\partial f_{ij}^{y}(\boldsymbol{q}^{\mathrm{FB}}(\gamma))}{\partial r_i^{\zeta}} r_{ij}^{x}(\boldsymbol{q}^{\mathrm{FB}}(\gamma))\right) \\
& \quad \times \left(\delta_{\zeta x} y_{ij}(\boldsymbol{q}^{\mathrm{FB}}(\gamma)) + \frac{d\mathring{r}_{ij}^{\zeta}(\boldsymbol{q}^{\mathrm{FB}}(\gamma))}{d\gamma}\right) \\
& + \left(\frac{\partial f_{ij}^{x}(\boldsymbol{q}^{\mathrm{FB}}(\gamma))}{\partial \ell_i} r_{ij}^{y}(\boldsymbol{q}^{\mathrm{FB}}(\gamma)) + \frac{\partial f_{ij}^{y}(\boldsymbol{q}^{\mathrm{FB}}(\gamma))}{\partial \ell_i} r_{ij}^{xx}(\boldsymbol{q}^{\mathrm{FB}}(\gamma))\right) \\
& \quad \times \left(\frac{d\mathring{\ell}_i(\boldsymbol{q}^{\mathrm{FB}}(\gamma))}{d\gamma} + \frac{d\mathring{\ell}_j(\boldsymbol{q}^{\mathrm{FB}}(\gamma))}{d\gamma}\right)\Bigg]. \qquad \text{(J.8)}
\end{aligned}
$$

Because $\sum_{i(i\neq j)} f_{ij}^{\alpha}(\boldsymbol{q}^{\mathrm{FB}}(\gamma)) = 0$ in the FB state, the first and second terms on the RHS of Eq. (J.8) can be written as

$$
\begin{aligned}
\sum_{i,j(i\neq j)} f_{ij}^{\alpha}(\boldsymbol{q}^{\mathrm{FB}}(\gamma))\frac{d\mathring{r}_{ij}^{\kappa}(\boldsymbol{q}^{\mathrm{FB}}(\gamma))}{d\gamma} &= \sum_{i,j(i\neq j)} f_{ij}^{\alpha}(\boldsymbol{q}^{\mathrm{FB}}(\gamma))\left(\frac{d\mathring{r}_{i}^{\kappa}(\boldsymbol{q}^{\mathrm{FB}}(\gamma))}{d\gamma} - \frac{d\mathring{r}_{j}^{\kappa}(\boldsymbol{q}^{\mathrm{FB}}(\gamma))}{d\gamma}\right) \\
&= \sum_{j}\left(\sum_{j(j\neq i)} f_{ij}^{\alpha}(\boldsymbol{q}^{\mathrm{FB}}(\gamma))\right)\frac{d\mathring{r}_{i}^{\kappa}(\boldsymbol{q}^{\mathrm{FB}}(\gamma))}{d\gamma} \\
&\quad - \sum_{i}\left(\sum_{i(i\neq j)} f_{ij}^{\alpha}(\boldsymbol{q}^{\mathrm{FB}}(\gamma))\right)\frac{d\mathring{r}_{j}^{\kappa}(\boldsymbol{q}^{\mathrm{FB}}(\gamma))}{d\gamma} \\
&= 0. \qquad \text{(J.9)}
\end{aligned}
$$

Thus, g is expressed as

$$
\begin{aligned}
g(\gamma) = -\frac{1}{4L^2}\sum_{i,j(i\neq j)}\Bigg[& \sum_{\zeta=x,y}\left(\frac{\partial f_{ij}^{x}(\boldsymbol{q}^{\mathrm{FB}}(\gamma))}{\partial r_i^{\zeta}} r_{ij}^{y}(\boldsymbol{q}^{\mathrm{FB}}(\gamma)) + \frac{\partial f_{ij}^{y}(\boldsymbol{q}^{\mathrm{FB}}(\gamma))}{\partial r_i^{\zeta}} r_{ij}^{x}(\boldsymbol{q}^{\mathrm{FB}}(\gamma))\right) \\
& \quad \times \left(\delta_{\zeta x} y_{ij}(\boldsymbol{q}^{\mathrm{FB}}(\gamma)) + \frac{d\mathring{r}_{ij}^{\zeta}(\boldsymbol{q}^{\mathrm{FB}}(\gamma))}{d\gamma}\right) \\
& + \left(\frac{\partial f_{ij}^{x}(\boldsymbol{q}^{\mathrm{FB}}(\gamma))}{\partial \ell_i} r_{ij}^{y}(\boldsymbol{q}^{\mathrm{FB}}(\gamma)) + \frac{\partial f_{ij}^{y}(\boldsymbol{q}^{\mathrm{FB}}(\gamma))}{\partial \ell_i} r_{ij}^{xx}(\boldsymbol{q}^{\mathrm{FB}}(\gamma))\right) \\
& \quad \times \left(\frac{d\mathring{\ell}_i(\boldsymbol{q}^{\mathrm{FB}}(\gamma))}{d\gamma} + \frac{d\mathring{\ell}_j(\boldsymbol{q}^{\mathrm{FB}}(\gamma))}{d\gamma}\right)\Bigg]. \qquad \text{(J.10)}
\end{aligned}
$$

Using $\mathcal{H}_{ij}^{\alpha\beta} = \mathcal{J}_{ij}^{\alpha\beta} := -\partial_{q_j^{\beta}} f_{ij}^{\alpha}$ for $i \neq j$ in the case of the harmonic potential,

we can express g as

$$
\begin{aligned}
g(\gamma) = \frac{1}{4L^2} \sum_{i,j(i\neq j)} \Bigg[& \sum_{\zeta=x,y} \Big(y_{ij}(\boldsymbol{q}^{\mathrm{FB}}(\gamma)) \mathcal{H}^{x\zeta}_{ji}(\boldsymbol{q}^{\mathrm{FB}}(\gamma)) + x_{ij}(\boldsymbol{q}^{\mathrm{FB}}(\gamma)) \mathcal{H}^{y\zeta}_{ji}(\boldsymbol{q}^{\mathrm{FB}}(\gamma)) \Big) \\
& \times \left(\delta_{\zeta x} y_{ij}(\boldsymbol{q}^{\mathrm{FB}}(\gamma)) + \frac{d\mathring{r}^{\zeta}_{ij}(\boldsymbol{q}^{\mathrm{FB}}(\gamma))}{d\gamma} \right) \\
& + \Big(y_{ij}(\boldsymbol{q}^{\mathrm{FB}}(\gamma)) \mathcal{H}^{x\ell}_{ji}(\boldsymbol{q}^{\mathrm{FB}}(\gamma)) + x_{ij}(\boldsymbol{q}^{\mathrm{FB}}(\gamma)) \mathcal{H}^{y\ell}_{ji}(\boldsymbol{q}^{\mathrm{FB}}(\gamma)) \Big) \\
& \times \left(\frac{d\mathring{\ell}_i(\boldsymbol{q}^{\mathrm{FB}}(\gamma))}{d\gamma} + \frac{d\mathring{\ell}_j(\boldsymbol{q}^{\mathrm{FB}}(\gamma))}{d\gamma} \right) \Bigg] \\
= \frac{1}{4L^2} \sum_{i,j(i\neq j)} \Bigg[& y_{ij} \left(y_{ij}(\boldsymbol{q}^{\mathrm{FB}}(\gamma)) \mathcal{H}^{xx}_{ji}(\boldsymbol{q}^{\mathrm{FB}}(\gamma)) + x_{ij}(\boldsymbol{q}^{\mathrm{FB}}(\gamma)) \mathcal{H}^{yx}_{ji}(\boldsymbol{q}^{\mathrm{FB}}(\gamma)) \right) \\
& + \sum_{\zeta=x,y} \Big(y_{ij}(\boldsymbol{q}^{\mathrm{FB}}(\gamma)) \mathcal{H}^{x\zeta}_{ji}(\boldsymbol{q}^{\mathrm{FB}}(\gamma)) + x_{ij}(\boldsymbol{q}^{\mathrm{FB}}(\gamma)) \mathcal{H}^{y\zeta}_{ji}(\boldsymbol{q}^{\mathrm{FB}}(\gamma)) \Big) \frac{d\mathring{r}^{\zeta}_{ij}(\boldsymbol{q}^{\mathrm{FB}}(\gamma))}{d\gamma} \\
& + \Big(y_{ij}(\boldsymbol{q}^{\mathrm{FB}}(\gamma)) \mathcal{H}^{x\ell}_{ji}(\boldsymbol{q}^{\mathrm{FB}}(\gamma)) + x_{ij}(\boldsymbol{q}^{\mathrm{FB}}(\gamma)) \mathcal{H}^{y\ell}_{ji}(\boldsymbol{q}^{\mathrm{FB}}(\gamma)) \Big) \\
& \times \left(\frac{d\mathring{\ell}_i(\boldsymbol{q}^{\mathrm{FB}}(\gamma))}{d\gamma} + \frac{d\mathring{\ell}_j(\boldsymbol{q}^{\mathrm{FB}}(\gamma))}{d\gamma} \right) \Bigg]. \qquad \text{(J.11)}
\end{aligned}
$$

Thus, using Eqs (4.39) and (4.40), we obtain Eqs. (4.42)–(4.44).

J.2 The rigidity of the harmonic potential in the linear response regime

In this appendix, we verify the validity of our method to evaluate the rigidity G_0 for frictional harmonic potential in the linear response regime for various k_T/k_N and ϕ as in Ref. [119]. Figure J.1 presents the results of the rigidity, in which G_0 obtained by the eigenvalue analysis (filled symbols) is in perfect agreement with that obtained by the simulation (open symbols). Here we take the average over 5 ensembles for each ϕ and k_T. This figure confirms the validity of the theoretical method in the linear response regime.

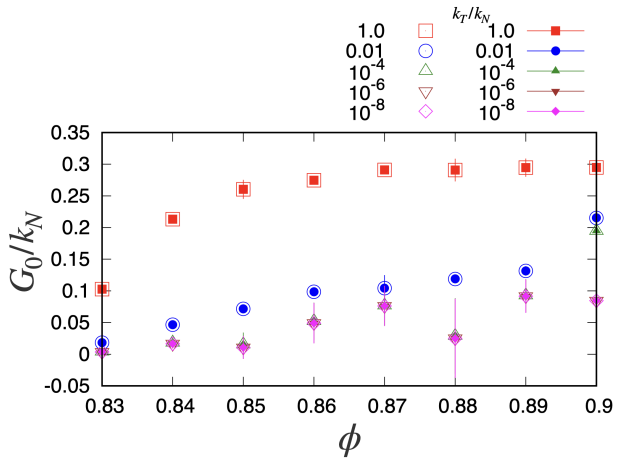

Figure J.1: The plot of the rigidity G_0 in the linear response regime for various k_T/k_N and ϕ, where open symbols and filled symbols are results of the theory and simulation, respectively.

Bibliography

[1] R. Zallen, The physics of amorphous solids (Wiley, 1983).

[2] H. M. Jaeger, S. R. Nagel, and R. P. Behringer, Granular solids, liquids, and gases, Rev. Mod. Phys. **68**, 1259 (1996).

[3] S. Alexander, Amorphous solids: their structure, lattice dynamics, and elasticity, Phys. Rep. **296**, 65, (1998).

[4] P. Richard, M. Nicodemi, R. Delannay, P. Ribiére, and D. Bideau, Slow relaxation and compaction of granular systems, Nature Materials **4**, 121 (2005).

[5] M. Wyart, On the rigidity of amorphous solids, Ann. Phys. Fr. **30**, 1 (2005).

[6] M. van Hecke, Jamming of soft particles: geometry, mechanics, scaling and isostaticity, J. Phys.: Cond. Matt. **22**, 033101 (2010).

[7] L. Berthier and G. Biroli, Theoretical perspective on the glass transition and amorphous materials, Rev. Mod. Phys., **83**, 587 (2011).

[8] A. Baule, F. Morone, H. J. Herrmann, and H. A. Makse, Edwards statistical mechanics for jammed granular matter, Rev. Mod. Phys. **90**, 015006 (2018).

[9] D. J. Durian, Foam Mechanics at the Bubble Scale, Phys. Rev. Lett. **75**, 4780 (1995).

[10] A. Liu and S. Nagel, Jamming is not just cool any more, Nature (London) **396**, 21 (1998).

[11] V. Trappe, V. Prasad, L. Cipelletti, P. N. Segre, and D. A. Weitz, Jamming phase diagram for attractive particles, Nature (London) **411**, 772 (2001).

[12] C. S. O'Hern, L. E. Silbert, A. J. Liu, and S. R. Nagel, Jamming at zero temperature and zero applied stress: The epitome of disorder, Phys. Rev. E **68**, 011306 (2003).

[13] N. Brilliantov, T. Pöschel, Kinetic Theory of Granular Gases, (Oxford, 2004).

[14] P. Jop, Y. Forterre, and O. Pouliquen, A constitutive law for dense granular flows Nature **441**, 727 (2006).

[15] K. Saitoh and H. Hayakawa, Rheology of a granular gas under a plane shear, Phys. Rev. E **75**, 021302 (2007).

[16] H. P. Zhang and H. A. Makse, Jamming transition in emulsions and granular materials, Phys. Rev. E **72**, 011301 (2005).

[17] W. G. Ellenbroek, E. Somfai, M. van Hecke, and W. van Saarloos, Critical Scaling in Linear Response of Frictionless Granular Packings near Jamming, Phys. Rev. Lett. **97**, 258001 (2006).

[18] T. S. Majmudar, M. Sperl, S. Luding, and R. P. Behringer, Jamming Transition in Granular Systems, Phys. Rev. Lett. **98**, 058001 (2007).

[19] M. Otsuki, H. Hayakawa, Critical behaviors of sheared frictionless granular materials near the jamming transition, Phys. Rev. E **80**, 011308 (2009).

[20] M. P. Ciamarra, R. Pastore, M. Nicodemi, and A. Coniglio, Jamming phase diagram for frictional particles, Phys. Rev. E **84**, 041308 (2011).

[21] M. Otsuki and H. Hayakawa, Critical scaling near jamming transition for frictional granular particles, Phys. Rev. E **83**, 051301 (2011).

[22] P. Chaudhuri, L. Berthier, and S. Sastry, Jamming Transitions in Amorphous Packings of Frictionless Spheres Occur over a Continuous Range of Volume Fractions, Phys. Rev. Lett. **104**, 165701 (2010).

[23] M. Ozawa, T. Kuroiwa, A. Ikeda, and K. Miyazaki, Jamming Transition and Inherent Structures of Hard Spheres and Disks, Phys. Rev. Lett. **109**, 205701 (2012).

[24] N. Kumar and S. Luding, Memory of jamming-multiscale models for soft and granular matter, Granular Matter **18**, 58 (2016).

[25] N. D. Ashcroft and N. W. Mermin, Solid State Physics (Harcourt, 1976).

[26] A. Virtanen, J. Joutsensaari, T. Koop, J. Kannosto, P. Yli-Pirilä, J. Leskinen, J. M. Mäkelä, J. K. Holopainen, U. Pöschl, M. Kulmala, D. R. Worsnop, and A. Laaksonen, An amorphous solid state of biogenic secondary organic aerosol particles, Nature Lett. **467**, 824 (2010).

[27] S. F. Edwards and D. R. Wilkinson, The surface statistics of a granular aggregate, Proc. Roy. Soc. London, Ser. A **381**, 17 (1982).

[28] S. F. Edwards and R. B. S. Oakeshott, Theory of powders, Physica A **157**, 1080 (1989).

[29] C. C. Mounfield and S. F. Edwards, The statistical mechanics of granular systems composed of elongated grains, Physica A **210**, 279 (1994).

[30] H. M. Jaeger and S. R. Nagel, Physics of the Granular State, Science **255**, 1523 (1992).

[31] E. Clément, J. Duran, and J. Rajchenbach, Experimental Study of Heaping in a Two-Dimensional "Sandpile", Phys. Rev. Lett. **69** 8 (1992).

[32] P. Evesque, D. Fargeix, P. Habib, M. P. Luong, and P. Porion, Pile density is a control parameter of sand avalanches, Phys. Rev. E **47**, 2326 (1993).

[33] C. S. O'Hern, S. A. Langer, A. J. Liu, and S. R. Nagel, Force Distributions near Jamming and Glass Transitions, Phys. Rev. Lett. **86**, 111 (2001).

[34] W. G. Ellenbroek, Z. Zeravcic, W. van Saarloos, and M. van Hecke, Non-affine response: Jammed packings vs. spring networks, Eur. Phys. Lett., **87**, 34004 (2009).

[35] O. Reynolds, On the dilatancy of media composed of rigid particles in contact. With experimental illustrations, Philos. Mag. Ser. **20**, 469 (1885).

[36] R. A. Bagnold, The shearing and dilatation of dry sand and the 'singing' mechanism, Proc. R. Soc. London A **295**, 219 (1966).

[37] P. A. Thompson and G. S. Grest, Granular flow: Friction and the dilatancy transition, Phys. Rev. Lett. **67**, 1751 (1991).

[38] GDR MiDi , On dense granular flows, Eur. Phys. J. E **14**, 341 (2004).

[39] F. da Cruz, S. Emam, M. Prochnow, J. N. Roux, and F. Chevoir, Rheophysics of dense granular materials: Discrete simulation of plane shear flows, Phys. Rev. E. **72**, 021309 (2005).

[40] Y. Forterre and O. Pouliquen, Flows of Dense Granular Media, Annu. Rev. Fluid Mech. **40**, 1 (2008).

[41] F. Boyer, É. Guazzelli, and O. Pouliquen, Unifying Suspension and Granular Rheology, Phys. Rev. Lett. **107**, 188301 (2011).

[42] J. B. Knight, C.G. Fandrich, C.N. Lau, H.M. Jaeger, and S. R. Nagel, Density relaxation in a vibrated granular material, Phys. Rev. E **51**, 3957 (1995).

[43] E. R. Nowak, J.B. Knight, E. Ben-Naim, H. M. Jaeger, and S.R. Nagel, Density fluctuations in vibrated granular materials, Phys. Rev E **57**, 1971 (1998).

[44] M. D. Haw, W. C. K. Poon, and P. N. Pusey, Direct observation of oscillatory-shear-induced order in colloidal suspensions, Phys. Rev. E **57**, 6859 (1998).

[45] M. D. Haw, W. C. K. Poon, P. N. Pusey, P. Hebraud, and F. Lequeux, Colloidal glasses under shear strain, Phys. Rev. E **58**, 4673 (1998).

[46] M. Nicolas, P. Duru, and O. Pouliquen, Compaction of a granular material under cyclic shear, Eur. Phys. J. E **3**, 309 (2000).

[47] O. Pouliquen, M. Belzons, and M. Nicolas, Fluctuating Particle Motion during Shear Induced Granular Compaction, Phys. Rev. Lett. **91**, 014301 (2003).

[48] D. Ishima and H. Hayakawa, Dilatancy of frictional granular materials under oscillatory shear with constant pressure, EPJ Web of Conf. **249**, 02011 (2021).

[49] F. P. Bowden and D. Tabor, The Friction and Lubrication of Solids (Clarendon Press, Oxford, 1954).

[50] J. Gao, W. D. Luedtke, D. Gourdon, M. Ruths, J. N. Israelchvili, and U. Landman, Frictional Forces and Amontons' Law: From the Molecular to the Macroscopic Scale, J. Phys. Chem. B **108**, 3410 (2004).

[51] H. Yoshizawa, Y. L. Chen, and J. Israelachvili, Fundamental mechanisms of interfacial friction. 1. Relation between adhesion and friction, J. Phys. Chem. **97**, 4128 (1993).

[52] F. Heslot, T. Baumberger, B. Perrin, B. Caroli, and C. Caroli, Creep, stick-slip, and dry-friction dynamics: Experiments and a heuristic model, Phys. Rev. E **49**, 4973 (1994).

[53] H. Matsukawa and F. Fukuyama, Theoretical study of friction: One-dimensional clean surfaces, Phys. Rev. B **49**, 17286 (1994).

[54] B. N. J. Persson, Sliding Friction: Physical Principles and Applications, (Springer, 2000).

[55] J. H. Dieterich, Time-Dependent Friction in Rocks, J. Geophys. Res. **77**, 3690 (1972).

[56] E. Brown and H. M. Jaeger, Dynamic Jamming Point for Shear Thickening Suspensions, Phys. Rev. Lett. **103**, 086001 (2009).

[57] R. Seto, R. Mari, J. F. Morris, and M. M. Denn, Discontinuous Shear Thickening of Frictional Hard-Sphere Suspensions Phys. Rev. Lett. **111**, 218301 (2013).

[58] M. Wyart and M. E. Cates, Discontinuous Shear Thickening without Inertia in Dense Non-Brownian Suspensions Phys. Rev. Lett., **112**, 098302 (2014).

[59] T. Kawasaki and L. Berthier, Discontinuous shear thickening in Brownian suspensions, Phys. Rev. E **98**, 012609 (2018).

[60] M. Otsuki, H. Hayakawa, Shear jamming, discontinuous shear thickening, and fragile states in dry granular materials under oscillatory shear Phys. Rev. E **101**, 032905 (2020).

[61] Pradipto and Hisao Hayakawa, Simulation of dense non-Brownian suspensions with the lattice Boltzmann method: shear jammed and fragile states, Soft Matter **16**, 945 (2020).

[62] D. Bi, J. Zhang, B. Chakraborty, and R. P. Behringer, Jamming by shear, Nature (London) **480**, 355 (2011).

[63] A. Fall, F. Bertrand, D. Hautemayou, C. Meziére, P, Moucheront, A. Lemaître, and G. Ovarlez, Macroscopic Discontinuous Shear Thickening versus Local Shear Jamming in Cornstarch, Phys, Rev. Lett. **114**, 098301 (2015).

[64] S. Sarkar, D. Bi, J. Zhang, J. Ren, R. P. Behringer, and B. Chakraborty, Shear-induced rigidity of frictional particles: Analysis of emergent order in stress space, Phys. Rev. E **93**, 042901 (2016.

[65] I. R. Peters, S. Majumdar, and H. M. Jaeger, Direct observation of dynamic shear jamming in dense suspensions, Nature (London) **532**, 214 (2016).

[66] D. Wang, J. Ren, J. A. Dijksman, H. Zheng, and R. P. Behringer, Microscopic Origins of Shear Jamming for 2D Frictional Grains, Phys. Rev. Lett. **120**, 208004 (2018).

[67] E. D. Knowlton, D. J. Pine, and L. Cipelletti, A microscopic view of the yielding transition in concentrated emulsions, Soft Matter **10**, 6931 (2014).

[68] T. Kawasaki and L. Berthier, Macroscopic yielding in jammed solids is accompanied by a nonequilibrium first-order transition in particle trajectories, Phys. Rev. E **94**, 022615 (2016).

[69] S. Dagois-Bohy, E. Somfai, B. P. Tighe, and M. van Hecke, Softening and yielding of soft glassy materials, Soft Matter **13**, 9036 (2017).

[70] M. Otsuki and H. Hayakawa, Softening and residual loss modulus of jammed grains under oscillatory shear in absorbing state, Phys. Rev. Lett. **128**, 208002 (2022).

[71] D. Ishima and H. Hayakawa, Scaling laws for frictional granular materials confined by constant pressure under oscillatory shear, Phys. Rev. E **101**, 042902 (2020).

[72] M. Otsuki and H. Hayakawa, Discontinuous change of shear modulus for frictional jammed granular materials, Phys. Rev. E **95**, 062902 (2017).

[73] M. Doi and F. Edwards, The Theory of Polymer Dynamics (Oxford Univ. Press, 1986).

[74] R. H. Ewoldt, A. E. Hosoi, and G. H. McKinley, New measures for characterizing nonlinear viscoelasticity in large amplitude oscillatory shear, J. Rheol. **52**, 1427 (2008).

[75] K. Hyun, M. Wilhelm, C. O. Klein, K. S. Cho, J. G. Nam, K. H. Ahn, S. J. Lee, R. H. Ewoldt, and G. H. McKinley, A review of nonlinear oscillatory shear tests: Analysis and application of large amplitude oscillatory shear (LAOS), Prog. Polym. Sci. **36**, 1697 (2011).

[76] I. Argatov, A. Iantchenko, and V. Kochebitov, How to define the storage and loss moduli for a rheologically nonlinear material?, Cont. Mech. Thermodyn. **29**, 1375 (2017).

[77] N. Miatarai and F. Nori, Wet granular materials, Advances in Physics **55**, 1 (2007).

[78] S. Luding, Global equation of state of two-dimensional hard sphere systems, Phys. Rev. E **63**, 042201 (2001).

[79] L. Oddershede, P. Dimon, and J Bohr, Self-Organized Criticality in Fragmenting, Phys. Rev. Lett. **71**, 1 (1993).

[80] H. Katsuragi, D. Sugino, and H. Honjo, Crossover of weighted mean fragment mass scaling in two-dimensional brittle fragmentation, Phys. Rev. E. **70**, 065103(R) (2004).

[81] D. Shimamoto, and M. Yanagisawa, Common Packing Patterns for Jammed Particles of Different Power Size Distributions, arXiv: 2205.08111.

[82] M. Wyart, S. R. Nagel, and T. A. Witten, Geometric origin of excess low-frequency vibrational modes in weakly connected amorphous solids, Eur. Phys. Lett. **72**, 486 (2005).

[83] A. Zaccone and E. S.-Romano, Approximate analytical description of the nonaffine response of amorphous solids, Phys. Rev. B **83**, 184205 (2011).

[84] E. Lerner, G. Düring, and E. Bouchbinder, Statistics and Properties of Low-Frequency Vibrational Modes in Structural Glasses, Phys. Rev. Lett. **117**, 035501 (2016).

[85] M. Wyart, L. E. Silbert, S. R. Nagel, and T. A. Witten, Effects of compression on the vibrational modes of marginally jammed solids, Phys. Rev. E 72, 051306 (2005).

[86] H. Mizuno, K. Saitoh, and L. Silbert, Elastic moduli and vibrational modes in jammed particulate packings, Phys. Rev. E **93**, 062905 (2016).

[87] L. Gartner and E. Lerner, Nonlinear plastic modes in disordered solids, Phys. Rev. E **93**, 011001(R) (2016).

[88] S. Bonfanti, R. Guerra, C. Mondal, I. Procaccia, and S. Zapperi, Elementary plastic events in amorphous silica, Phys. Rev. E 100 060602(R) (2019).

[89] P. Morse, S. Wijtmans, M. van Deen, M. van Hecke, and M. L. Manning, Differences in plasticity between hard and soft spheres, Phys. Rev. Res. **2**, 023179 (2020).

[90] E. DeGiuli, E. Lerner, C. Brito, and M. Wyart, Force distribution affects vibrational properties in hard-sphere glasses, Proc. Natl. Acad. Sci. U.S.A. **111**, 17054 (2014).

[91] E. DeGiuli, A. Laversanne-Finot, G. Düring, E. Lerner, and M. Wyart, Effects of coordination and pressure on sound attenuation, boson peak and elasticity in amorphous solids, Soft Matter **10**, 5628 (2014).

[92] M. Baity-Jesi, V. Martín-Mayor, G. Parisi, and S. Perez-Gaviro, Soft Modes, Localization, and Two-Level Systems in Spin Glasses, Phys. Rev. Lett. **115**, 267205 (2015).

[93] Z. Zeravcic, N. Xu, A. J. Liu, S. R. Nagel, and W. van Saarloos, Excitations of ellipsoid packings near jamming, Eur. Phys. Lett. **87**, 26001 (2009).

[94] M. Mailman, C. F. Schreck, C. S. O'Hern, and B. Chakraborty, Jamming in Systems Composed of Frictionless Ellipse-Shaped Particles, Phys. Rev. Lett. **102**, 255501 (2009).

[95] C. F. Schreck, N. Xu, and C. S. O'Hern, A comparison of jamming behavior in systems composed of dimer- and ellipse-shaped particles, Soft Matter **6**, 2960 (2010).

[96] P. J. Yunker, K. Chen, Z. Zhang, W. G. Ellenbroek, A. J. Liu, and A. G. Yodh, Rotational and translational phonon modes in glasses composed of ellipsoidal particles, Phys. Rev. E **83**, 011403 (2011).

[97] C. F. Schreck, M. Mailman, B. Chakraborty, and C. S. O'Hern, Constraints and vibrations in static packings of ellipsoidal particles, Phys. Rev. E **85**, 061305 (2012).

[98] K. Shiraishi, H. Mizuno, and A. Ikeda, Vibrational properties of two-dimensional dimer packings near the jamming transition, Phys. Rev. E **100**, 012606 (2019).

[99] S. Papanikolaou, C. S. O'Hern, and M. D. Shattuck, Isostaticity at Frictional Jamming, Phys. Rev. Lett. **110**, 198002 (2013).

[100] C. Brito, H. Ikeda, P. Urbani, M. Wyart, and F. Zamponi, Universality of jamming of nonspherical particles, Proc. Natl. Acad. Sci. U.S.A. **115**, 11736 (2018).

[101] J. D. Treado, D. Wang, A. Boromand, M. P. Murrell, Mark D. Shattuck, and C. S. O'Hern, Bridging particle deformability and collective response in soft solids, Phys. Rev. Materials **5**, 055605 (2021).

[102] H. Ikeda, C. Brito, M. Wyart, and F. Zamponi, Jamming with Tunable Roughness, Phys. Rev. Lett. **124**, 208001 (2020).

[103] H. Ikeda, Testing mean-field theory for jamming of non-spherical particles: contact number, gap distribution, and vibrational density of states, Eur. Phys. E **44**, 120 (2021).

[104] E. Somfai, M. van Hecke, W. G. Ellenbroek, K. Shundyak, and W. van Saarloos, Critical and noncritical jamming of frictional grains, Phys. Rev. E **75**, 020301(R) (2007).

[105] S. Henkes, M. van Hecke, and W. van Saarloos, Critical jamming of frictional grains in the generalized isostaticity picture, Eur. Phys. Lett. **90**, 14003 (2010).

[106] K. Liu, J. E. Kollmer, K. E. Daniels, J. M. Schwarz, and S. Henkes, Spongelike Rigid Structures in Frictional Granular Packings, Phys. Rev. Lett. **126**, 088002 (2021).

[107] C. Maloney and A. Lemaître, Universal Breakdown of Elasticity at the Onset of Material Failure, Phys. Rev. Lett. **93**, 195501 (2004).

[108] C. Maloney and A. Lemaître, Amorphous systems in athermal, quasistatic shear, Phys. Rev. E **74**, 016118 (2006).

[109] A. Lemaître and C. Maloney, Sum Rules for the Quasi-Static and Visco-Elastic Response of Disordered Solids at Zero Temperature, J. Stat. Phys. **123**, 415 (2006).

[110] S. Karmakar, A. Lemaître, E. Lerner, and I. Procaccia, Predicting Plastic Flow Events in Athermal Shear-Strained Amorphous Solids, Phys. Rev. Lett. **104**, 215502 (2010).

[111] M. L. Manning and A. J. Liu, Vibrational Modes Identify Soft Spots in a Sheared Disordered Packing, Phys. Rev. Lett. **107**, 108302 (2011).

[112] R. Dasgupta, S. Karmakar, and I. Procaccia, Universality of the Plastic Instability in Strained Amorphous Solids, Phys. Rev. Lett. **108**, 075701 (2012).

[113] F. Ebrahem, F. Bamer, and B. Markert, Origin of reversible and irreversible atomic-scale rearrangements in a model two-dimensional network glass, Phys. Rev. E **102**, 033006 (2020).

[114] D. Richard, M. Ozawa, S. Patinet, E. Stanifer, B. Shang, S. A. Ridout, B. Xu, G. Zhang, P. K. Morse, J.-L. Barrat, L. Berthier, M. L. Falk, P. Guan, A. J. Liu, K. Martens, S. Sastry, D. Vandembroucq, E. Lerner, and M. L. Manning, Predicting plasticity in disordered solids from structural indicators, Phys. Rev. Materials **4**, 113609 (2020).

[115] J. Chattoraj, O. Gendelman, M. Pica Ciamarra, and I. Procaccia, Oscillatory Instabilities in Frictional Granular Matter, Phys. Rev. Lett. **123**, 098003 (2019).

[116] J. Chattoraj, O. Gendelman, M. P. Ciamarra, and I. Procaccia, Noise amplification in frictional systems: Oscillatory instabilities, Phys. Rev. E **100**, 042901 (2019).

[117] H. Charan, O. Gendelman, I. Procaccia, and Y. Sheffer, Giant amplification of small perturbations in frictional amorphous solids, Phys. Rev. E **101**, 062902 (2020).

[118] E. Bitzek, P. Koskinen, F. Gähler, M. Moseler, P. Gumbsch, Structural Relaxation Made Simple, Phys. Lev. Lett. **97**, 170201 (2006).

[119] D. Ishima, K. Saitoh, M. Otsuki, and H. Hayakawa, Theory of rigidity and density of states of two-dimensional amorphous solids of dispersed frictional grains in the linear response regime, arXiv:2207.06632.

[120] L. D. Landau, and E. M. Lifshitz, Fluid Mechanics, (Pergamon Press, 1987).

[121] J. F. Brady, and G. Bossis, Stokesian Dynamics, Annu. Rev. Fluid Mech. **20**, 111 (1988).

[122] R. C. Ball, and J. R. Melrose, A simulation technique for many spheres in quasi-static motion under frame-invariant pair drag and Brownian forces, Physica A **247** 444 (1997).

[123] P. A. Cundall, O. D. L. Strack, A discrete numerical model for granular assemblies, Géotechnique **29**, 47 (1979).

[124] S. Luding, Cohesive, frictional powders: contact models for tension, Granul. Matter **10**, 235 (2008).

[125] C. O'Sullivan, Particulate Discrete Element Modelling: A Geomechanics Perspective, CRC Press, (2011).

[126] K. L. Johnson, Contact Mechanics (Cambridge Univ. Press, 1985).

[127] L. D. Landau, and E. M. Lifshitz, Theory of Elasticity, (Pergamon Press, 1986).

[128] V. L. Popov, Contact Mechanics and Friction: Physical Principles and Applications (Springer-Verlag, 2010).

[129] G. Kuwabara and K. Kono, Restitution Coefficient in a Collision between Two Spheres, Jpn. J. Appl. Phys. **26**, 1230 (1987).

[130] N. V. Brilliantov, F. Spahn, J.-M. Hertzsch, and T. Pöschel, Model for collisions in granular gases, Phys. Rev. E **53**, 5382 (1996).

[131] W. A. M. Morgado and I. Oppenheim, Energy dissipation for quasielastic granular particle collisions, Phys. Rev. E **55**, 1940 (1997).

[132] K. Saitoh, R. Shrivastava, and S. Luding, Rotational sound in disordered granular materials, Phys. Rev. E **99**, 012906 (2019).

[133] W. C. Swope, H. C. Andersen, P. H. Berens, and K. R. Wilson, A computer simulation method for the calculation of equilibrium constants for the formation of physical clusters of molecules: Application to small water clusters, J. Chem. Phys. **76**, 637 (1982).

[134] K. Hima Nagamanasa, S. Gokhale, A. K. Sood, and R. Ganapathy, Experimental signatures of a nonequilibrium phase transition governing the yielding of a soft glass, Phys. Rev. E **89**, 062308 (2014).

[135] P. Leishangthem, A. D.S. Parmar, and S. Sastry, The yielding transition in amorphous solids under oscillatory shear deformation, Nat. Commun. **8**, 14653 (2017).

[136] M. Ozawa, L. Berthier, G. Birolib, A. Rosso, and G. Tarjus, Random critical point separates brittle and ductile yielding transitions in amorphous materials, Proc. Natl. Acad. Sci. U.S.A. **115**, 6656 (2018).

[137] A. H. Clark, J. D. Thompson, M. D. Shattuck, N. T. Ouellette, and C. S. O'Hern, Critical scaling near the yielding transition in granular media, Phys. Rev. E **97**, 062901 (2018).

[138] J. Boschan, S. Luding, and B. P. Tighe, Jamming and irreversibility, Granul. Matter **21**, 58 (2019).

[139] M. Singh, M. Ozawa, and L. Berthier, Brittle yielding of amorphous solids at finite shear rates, Phys. Rev. Materials **4**, 025603 (2020).

[140] A. Lees and S. Edwards, The computer study of transport processes under extreme conditions, J. Phys. C: Solid State Phys. **5**, 1921 (1972).

[141] D. J. Evans and G. P. Morriss, Statistical Mechanics of Nonequilibrium Liquids, 2nd ed. (Cambridge University Press, 2008).

[142] P. Olsson and S. Teitel, Critical scaling of shearing rheology at the jamming transition of soft-core frictionless disks, Phys. Rev. E 83, 030302(R) (2011).

[143] E. Lerner and I. Procassia, Locality and nonlocality in elastoplastic responses of amorphous solids, Phys. Rev. E **79**, 066109 (2009).

[144] S. Karmakar, E. Lerner, I. Procaccia, and J. Zylberg, Statistical physics of elastoplastic steady states in amorphous solids: Finite temperatures and strain rates, Phys. Rev. E **82**, 031301 (2010).